การสังเคราะห์ตัวเร่งปฏิกิริยาโลหะแทรนซิชันไทเทโนซิลิเกตสำหรับเบนซีนไฮดรอกซิเลชัน

นางสาวพรพิมล วงศ์สุวรรณ

วิทยานิพนธ์นี้เป็นส่วนหนึ่งของการศึกษาตามหลักสูตรปริญญาวิทยาศาสตรมหาบัณฑิต
สาขาวิชาปิโตรเคมีและวิทยาศาสตร์พอลิเมอร์
คณะวิทยาศาสตร์ จุฬาลงกรณ์มหาวิทยาลัย
ปีการศึกษา 2559

SYNTHESIS OF TRANSITION METAL-TITANOSILICATE CATALYSTS FOR BENZENE HYDROXYLATION

Miss Pornpimol Wongsuwan

A Thesis Submitted in Partial Fulfillment of the Requirements
for the Degree of Master of Science Program in Petrochemistry and Polymer Science
Faculty of Science
Chulalongkorn University
Academic Year 2016

Thesis Title	SYNTHESIS OF TRANSITION METAL-TITANOSILICATE CATALYSTS FOR BENZENE HYDROXYLATION
By	Miss Pornpimol Wongsuwan
Field of Study	Petrochemistry and Polymer Science
Thesis Advisor	Duangamol Tungasmita, Ph.D.

Accepted by the Faculty of Science, Chulalongkorn University in Partial Fulfillment of the Requirements for the Master's Degree

.....Dean of the Faculty of Science
(Associate Professor Polkit Sangvanich, Ph.D.)

THESIS COMMITTEE

.....Chairman
(Assistant Professor Warinthorn Chavasiri, Ph.D.)

.....Thesis Advisor
(Duangamol Tungasmita, Ph.D.)

.....Examiner
(Associate Professor Wimonrat Trakarnpruk, Ph.D.)

.....External Examiner
(Sanya Prangsri-aroon, Ph.D.)

พรพิมล วงศ์สุวรรณ : การสังเคราะห์ตัวเร่งปฏิกิริยาโลหะแทรนซิชันไทเทโนซิลิเกตสำหรับเบนซีนไฮดรอกซิเลชัน (SYNTHESIS OF TRANSITION METAL-TITANOSILICATE CATALYSTS FOR BENZENE HYDROXYLATION) อ.ที่ปรึกษาวิทยานิพนธ์หลัก: ดร. ดวงกมล ตุงคะสมิต, 180 หน้า.

สามารถสังเคราะห์ไทเทโนซิลิเกตที่มีรูพรุนขนาดเล็ก (ไทเทโนซิลิกาไลต์-1 และไทเทเนียม-เอ็มดับเบิลยูดับเบิลยู) และรูพรุนขนาดกลาง (ไทเทเนียมเอ็มซีเอ และไทเทเนียมเอสบีเอ-15) ที่มีโลหะแทรนซิชันได้สำเร็จโดยวิธีทางความร้อน และตามด้วยวิธีเคลือบฝัง โลหะแทรนซิชันในงานวิจัยนี้ได้แก่ ซีเรียม คอปเปอร์ เหล็ก และวาเนเดียม ผลิตภัณฑ์ที่สังเคราะห์ได้ทั้งหมดถูกตรวจสอบลักษณะทางกายภาพโดยใช้เทคนิคการเลี้ยวเบนของรังสีเอ็กซ์ การดูดซับแก๊สไนโตรเจน การดูดกลืนแสงยูวี กล้องจุลทรรศน์อิเล็กตรอนแบบส่องกราด กล้องจุลทรรศน์อิเล็กตรอนแบบส่องผ่าน และไอซีพี-เอ็มเอส ตัวเร่งปฏิกิริยาที่มีโลหะสองชนิดทุกตัวยังคงรักษาโครงสร้างของวัสดุต้นแบบไว้ได้หลังการดัดแปลง นอกจากนี้โลหะตัวที่สองได้กระจายอยู่บนพื้นผิวของตัวรองรับไทเทโนซิลิเกตซึ่งยืนยันโดยผลการทดสอบด้วยกล้องจุลทรรศน์อิเล็กตรอนแบบส่องผ่าน ตัวเร่งปฏิกิริยาที่เตรียมได้ถูกทดสอบความสามารถในการเร่งปฏิกิริยาในปฏิกิริยาเบนซีนไฮดรอกซิเลชันโดยมีไฮโดรเจนเปอร์ออกไซด์เป็นตัวออกซิไดซ์ ในบรรดาโลหะตัวที่สองชนิดต่างๆ วาเนเดียมมีความสามารถในการเร่งปฏิกิริยาได้ดีที่สุดในทุกตัวรองรับไทเทโนซิลิเกต การมีวาเนเดียมในตัวเร่งปฏิกิริยาจะเพิ่มประสิทธิภาพในการเร่งปฏิกิริยาออกซิเดชันเนื่องจากเป็นการเพิ่มตำแหน่งในการเกิดปฏิกิริยา ธรรมชาติและการกระจายตัวของวาเนเดียมรวมไปถึงโครงสร้างของตัวรองรับไทเทโนซิลิเกตมีผลอย่างมากต่อผลิตภัณฑ์ฟีนอลที่ได้ ที่ภาวะการทดลองที่ดีที่สุดของตัวเร่งปฏิกิริยาแต่ละตัว วาเนเดียมบนตัวรองรับไทเทเนียมเอ็มดับเบิลยูดับเบิลยูที่มีปริมาณวาเนเดียมร้อยละ 5 โดยน้ำหนักให้ประสิทธิภาพในการเร่งปฏิกิริยาสูงที่สุดโดยให้ผลิตภัณฑ์ฟีนอล 14.72% โครงสร้างของรูพรุนที่เป็นแบบสามมิติที่มีเอกลักษณ์เฉพาะตัวของไทเทเนียมเอ็มดับเบิลยูดับเบิลยูทำให้ความสามารถในการแพร่และการขนส่งสารตั้งต้นมีประสิทธิภาพสูงส่งผลให้มีประสิทธิภาพในการเร่งปฏิกิริยาสูงด้วย ภาวะการทดลองที่ดีที่สุดในปฏิริยาเบนซีนไฮดรอกซิเลชันอยู่ที่สัดส่วนโมลของเบนซีนต่อไฮโดรเจนเปอร์ออกไซด์ 1:3 ตัวเร่งปฏิกิริยาวาเนเดียมบนตัวรองรับไทเทเนียมเอ็มดับเบิลยูดับเบิลยูที่มีโลหะวาเนเดียมร้อยละ 5 โดยน้ำหนักปริมาณ 0.1 กรัม อะซิโตไนไตรล์ 5.66 กรัม ที่อุณหภูมิ 55 องศาเซลเซียส เป็นเวลา 3 ชั่วโมง

สาขาวิชา ปิโตรเคมีและวิทยาศาสตร์พอลิเมอร์ ลายมือชื่อนิสิต .....

ปีการศึกษา 2559 ลายมือชื่อ อ.ที่ปรึกษาหลัก .....

5572256023 : MAJOR PETROCHEMISTRY AND POLYMER SCIENCE
KEYWORDS: TITANOSILICATE/BIMETALLIC CATALYST/BENZENE HYDROXYLATION

PORNPIMOL WONGSUWAN: SYNTHESIS OF TRANSITION METAL-TITANOSILICATE CATALYSTS FOR BENZENE HYDROXYLATION. ADVISOR: DUANGAMOL TUNGASMITA, Ph.D., 180 pp.

The microporous (TS-1 and Ti-MWW) and mesoporous (Ti-MCA and Ti-SBA-15) titanosilicates with the transition metal were successfully synthesized by hydrothermal followed by impregnation method. The transition metals in this study were Ce, Cu, Fe, and V. All synthesized products were characterized the physical properties by using X-ray powder diffraction, N_2 adsorption-desorption, DR-UV spectrophotometry, scanning electron microscopy (SEM), transmission electron microscopy (TEM) and inductively coupled plasma mass spectrometry (ICP-MS). After the bimetallic catalysts modification, the porous materials still preserved structure of parent materials. Moreover, the second metal was dispersed on the surface of titanosilicate supporter which confirmed by TEM results. The catalytic activity of the prepared catalysts was evaluated in the benzene hydroxylation with hydrogen peroxide as the oxidizing agent. Among various kind of second metals, V presented the best catalytic activity in all titanosilicate supports. The presence of V in catalyst remarkably enhanced catalytic oxidation capacity because of the increase of active site. Nature and dispersion of vanadium species as well as structure of titanosilicate support had tremendous effect on the yield of phenol product. At the optimum reaction condition of each catalyst, vanadium supported on Ti-MWW with 5 wt.% V-content showed highest catalytic performance with 14.72% yield of phenol. The three-dimensional and unique pore system of Ti-MWW made the efficient diffusion and transport of reactants resulting in high catalytic performance. The optimum condition in benzene hydroxylation was carried at benzene: H_2O_2 mole ratio of 1:3, 0.1 g of 5 wt.% V/Ti-MWW, acetonitrile 5.66 g, 55°C for 3 h.

Field of Study:	Petrochemistry and Polymer Science	Student's Signature	.....
		Advisor's Signature	.....
Academic Year:	2016		

ACKNOWLEDGEMENTS

The accomplishment of this thesis can be attributed to the extensive support and assistance from Dr. Duangamol Tungasmita, my thesis advisor. I would like to sincere gratitude to her for valuable advice and guidance in this research as well as extraordinary experiences throughout the work.

I would like to gratitude to Asistant Professor Dr. Warinthorn Chavasiri as the chairman, Associate Professor Dr. Wimonrat Trakarnpruk and Dr. Sanya Prangsri-aroon who have been members of thesis committee, for all of their kindness and useful advice in this research.

I would like to gratefully thank IRPC Public Company Limited for supporting the finance and all suggestions. Moreover, I would like to thank Department of Chemistry and Program of Petrochemistry and Polymer Science, Faculty of Science, Chulalongkorn University for the valuable knowledge and experience.

Many thanks go in particular to the members of Materials Chemistry and Catalysis Research Unit for their help and encouragement throughout the course of my research and study. Finally, I greatly thank to my family and all of my friends for their help and encouragement during my graduate study.

CONTENTS

Page

Page

Page

Page

Page

Page

Page

Page

LIST OF TABLES

Table **Page**

LIST OF FIGURES

Figure **Page**

LIST OF SCHEMES

Scheme **Page**

LIST OF ABBREVIATION

Å	Angstrom
BET	Brunauer-Emmett-Teller
^{o}C	Degree Celsius
GC	Gas chromatography
g	Gram (s)
h	Hour
µm	Micrometer (s)
mg	Milligram (s)
ml	Milliliter (s)
min	Minute (s)
M	Molarity
N	Normality
nm	Nanometer (s)
SEM	Scanning electron microscopy
TEM	Transmission electron microscopy
XRD	X-ray diffraction
wt.%	Percentage by weight

CHAPTER I

INTRODUCTION

1.1 Background

Phenol is one of the most important organic chemical which is used as an intermediate in industrial chemicals manufacture. Figure 1.1 shows global phenol consumption in 2015[1]. The largest use of phenol (49%) is in the production of bisphenol A that is primarily used to produce polycarbonates and epoxy resins. The second largest use of phenol with 30% of total phenol consumption is in phenolic resins manufacture. These resins are used mainly in the construction industry. Moreover, phenol is used as a precursor in the manufacture of alkylphenols, caprolactam, adipic acid and others. Therefore, the global phenol market is mainly driven by demand of the major derivatives namely bisphenol A and phenolic resins.

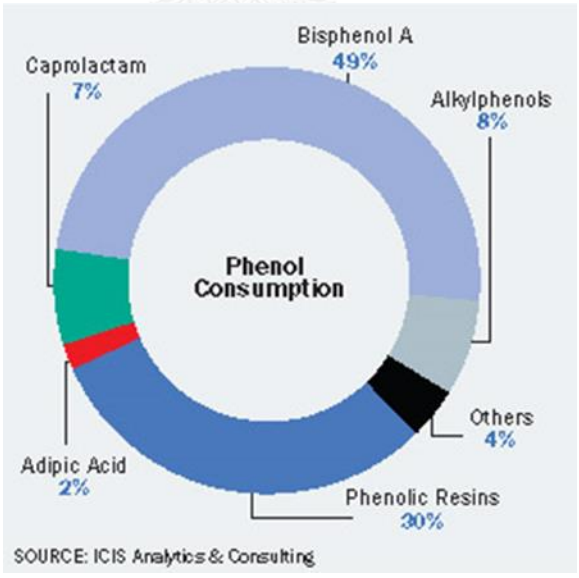

Figure 1.1 Global phenol consumption in 2015

The global demand for bisphenol A and phenolic resins have been continuously increasing due to high demand of its end-use segment. As can be seen in Figure 1.2 [2, 3], the global market of bisphenol A and phenolic resins has grown and is expected to continue to increase in the coming years. The growing demand for bisphenol A and phenolic resins will result in strong demand for phenol. Thus, In order to support the demand in the future, the efficient production of phenol is necessary.

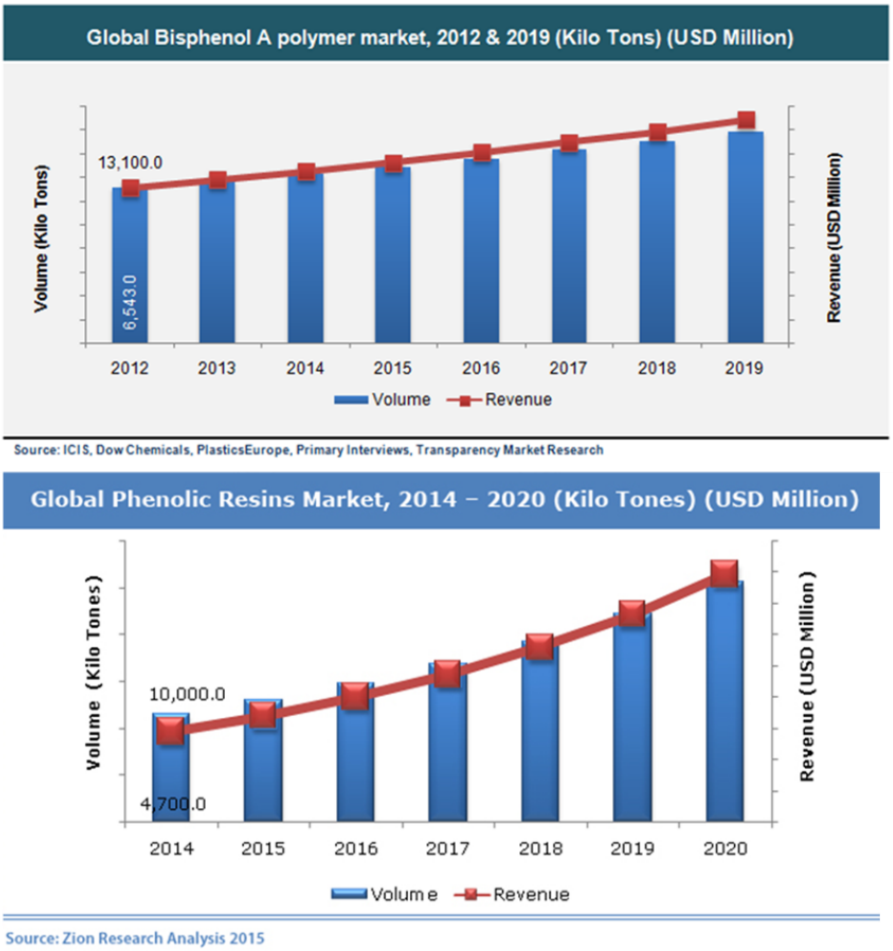

Figure 1.2 Global market of bisphenol A and phenolic resins.

Nowadays phenol is mainly produced by cumene process (Hock process) which consists of three steps including the alkylation of benzene with propylene to cumene, the oxidation of cumene to cumene hydroperoxide and the acid-cleavage

of cumene hydroperoxide to phenol by H_2SO_4, as shows in Figure 1.3[4]. The disadvantages of cumene process are not only consist of multistage in the process but also produce the explosive intermediate and require the complicated equipment which results in high cost process. Moreover, this process provides an equimolar amount of acetone as by-product that exceeds market demand. Thus, the expansion of this process is restricted by the marketability of acetone. In order to overcome this problem, the direct hydroxylation of benzene to phenol has attracted much attention. A potential route is the direct insertion of a hydroxyl group to the benzene ring via the hydroxylation of benzene. Many researchers study this reaction extensively by using various oxidants such as nitrous oxide, oxygen and hydrogen peroxide.

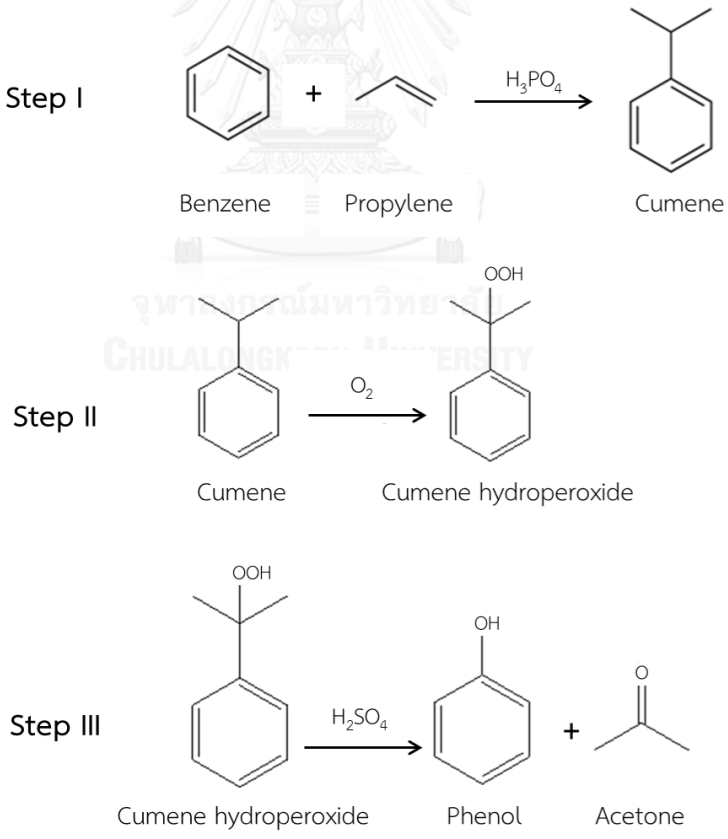

Figure 1.3 Cumene process

1.2 Literature reviews

1.2.1 Benzene hydroxylation by using nitrous oxide (N_2O)

In 2001, Pirutko et al. [5] studied preparation and catalytic properties of metal modified TS-1 in the oxidation of benzene to phenol by nitrous oxide. The metals in this study were Al, V, Cr, Fe, Co and Ru. From the results, other metal-modified TS-1 materials are inert, except for Fe-TS-1 shows catalytic properties in the oxidation of benzene with high activity and selectivity. The ability of catalyst depends on Fe content and specific sites concentration. This catalyst containing 0.95% Fe which activated at 650°C for 2 h providing 7.68% yield of phenol at 400°C, 1.0 g of catalyst, at fed rate 7.2 l/h of mixture of 50 mol% benzene and 5 mol% nitrous oxide.

In 2005, Hronec and Bahidsky [6] studied hydroxylation of benzene with nitrous oxide using copper-calcium-phosphates as a catalyst. The reaction temperature and reaction time were varied in the range of 330°C - 450°C and 1 h – 6 h, respectively. They found that the highest phenol yield of 3.26% was obtained by using 12.3 mmol/h of benzene, 8.1 mmol/h of N_2O and 18.8 mmol/h of N_2 as starting materials over 2 g of copper-calcium-phosphates catalyst. This hydroxylation was operated at 450°C for 2 h and 60.8 mmol/h of H_2O was used as solvent.

In 2007, Yuranov et al. [7] studied hydroxylation of benzene to phenol with N_2O over Fe-Beta and Fe-ZSM-5 catalysts. The reaction temperature was varied from 270°C to 350°C. From the results, both catalysts was deactivated at temperature >297°C due to coke formation. In the hydroxylation of benzene, the highest phenol yield of 7.12% was obtained by using benzene : N_2O mole ratio 1:5, total gas flow = 60 ml/min at 270°C for 2.5 h over 1.0 g of Fe-ZSM-5 (Fe loading 0.58 wt.%) which activated at 1050°C in a He flow (50 ml/min) for 2 h.

Although benzene hydroxylation by using nitrous oxide as oxidant exhibits high selectivity to phenol, the reaction is carried out at high temperature. In addition,

main problem of this process is the deactivation of the catalyst because of heavy coke formation that limits the application of this technology for industrial manufacture.

1.2.2 Benzene hydroxylation by using molecular oxygen (O_2)

In 2003, Battistel et al. [8] studied oxidation of benzene with molecular oxygen to produce phenol using chloride metal salt catalysts such as $CuCl_2$, $FeCl_3$, $TiCl_3$ and VCl_3. The dithiothreitol, ascorbate and mercaptoethanol were used as reducing agents. From the results, they found that the highest 3.5% yield of phenol was obtained by using VCl_3 catalyst and ascorbate reducing agent at 50°C, 17 h, 40 μmol of VCl_3, 1 atm of O_2 and 11.3 mmol of benzene. When reducing agent was changed to dithiothreitol, high hydroquinone selectivity was achieved (0.69% yield) at the same oxidation condition.

In 2006, Lui et al. [9] reported the oxidation of benzene with molecular oxygen over $Pd(OAc)_2$ and heteropolyacid homogeneous catalysts compared to $Pd(OAc)_2$ and heteropolyacid (HPA) immobilized on hexagonal mesoporous silica (HMS) and polyimine (PIM) heterogeneous catalysts. From the results, the heterogeneous catalyst gave similar phenol yield to homogeneous catalyst. Moreover, the highest 16% yield of phenol was obtained by using HMS-HPA + $Pd(OAc)_2$ catalyst at 120°C, 10 h, 0.5 g of catalyst, 2 mL of benzene, 2 mL of acetic acid (reductant) and 2 MPa of O_2.

In 2007, Gu et al. [10] studied hydroxylation of benzene with molecular oxygen in the presence of ascorbic acid as the reducing agent. The catalysts in this study were V-Cu oxide with different supports such as Al_2O_3, SiO_2, HZSM-5, MCM-41 and SBA-15. From results they found that VO_x/CuSBA-15 was a good catalyst for this reaction and the best ratio of V/Cu was 0.24. Furthermore, this catalyst provided 27% yield of phenol and 0.01% yield of benzoquinone and hydroquinone at reaction

condition 80°C, 5 h, 50 mg of catalyst, 11.3 mmol of benzene, 11.9 mmol of ascorbic acid over 0.7 MPa of O_2.

The prominent advantages of benzene hydroxylation with molecular oxygen are the production of less waste and the easy acquirement of raw materials. However, this system usually requires reducing agent such as ascorbic acid, acetic acid, dithiothreitol and mercaptoethanol.

1.2.3 Benzene hydroxylation by using hydrogen peroxide (H_2O_2)

In 2007, Parida and Dash [11] performed oxidation of benzene with hydrogen peroxide using manganese nodule leached residue (MNLR) catalyst. The influences of reaction parameter were studied. It was found that 13.5% yield of phenol, 2.7% yield of hydroquinone and 4.5% yield of benzoquinone were achieved by using 0.05 g of MNLR catalyst, benzene to H_2O_2 mole ratio 1:2, 7.5 mL of acetic acid solvent at room temperature for 100 min.

In 2008, Kong et al. [12] studied hydroxylation of benzene with H_2O_2 over Cu-MCM-41 catalyst. The Cu-MCM-41 material, which contained 26% of copper content, showed excellent catalytic activity in hydroxylation of benzene. From reaction results they found that the best reaction condition was 0.1 g of catalyst, 65°C for 2.5 h and 1:3 mole ratio of benzene to H_2O_2. This hydroxylation condition exhibited 18.4% yield of phenol, 7% yield of hydroquinone and 5.6% yield of catechol.

In 2010, Zhu et al. [13] studied hydroxylation of benzene with H_2O_2 using mesoporous VO_x/SBA-16 catalyst. The effect of vanadium loading on SBA-16 was investigated. From results they found that 14% yield of phenol and 2.5% yield of benzoquinone were obtained from hydroxylation of 0.3 mL benzene with 1.5 mL of H_2O_2 (benzene : H_2O_2 mole ratio 1:5) and 5 mL of acetonitrile over 0.01 g VO_x/SBA-16 (7.3 wt. % V loading) catalyst at 60°C, 4 h.

In 2011, Song et al. [14] studied preparation and catalytic properties of bi-component catalysts, VO_2 supported on multi-walled carbon nanotubes (MWCNTs) with defects as promoters (VO_2-defects/MWCNTs). The effect of defect density on the benzene hydroxylation was investigated. From the results, VO_2-defects/MWCNT with 0.97 defect density shows much higher catalytic activities in the benzene hydroxylation to phenol. The highest 22.95% yield of phenol was obtained by using 0.05 g of catalyst, benzene: hydrogen peroxide mole ratio 1:1.5, 8 mL of acetonitrile at 60°C for 3 h. Moreover, compared with other vanadium catalysts, VO_2-defects/MWCNTs have a much higher catalytic performance than V_2O_5/HZSM-5, V_2O_5/MCM-41 and V_2O_5/Al_2O_3 at the same reaction condition.

In 2015, Wang et al. [15] reported the benzene hydroxylation with H_2O_2 over metal oxide supported graphene oxide (M/GO) catalysts. M/GO catalysts were prepared by the impregnation method. The metals used in this research were V, Fe and Cu. From the results, V/GO with 10 wt.% V-content is the most active catalyst in the benzene hydroxylation reaction. This catalyst provided a phenol yield of 22.7% with good recycle performance. The optimum condition was Benzene : H_2O_2 mole ratio = 1:2.4, 0.04 g of catalyst, 10 ml acetic acid at 65 °C for 3 h.

The benzene hydroxylation by using hydrogen peroxide as the oxidant provides high conversion but low selectivity. Nevertheless, the catalytic oxidation process is simple and easy to handle. Furthermore, the using of hydrogen peroxide in oxidation reaction is usually carried out at mild condition and gives water as the only by-product. Another advantage of hydrogen peroxide is its comparatively low cost. From an economic and environmental standpoint, hydrogen peroxide is chosen as the good oxidizing agent.

1.2.4 Benzene hydroxylation over transition metal catalysts

In 2008, Tanarungsun et al. [16] reported the hydroxylation of benzene with hydrogen peroxide to produce phenol over Fe/TiO_2 loaded with different second metal (Ni, Co, Pd and Pt). In addition, the effect of reaction condition to phenol yield was studied by vary the reaction temperature, reaction time, catalyst amount, H_2O_2 to benzene mole ratio and solvent amount. From results they found that the presence of the second metal in Fe/TiO_2 catalyst increased the phenol yield. The yield of phenol follows the order: Pt > Pd >> Co ~ Ni. The 6.7% yield of phenol was achieved using 0.2 g of $FePt/TiO_2$ catalyst at 30°C, 4 h, benzene : H_2O_2 mole ratio of 1:2, 0.5 g of ascorbic acid.

In 2010, Adam and Thankappan [17] studied the oxidation of benzene with H_2O_2 over bi-metallic Cu-Ce incorporated rice husk silica (RH). It was found that the Cu-Ce/RH catalyst showed good catalytic activity. Furthermore, the 27.8% of phenol, 9.9% of hydroquinone and 41.0% of benzoquinone yield were obtained by using 70 mg of Cu-Ce/RH catalyst at 70°C, 5 h, benzene : H_2O_2 mole ratio of 1:2 in 10 mL acetonitrile.

In 2013, Dan et al. [18] studied liquid phase hydroxylation of benzene to phenol with hydrogen peroxide over VO_x-TiO_2 catalyst (4.3% of V-content) with Cu as a second metal. The effect of reaction condition to phenol yield such as amount of Cu loading, reaction time, reaction temperature and amount of catalyst were also studied. From the results, Cu not only improved thermal stability of Cu/VO_x-TiO_2 but also promoted the mono dispersion of the vanadium species on the surface. The maximum 25.6% yield of phenol yield was obtained by using benzene : H_2O_2 mole ratio of 1:2, 5 ml of acetonitrile and 0.18 g of Cu/VO_x-TiO_2 catalyst with Cu content of 0.75% at 60 °C for 5 h.

In 2014, Hu et al. [19] studied the benzene hydroxylation to phenol over Cu-V bimetal modified HMS catalysts with different copper content. From the results they found that Cu-V-HMS which containing 0.9 Cu/V molar ratio exhibited the best catalytic activity with a phenol yield 29 % at the reaction condition 0.1 g of catalyst, benzene : H_2O_2 mole ratio = 1:2.75, 24 mL of acetic acid (80 wt.%), 70°C for 3 h. Furthermore, this catalyst could be reused five times without losing activity for benzene hydroxylation reaction.

In 2014, Ye et al. [20] studied oxidation of benzene to phenol over hybrid catalyst of TS-1 under visible light irradiation. The Fe-CN/TS-1 hybrid catalysts were synthesized by a facial thermal polymerization using dicyandiamide, metal chloride as precursors and TS-1 zeolite as a support. From the results, Fe-CN/TS-1 catalyst with 6% Fe/Cl_3 showed good catalytic activity. The optimal condition to produce phenol was Benzene : H_2O_2 mole ratio = 1:0.56, 0.05 g of catalyst, 4 ml of water and 4 ml of acetonitrile at 60 ℃ for 4 h provided 10.0% yield of phenol.

Many transition metals such as Ce, Co, Cu, Fe, Ni, Pd, Pt, Ti and V were used to catalyze the hydroxylation of benzene to phenol. Among various transition metals, Ce, Cu, Fe, Ti and V show good catalytic performance in benzene hydroxylation. In this work, Ti is selected as the main element for synthesis of microporous and mesoporous titanolisicates, which is one of the high potential catalysts in oxidation field. The effective transition metals (Ce, Cu, Fe and V) are immobilized on titanosilicate support as a second metal in order to improve catalytic activity of catalysts. The prepared catalysts are tested in benzene hydroxylation reaction using hydrogen peroxide as oxidizing agent.

1.3 Objectives

1.3.1 To prepare transition metal-titanosilicate catalysts for using in benzene hydroxylation.

1.3.2 To test the catalytic activity of synthesized catalysts in benzene hydroxylation using hydrogen peroxide as oxidant and investigate the optimum condition.

1.4 Scopes of work

This project involves microporous and mesoporous titanosilicates preparation together with the introduction of transition metal such as cerium, copper, iron or vanadium into titanosilicate support producing bimetallic catalysts. All of synthesized catalysts will be characterized by XRD, DR-UV, surface area analyzer, SEM, TEM and ICP-MS. After that, the bimetallic catalysts will be tested in benzene hydroxylation with hydrogen peroxide and studied the effect of reaction parameters on the yield of product. Moreover, the reusability of catalysts will be investigated.

CHAPTER II

THEORY

2.1 Catalysts

The Rate of chemical reactions depending on various factors such as reaction temperature, concentration of reactants, pressure, nature of reactants and others. One of the most important factors that influence the reaction rate is catalyst. A Catalyst is a compound that accelerates the progress of a reaction without being consumed. When the reaction has finished, the mass of catalyst is the same as at the beginning. Moreover, it does not affect the equilibrium state of a reaction. Catalyst participates in a chemical reaction by reducing the activation energy resulting in the increase of reaction rate. The energy profiles of the reaction with and without catalyst were shown in Figure 2.1. In the presence of catalyst, it provides an alternative route to products which requiring lower activation energy than uncatalyzed reaction. In addition, the using of catalyst in the reaction makes process to work effectively. The effective chemical process usually means that a chemical compound can be made more cheaply and cleanly. Therefore, catalysts are essential and necessary for industry.

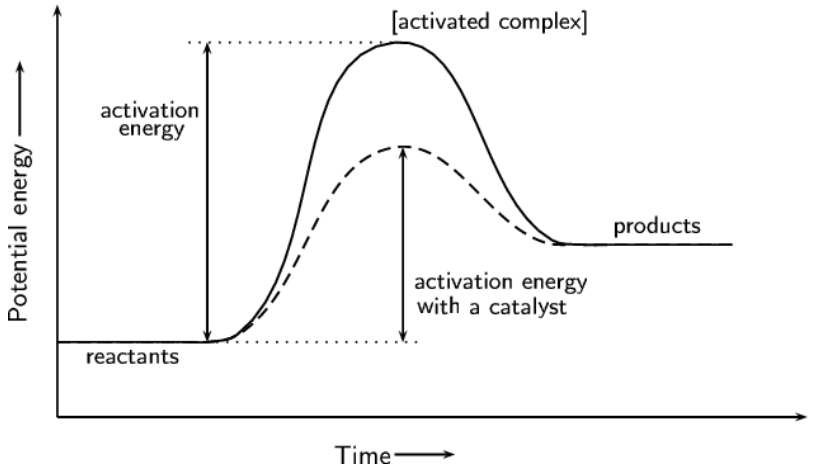

Figure 2.1 The energy profiles of the reaction with and without catalyst [21].

The important properties of industrial catalysts

- **Activity** of catalyst is an ability to increase reaction rate or progress the reaction process of catalyst. It can be defined in terms of kinetics or from a more practically oriented viewpoint.
- **Selectivity** of catalyst is an ability of catalyst that can convert reactants to desired product. This is termed as the selectivity of catalyst, which expressing by the ratio of the amount of particular product to the total product in the reaction. The selective catalyst can accelerate a particular reaction while inhibit another reaction.
- **Stability** to chemical, thermal and mechanical is the essential properties of catalyst. This can be determined by its lifetime in industrial reactors. The total catalyst lifetime is of crucial importance for the economics of a process. The numerous factors such as decomposition, coking, and poisoning also influence the stability of catalyst.

2.1.1 Types of catalysts

Catalysts can be classified in two main types on the basis of phases of reactant, products and catalyst [22].

2.1.1.1 Homogeneous catalysts

In homogeneous catalysis, catalyst, reactants, and products are present in the same phase resulting in higher degree of dispersion than heterogeneous catalysts. The high mobility of molecules in the reaction mixture makes more collisions with reactant molecules. Thus, the reactants can approach the catalytically active center from any direction leading to high catalytic activity. However, the major drawback of homogeneous catalyst is the difficulty of their

recovery from the product. More complicated processes such as distillation, liquid–liquid extraction, and ion exchange must often use to separate catalyst. Therefore, homogeneous catalysts are less frequently used in the industry.

2.1.1.2 Heterogeneous catalysts

In the heterogeneous catalysis, phase boundaries are always present between the catalyst and the reactants. Generally the catalyst is a solid, and the reactants are gases or liquids. In the catalytic process, reactant molecules are adsorbed on active sites of the catalyst. The interaction of catalyst and reactant are occurred. After that, catalyst converts the reactant molecules to product molecules. Later product molecules are desorbed from the active sites. Although heterogeneous catalysts exhibit a lower activity than homogeneous catalyst, the use of heterogeneous catalysts is always advantageous from both environmental and economic points of view due to its efficient recycling and easy handling. Heterogeneous catalyst can be separated by simple methods such as filtration or centrifugation.

Table 2.1 Comparison of homogeneous and heterogeneous catalysts

Consideration	Homogeneous catalyst	Heterogeneous catalyst
Active centers	All metal atoms	Only surface atoms
Concentration	Low	High
Selectivity	High	Lower
Diffusion problems	Practically absent	Present (mass-transfer-controlled reaction)
Reaction conditions	Mild (50–200°C)	Severe (often>250°C)
Applicability	Limited	Wide
Activity loss	Irreversible reaction with products (cluster formation), poisoning	Sintering of the metal crystallites, poisoning
Modification possibilities	High	Low
Thermal stability	Low	High
Catalyst separation	chemical decomposition, distillation, extraction	Fixed-bed: unnecessary suspension: filtration
Catalyst recycling	Possible	Unnecessary (fixed-bed) or easy (suspension)
Cost of catalyst losses	High	Low

2.2 Porous materials

Porous materials are extensively used in many applications including catalyst, adsorbents and catalyst supports because of high specific surface areas, uniform pore size, large pore volume and excellent mechanical stability. According to IUPAC definitions, porous material can be classified into three groups based on their pore sizes namely microporous materials, mesoporous materials and macroporous materials. The difference in the pore sizes of porous materials relates to their ability to perform the desired function in a particular application. Properties and examples of these materials are given in Table 2.2.

Table 2.2 IUPAC Classification of porous materials [23]

Type of porous material	Pore size (Å)	Examples
Microporous materials	< 20	ZSM-5, MOF-5
Mesoporous materials	20 – 500	M41s, SBA-15, Pillared clays
Macroporous materials	> 500	Glasses, Foams

2.2.1 Microporous materials

Microporous materials are subdivided into two groups in term of ultramicropores (less than 7 Å) and supermicropores (7-20 Å). Zeolites, a material with uniform micropores, are well-known members of the microporous materials. Zeolites are microporous aluminosilicates, which construct from TO_4 tetrahedra (T = tetrahedral atom e.g. Si, Al) connect by oxygen atoms. The primary building units of zeolites are shown in Figure 2.2 [24]. This primary building units are linked together to form secondary building units (SBU), as can be seen in Figure 2.3 [25].

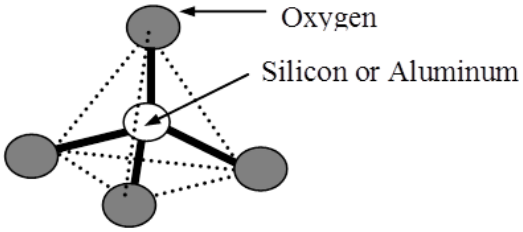

Figure 2.2 Primary building units of zeolites

Most porous material frameworks can be built from numerous different secondary building units. For example, the framework of sodalite can be generated from either the single 6-member ring or the single 4-member ring.

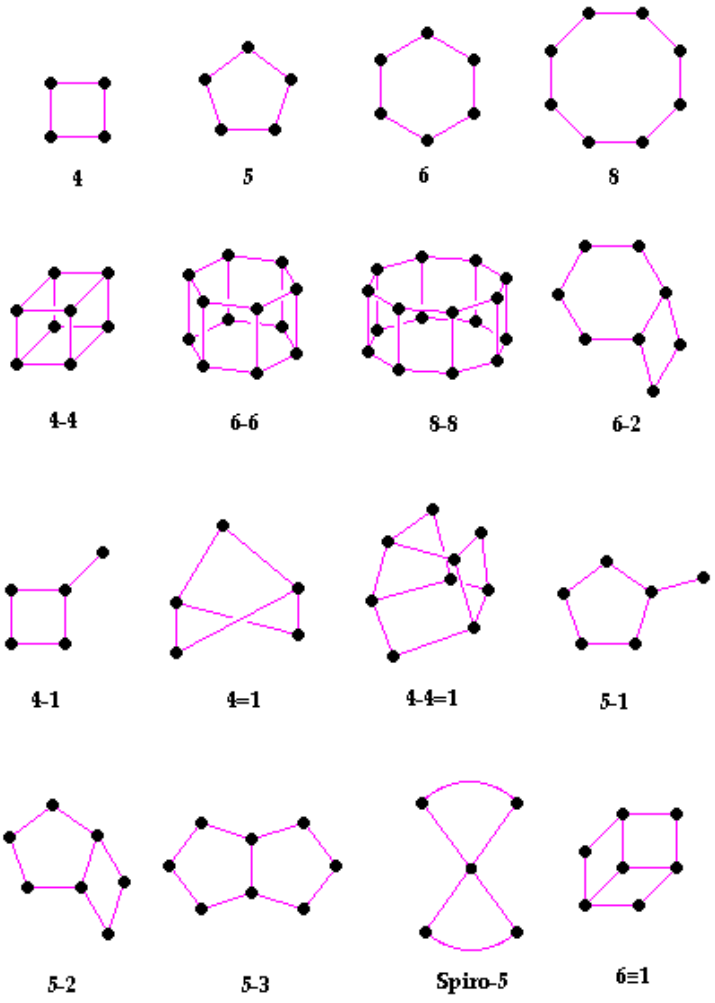

Figure 2.3 Secondary building units (SBU) in zeolite structure.

Zeolites have the ability to act as catalysts for chemical reactions which taking place within the internal cavities. The catalytic ability of zeolites is cause by the following properties.

1. Shape-selectivity properties

The first prominent properties of zeolites, which making them particularly suitable as catalysts are shape selectivity. The shape selectivity in zeolites can be divided into 3 types, (i) reactant shape selectivity; (ii) product shape selectivity and (iii) transition-state shape selectivity. These types of shape selectivity are shown in Figure 2.4. Zeolites are crystalline porous materials with inflexible pore. Thus, only suitable shape and size of reactant can diffuse into the interior of the pores of zeolite. The substrate molecules that lager dimensions than zeolite pore cannot react. Product shape selectivity means that only products of certain size and shape can escape from the zeolite pore. The transition-state shape selectivity is arising from the local environment around the active site. The rate steady for a certain reaction mechanism is reduced if the necessary transition state is too bulky to form readily [26].

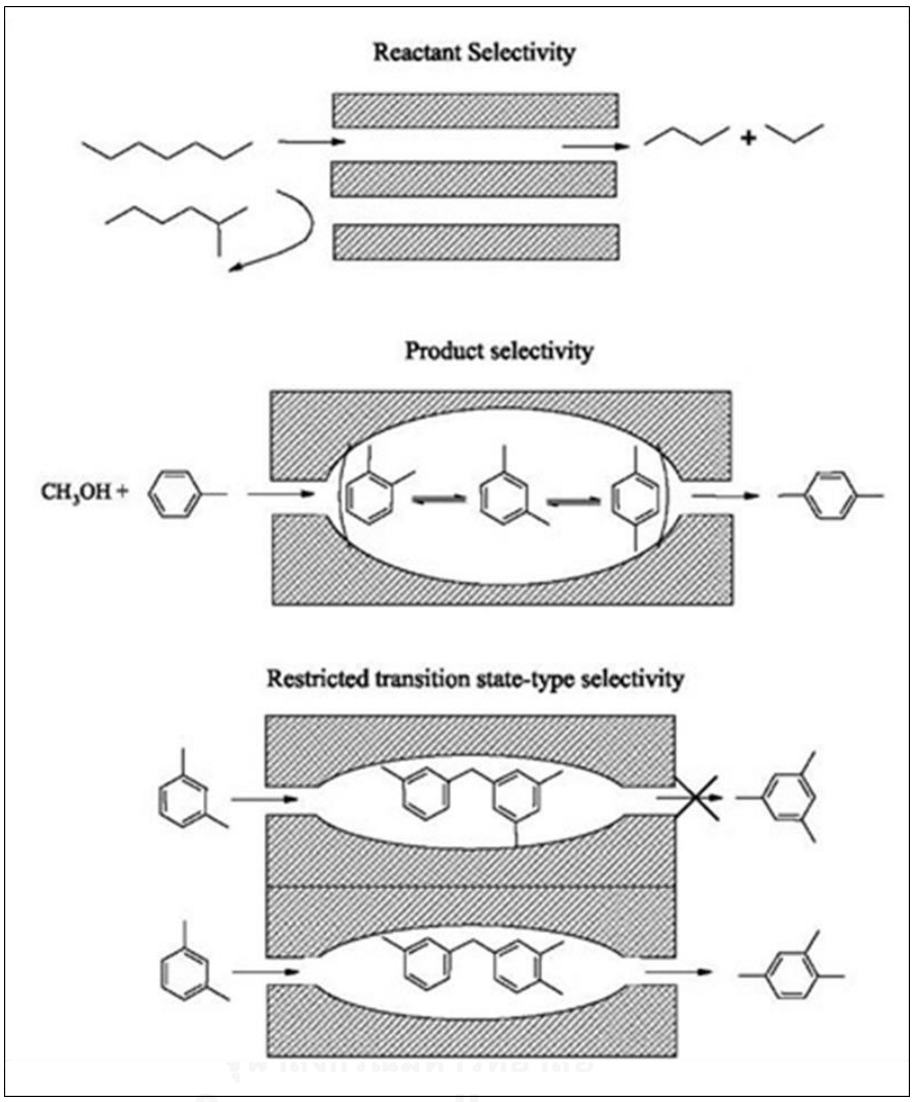

Figure 2.4 Three types of selectivity in zeolites

2. Chemical properties

Zeolites are cation exchangers. It means that various kinds of cations with different catalytic properties can introduce into their intra pore system. Therefore, it can create different catalytic properties not only as acid catalyst. Zeolites can also serve as redox catalysts by the incorporation of redox metals such as titanium, vanadium, iron and chromium.

Titanium-containing zeolites are one of the most efficient catalysts for oxidation reaction. The presence of Ti^{4+} demonstrated specific catalytic properties which have been taken advantage in promiscuity of oxidation reaction.

2.2.1.1 Titanium silicalite-1 (TS-1)

Titanium silicalite-1 (TS-1), discovering for the first time in 1983 by Taramasso et al., is a material with MFI structure. The MFI structure is built up by 5-1 secondary building units which are link together to form chain and interconnection of this chains leading to the formation of the channel system in the structure [27]. Figure 2.5 illustrates MFI structure and channel system in Titanium silicalite-1 catalysts. The MFI-type structure has a three dimensional pore system, which is a combination of sinusoidal (zigzag) 10-membered ring channels (0.51-0.55 nm), that directed along the a-axis, and the intersecting straight 10-membered ring channels (0.54-0.56 nm) that run parallel to the b-axis of the orthorhombic unit cell. The catalytic activity of TS-1 is associated with the isolated Ti^{4+} ions that present into the MFI framework as T-atoms. For the application, the main use of TS-1 is in the oxidation reaction of alkanes, alkenes and aromatic hydrocarbons in the presence of hydrogen peroxide [28, 29].

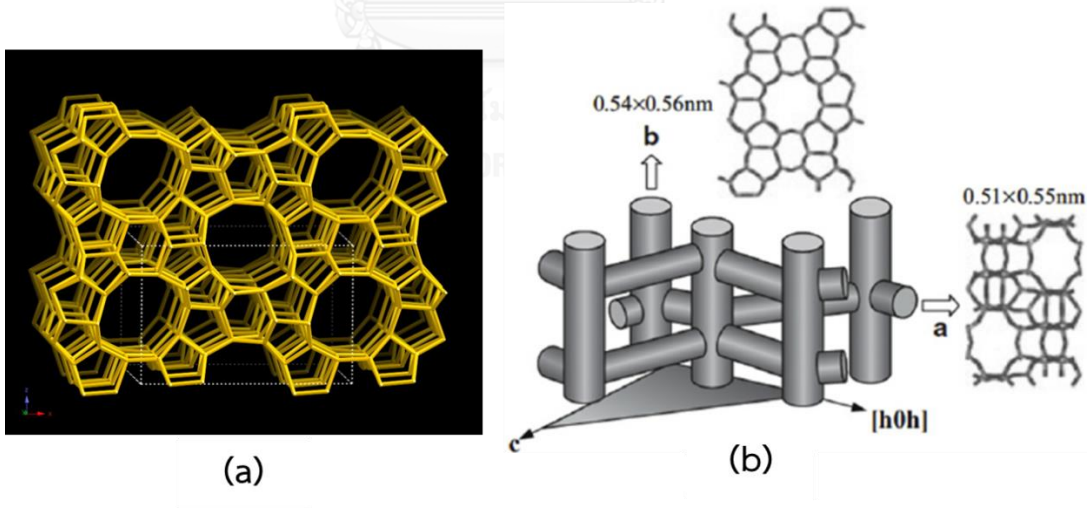

Figure 2.5 (a) MFI structure and (b) channel system in Titanium silicalite-1 catalysts.

2.2.1.2 Titanium Mobil composition of matter tWenty tWo (Ti-MWW)

Titanium Mobil composition of matter tWenty tWo (Ti-MWW) is a Ti-containing zeolite with MWW topology [30]. The MWW structure is constructed from a lamellar precursor (2-dimensional structure) undergoing dehydroxylation upon calcinations between the layered generating the MWW with 3-dimensional structure, as can be seen in Figure 2.6(a). MWW framework topology is consists of two independent channel systems. Figure 2.6(c) show the channel systems in MWW structure. One of the channel systems is 2-dimensional, defined by 10-membered ring sinusoidal channels within the layers. The other pore system is 3-dimensional, defined by 12-membered ring channels between the layers. The supercages turn out to be pocket or cup moieties 0.7 × 0.7 nm at the crystal exterior. The supercages and exterior pockets are considered to serve as the open reaction spaces for reactants. Therefore, Ti-MWW is chosen as one of the most efficient catalysts for oxidation reaction.

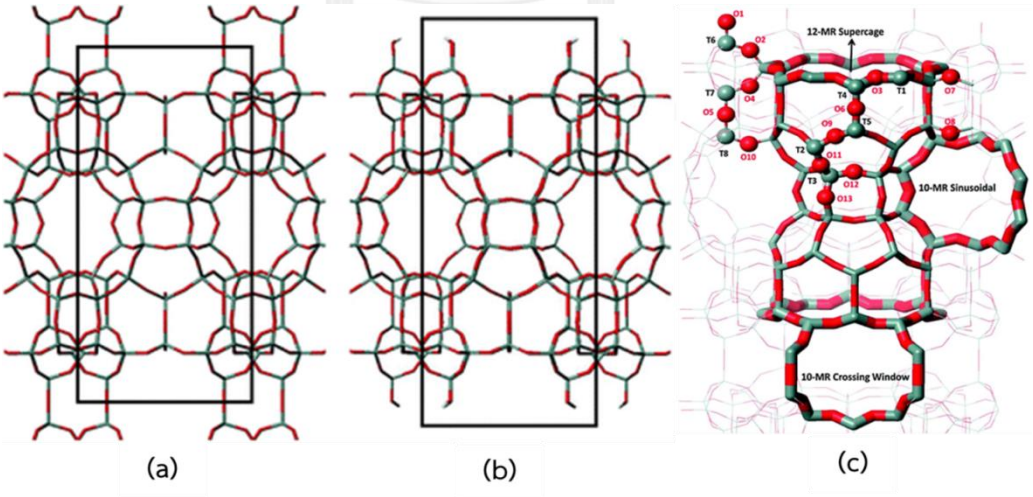

Figure 2.6 (a) Structure of the 3-Dimensional MWW zeolites.

(b) Structure of the 2-Dimensional MWW zeolites.

(c) Two independent channel systems in MWW structure.

2.2.2 Mesoporous material

Mesoporous materials can be grouped into three classes based on synthetic procedures, as shown in Table 2.3.

Table 2.3 Classification of mesoporous materials

Assembly	Template	Media	Material
Electrostatic	Quaternary ammonium salt	Based or acid	MCM-41
H-bonding	Primary amine	Neutral	HMS
H-bonding	Amphiphilic triblock copolymer	Acid (pH<2)	SBA-15

2.2.2.1 Santa Barbara Amorphous (SBA-15)

SBA-15 mesoporous material with 2-dimensional hexagonal structure (Figure 2.7) has been synthesized under acidic condition using tri-block copolymer as a structure directing agent [31]. The SBA-15 mesoporous material exhibits high hydrothermal stability when compare with MCM-41 because of its thicker pore walls (3.1-6.4 nm). The high internal surface area of typically 400–900 m^2/g together with a tunable pore diameter of between 5 and 15 nm makes SBA-15 as a well suited material for various applications such as catalyst support, adsorption and separation in environmental analytics [32, 33].

Figure 2.7 2-Dimensional hexagonal structure of SBA-15.

2.2.2.2 Mesoporous Cubic *Ia-3d* Amorphous (MCA)

Large-pore mesoporous silica with cubic *Ia-3d* has been synthesized by using tri-block copolymer Pluronic 123 ($EO_{20}PO_{70}EO_{20}$) as a template [34]. The cubic *Ia3d* mesoporous silica (MCA) has a three-dimensional (3D) structure similar to MCM-48, which was synthesized by using cetyltrimethylammonium bromide (CTAB) as the template [35]. The comparison of MCA and MCM-48 properties are given in Table 2.4. The prominent advantage of MCA is the larger pore size (>5 nm) than MCM-48 that attracting considerable attention for potential applications. In the catalytic applications, many researchers have concentrated on the surface modification by adding organic-inorganic functional groups such as sulfonic groups and amino groups. However, few researchers have paid attention to their property in catalyst support.

Table 2.4 Comparison of MCA and MCM-48 properties.

Properties	MCA	MCM-48
Pore size (nm)	5.3-7.5	3.1-3.3
Pore volume (cm^3/g)	1.03-1.30	0.53-0.80
Surface area (m^2/g)	1022-1152	660-1010

2.3 Benzene hydroxylation

Benzene hydroxylation reaction is one of the most important and economically attractive reactions. A potential route is the direct insertion of a hydroxyl group to the benzene ring via the hydroxylation of benzene. The main product is phenol which is an important chemical intermediate for the synthesis of bisphenol-A, phenolic resins, and alkylphenols. Moreover, diphenol isomers (hydroquinone and cathechol) are produce as hydroxylated by-products. In recent reports, the numerous oxidizing agents such as nitrous oxide, molecular oxygen and hydrogen peroxide were used in benzene hydroxylation. Hydrogen peroxide is the most promising oxidant because process is simple, cheap and environmentally friendly. In addition, many researchers try to develop the benzene hydroxylation capacity of catalysts. However, titanosilicate is one of the most popular catalysts for the oxidation reaction such as TS-1 [36], Ti-SBA-15 [37] and Ti-MCM-41 [38]. Furthermore, redox elements such as iron, chromium, copper and vanadium can improve the redox catalytic properties.

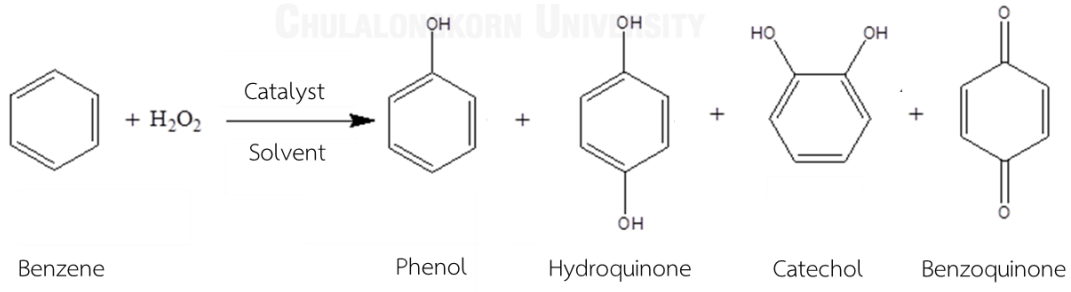

Scheme 2.1 Typical hydroxylation diagram of benzene

2.4 Material characterization

2.4.1 X-ray powder diffraction (XRD)

X-ray powder diffraction (XRD) is a non-destructive technique, which is known for the characterization of crystalline materials. Moreover, this technique can provide information on unit cell dimensions.

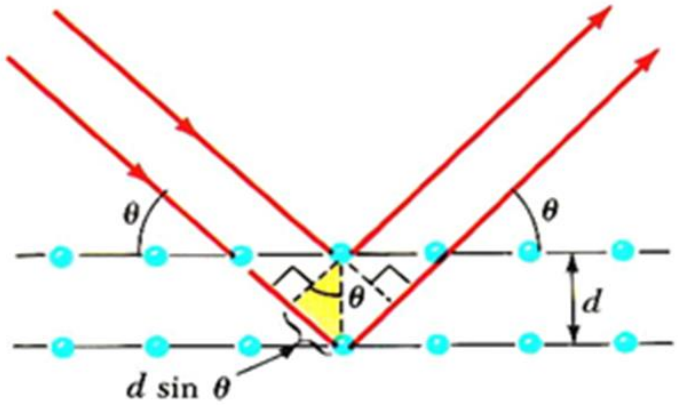

Figure 2.8 Diffraction of X-ray by regular planes of atoms [39].

In XRD, polychromatic X-rays are produced from a special tube called cathode-ray tube under vacuum atmosphere. After that, polychromatic X-rays are filter through a monochromator producing monochromatic radiation. A monochromatic X-ray beam is focused on sample in order to resolve structural information in the crystal lattice. Usually, the materials are composed of repeating uniform atomic planes which make up their crystal. Interactions of incident X-rays with the sample atomic planes (Figure 2.8) create diffracted, transmitted, refracted, scattered and absorbed beams according to Bragg's law, which is given below:

$$n\lambda = 2d \sin\theta$$

Where n = an integer defining order of diffracted beam

λ = wavelength of the incident X-ray beam

d = the distance between near atomic planes or d-spacings

θ = the angle of the incidence X-ray

After that, diffracted X-rays, which reflecting the physico-chemical characteristics of the crystalline materials are detected by detector followed by processing and counting of the diffracted rays to give X-ray diffractograme. Therefore, the XRD peaks are produced via a constructive interference of X-ray beam scattered at specific angles from each lattice plane of a sample. The peak intensity depends on arranging and distribution of atoms within the crystal lattice.

2.4.2 DR-UV spectroscopy

The DR-UV spectrometer is the instrument, which uses to provide information on the electronic structure of molecules, the valence and coordination of metal cations. The DR-UV spectrometer was used to study oxidation state of various metals containing in microporous and mesoporous catalysts. The UV-vis spectrum can give information about the oxidation state and the environmental symmetry of transition metal ions, e.g. tetrahedrally or octahedrally coordinated ions and the degree of polymerization.

Solid sample in form of powders are measured in reflectance mode owing to low transparency. In order to collect diffuse reflected light, integration spheres are used in UV-Vis spectrometers. The DR-UV-vis spectrum can be described by the Kubelka-Munk function *F*:

$$F = \frac{\left(1 - \tilde{R}_{Norm}\right)^2}{2\tilde{R}_{Norm}}$$

$$\tilde{R}_{Norm} = \frac{\tilde{R}_{sample}}{\tilde{R}_{ref}}$$

With R_{sample}= The reflectance of sample

R_{ref} = The reflectance of a reference material with a reflectance of 100% ("white standard")

2.4.3 Nitrogen adsorption-desorption technique

The physical properties such as surface area, pore volume, pore diameter and pore size distribution of microporous and mesoporous material are determined by nitrogen adsorption-desorption technique. According to IUPAC, adsorption-desorption isotherms are classified into six types [40], as can be seen in Figure 2.9. The type of adsorbate and type of adsorbents including intermolecular interaction between gas and surface influence the type of isotherms. The isotherm type I is obtained when adsorption is limited to only a few molecular layers corresponding to microporous material. Type II shows the isotherm for nonporous while type III is typical behavior for macroporous or nonporous materials owing to a relatively weak interaction between adsorbate and adsorbent. The isotherm type IV with hysteresis loop is the adsorption behavior of mesoporous materials. Type V is a combination of type IV and

type III while type VI is a special case that represents step-by-step adsorption of multilayers. The features of adsorption isotherms are summarized in Table 2.5.

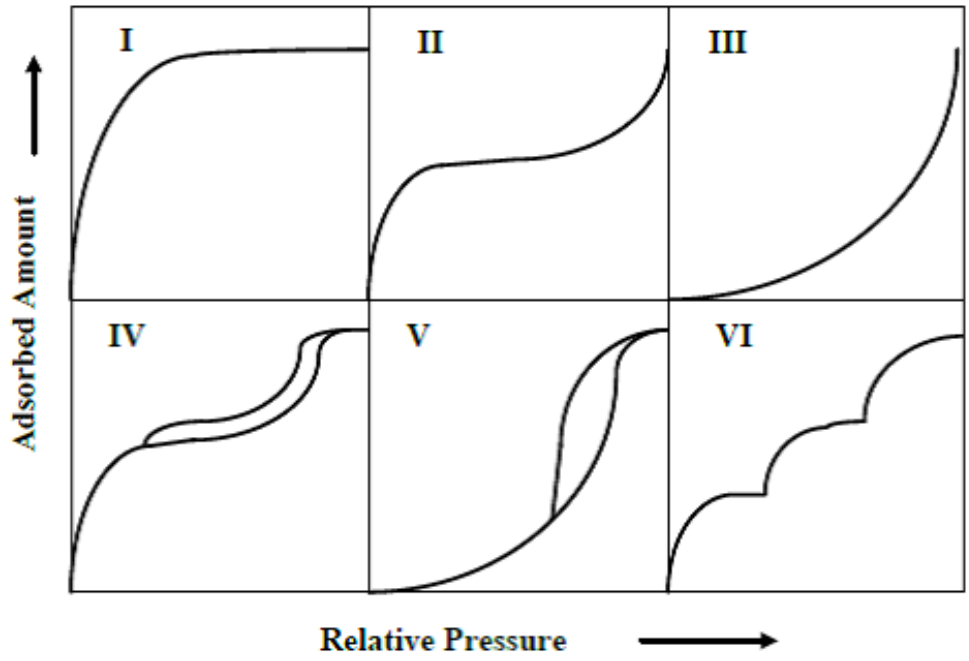

Figure 2.9 The IUPAC classification of adsorption isotherm [41].

Table 2.5 The features of adsorption isotherms.

Type	Features	
	Interaction between sample surface and adsorbate	Porosity
I	Relatively strong	Microporous
II	Relatively strong	Nonporous
III	Weak	macroporous or nonporous
IV	Relatively strong	Mesoporous
V	Weak	Microporous or mesoporous
VI	Relatively strong, Sample surface has an even distribution of energy	Nonporous

Hysteresis loop is presented due to the capillary condensation taking place in the mesopores. Furthermore, the first part of the curve is attributed to the monolayer adsorption. Therefore, hysteresis loop is a sign of porosity. The IUPAC classification of hysteresis loop in sorption isotherm is shown in Figure 2.10. H1 type relates to well-defined cylindrical pores or close agglomerates of uniform spheres while H2 type demonstrates some disorder in the pore structure. It means that pore size distribution and shape are not well-defined. Moreover, H3 indicates the occurrence of slit pores and H4 stands for slit pores with a large number of micropores.

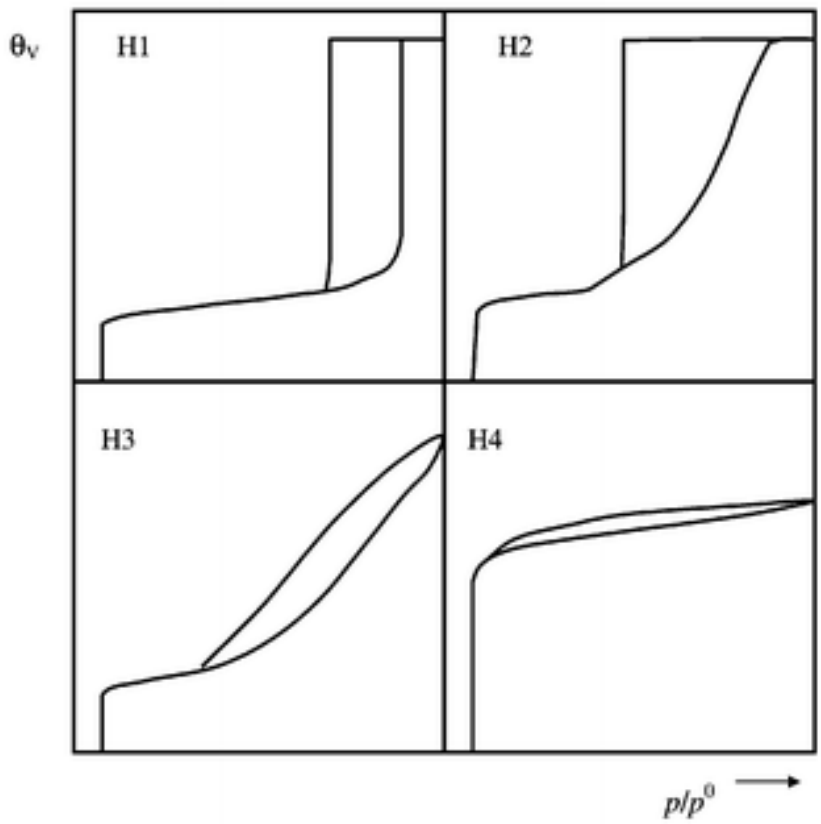

Figure 2.10 IUPAC classification of hysteresis loop in sorption isotherm.

Different models of calculating the surface area can be applied to the adsorption isotherm. Among of them, the isotherm model of Brunauer, Emmet and Teller (BET) is widely used for the calculation of total surface area. The equation for the propose is given by [42]

$$\frac{1}{W[(P_o/P)-1]} = \frac{1}{W_m C} + \frac{C-1}{W_m C}(P/P_o)$$

Where W = weight of nitrogen adsorbed at a given *P/Po*

W_m = weight of gas to give monolayer coverage

C = BET constant that related to the heat of adsorption

The quantity of nitrogen adsorbed in the monolayer can be determined by a slope and intercept. The surface area is calculated by using the equation below [42].

$$S_{total} = \frac{V_m N \sigma}{M}$$

Where S_{total} = total surface area,

N = Avogadro's number

σ = the gas cross section which is 0.162 nm^2 for the molecules of nitrogen gas.

2.4.4 Scanning electron microscopy (SEM)

The scanning electron microscope (SEM) is the instrument, which uses a focused scanned electron beam to produce images of the sample. The samples are scanned with the primary electron beam that generating a variety of signals at the surface of samples. These signals include secondary electrons, backscattered electrons, diffracted backscattered electrons and photons are leaved from its surface. The derived signals reveal information about the sample such as morphology, chemical composition and homogeneity of sample. Secondary electrons and backscattered electrons are used for imaging samples. Secondary electrons are most valuable for showing morphology and topography on samples while backscattered electrons are most valuable for illustrating contrasts in composition in multiphase samples. Then, after the electron beam generates electron emissions from the sample, a photomultiplier collect and amplify these electrons. Later, the electrons are converted into a signal visible on a monitor screen. The scanning electron micrograph results 3-dimension black and white images.

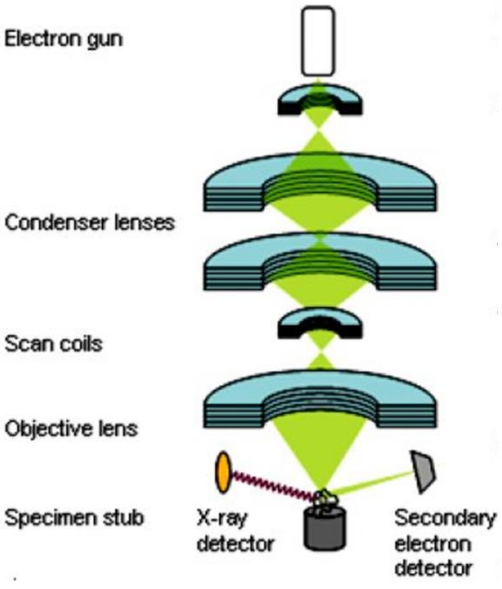

Figure 2.11.Schematic diagram of scanning electron microscope.

2.4.5 Transmission electron microscopy (TEM)

Transmission electron microscope (TEM) is kind of microscope that allows to see the internal structure of materials. The electron beam is generated by an electron gun. Then, the produced electron beams are focused into a thin beam by electromagnetic lenses under high vacuum conditions. This beam strikes through the specimen and parts of it are transmitted. The transmission capacity depends on the thickness and electron transparency of the specimen. After that, the images are magnified by a series of magnetic lenses and then are detected by the CCD camera, which displaying in real time on a monitor or computer. The transmission electron micrograph results 2-dimension black and white images.

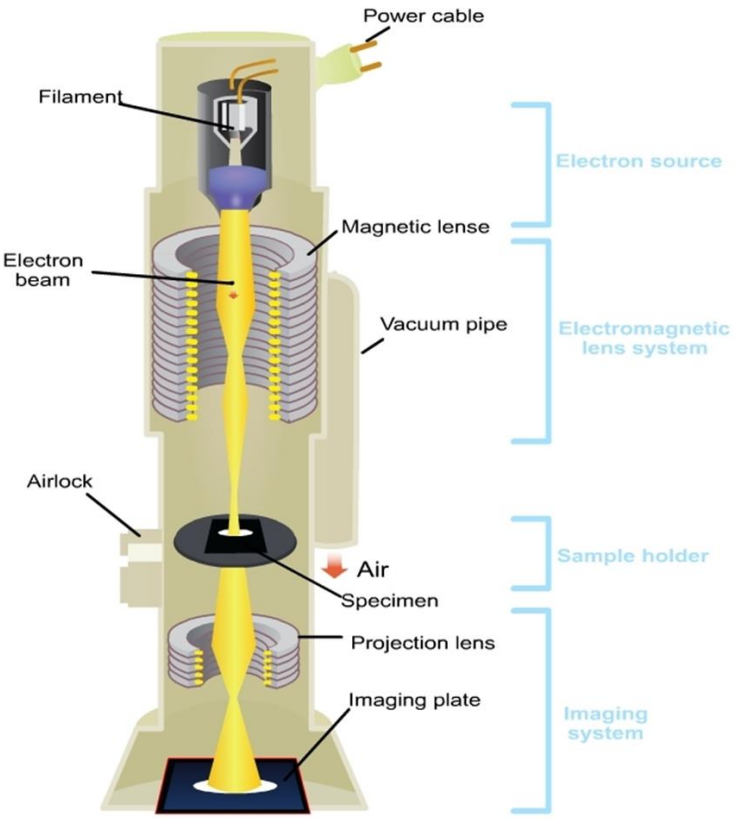

Figure 2.12. Schematic diagram of transmission electron microscope [43]..

2.4.6 Inductively Coupled Plasma Mass Spectroscopy (ICP-MS)

Inductively Coupled Plasma Mass Spectrometer (ICP-MS) combines mass spectrometric detector with an inductively coupled plasma source. It can analyze metal elements from lithium to uranium with the concentration from 0.1 ppm to 1 wt.%

In principle, solutions are vaporized using a nebulizer while solid samples can be examined using laser ablation. In order to split material into individual atoms, the samples are introduced into high-energy argon plasma that consists of electrons and positively charged argon ion. Then, this material atom show positive charge. In the hot plasma, most of elements ionize very efficiently (>90%). To allow their identification, the elemental ions must be transferred from 7000K to room temperature and from atmospheric pressure to high vacuum. After that, the ions are extracted through a number of apertures. Subsequently, the ion beam enters the quadrupole mass analyser. In the quadrupole, the ions are separated on the basis of their mass-to-charge ratio using quadrupole mass filter which only allow ion of a single mass-to-charge ratio pass the rod to the detector.

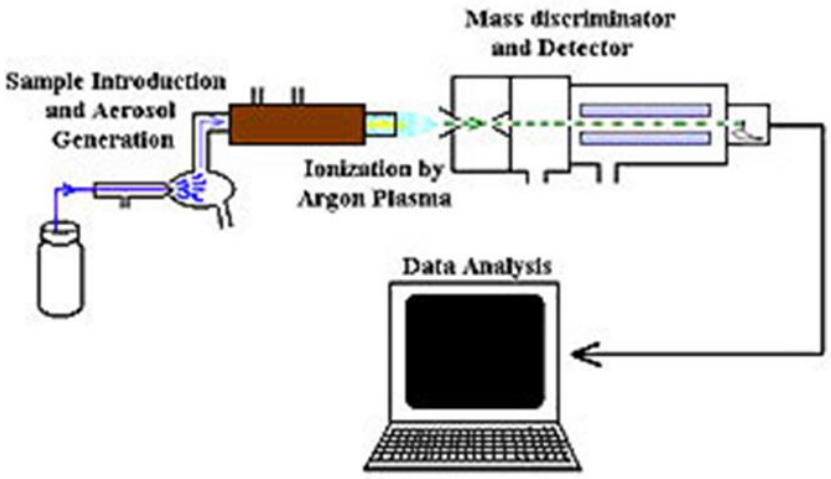

Figure 2.13 The process in ICP-MS [44].

CHAPTER III
EXPERIMENTS

3.1 Instruments and apparatus

3.1.1 Oven and furnace

The crystallization of SBA-15, Ti-SBA-15 and Ti-MCA was carried out at a required temperature using UM-500 oven. The calcination of samples at elevated temperature was performed on a Lenton AWF furnace with heating rate of 1°C/min in order to remove organic template, moisture and impurities from catalytic channels.

3.1.2 X-ray powder diffraction (XRD)

The X-ray diffraction patterns of prepared catalysts were determined by a Rigaku, Dmax 2200/Ultima^{+} diffractometer using a monochromator with Cu K**α** radiation (40 kV 30 mA). For the analysis of crystalline structure, the range of 2-theta, scan speed, scan step, scattering slit, divergent slit and receiving slit of all catalysts are shown in Table 3.1 while the metallic phase of second metal on the support was approved over 2-theta range of 10.0 to 80.0 degree with scan speed, scan step, scattering slit, divergent slit and receiving slit of 1 degree/min, 0.02 degree, 0.5 degree, 0.5 degree and 0.3 mm, respectively. The measured diffractograms were analyzed using Material Database Incorporation (MDI) software.

Table 3.1 The operational parameters of X-ray powder diffractometer.

Catalyst support	2-theta (degree)	scan speed (degree/min)	scan step (degree)	scattering slit (degree)	divergent slit (degree)	receiving slit (mm)
Silicalite-1	5-50	5	0.02	0.5	0.5	0.3
TS-1	5-50	5	0.02	0.5	0.5	0.3
Ti-MWW	2-40	5	0.02	0.5	0.5	0.3
SBA-15	0.7-3	1	0.02	0.05	0.5	0.15
Ti-SBA-15	0.7-3	1	0.02	0.05	0.5	0.15
Ti-MCA	0.7-3	1	0.02	0.05	0.5	0.15

3.1.3 DR-UV spectroscopy (DR-UV)

The diffuse reflectance UV spectra were recorded in the range of 200-700 nm by a Shimadzu UV-2550 spectrophotometer with $BaSO_4$ as reference under ambient temperature. The spectra of metal oxide species were collected in order to prove the metal position.

3.1.4 Surface area analyzer

The characterization of catalyst porosity in terms of nitrogen adsorption-desorption isotherms, specific surface area, pore size distribution and pore volume of prepared catalysts were carried out using a BEL Japan, BELSORP-mini nitrogen adsorptometer at 77 K. Before the measurement, 40 mg of calcined sample was weighed and pretreated at 180°C for 3 h.

3.1.5 Scanning electron microscopy (SEM)

The morphology and particles size of bimetallic catalysts were analyzed by JEOL JSM-6480LV scanning electron microscopy with 15 kV of acceleration voltage. All samples were coated with sputtering gold under vacuum for conductivity.

3.1.6 Transmission electron microscope (TEM)

The dispersion of metallic particles, microstructure and mesostructure of materials were investigated by JEOL; JEM-2010 transmission electron microscope (TEM).

3.1.7 Inductively Coupled Plasma Mass Spectroscopy (ICP-MS)

The Thermo Scientific, iCAP Qc inductively coupled plasma-mass spectrometer was used for analyzing metal content in the samples.

3.1.8 Gas chromatography analysis (GC)

A Varian CP 3800 gas chromatograph equipped with a 25 m length × 0.32 mm inner diameter of HP-1 capillary column was used to analyze reaction mixture from benzene hydroxylation. The liquid sample volume was 1 μL. Flame ionization detector (FID) was used as a detector. The heating program of column oven was illustrated in Scheme 3.1.

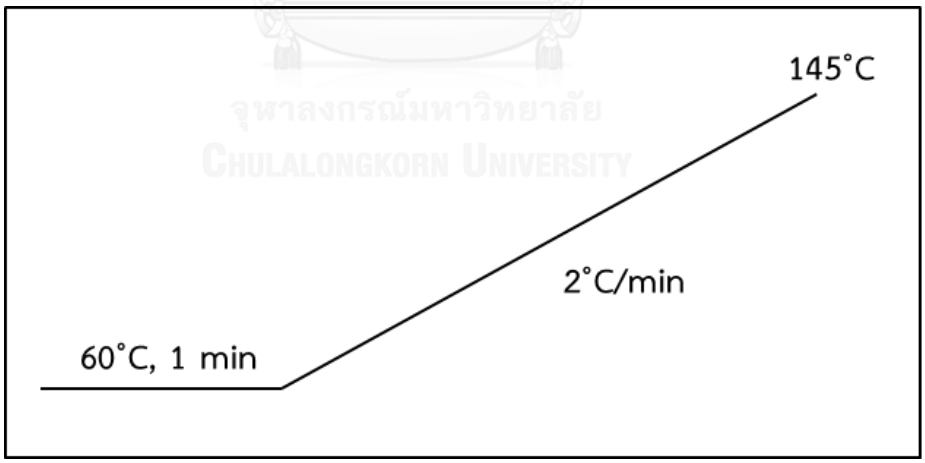

Scheme 3.1 The heating program for Gas chromatography analysis.

3.2 Chemicals

3.2.1 Chemicals for synthesis catalyst

1. Ammonia solution, NH_3 (Merck, 25%)
2. Boric acid, H_3BO_3 (Merck, 99.5%)
3. Cerium (III) nitrate hexahydrate, $Ce(NO_3)_3.6H_2O$ (Merck, 99.9%)
4. Copper (II) nitrate trihydrate, $Cu(NO_3)_2.3H_2O$ (Merck, 99.5%)
5. Ethanol (Merck)
6. Fumed silica (Aldrich)
7. Hexamethyleneimine, HMI (Aldrich, 99%)
8. Hydrochloric acid, HCl (Merck, 37 wt.%)
9. Iron (III) nitrate nonahydrate, $Fe(NO_3)_3.9H_2O$ (Merck, 99%)
10. 3-(mercaptopopyl) trimethoxysilane, MPTMS (Aldrich, 95.0%)
11. Nitric acid, HNO_3 (Merck, 65%)
12. Pluronic P123, PEO_{20}-PPO_{70}-PEO_{20}, MW = 5800 (Aldrich)
13. 2-propanol (Merck, 99.8%)
14. Tetrabutyl orthotitanate, TBOT (Aldrich, 97%)
15. Tetraethyl orthosilicate, TEOS (Fluka, 98%)
16. Tetrapropylammonium bromide, TPABr (Aldrich, 98%)
17. Tetrapropylammonium hydroxide, TPAOH (Merck, 40%)
18. Titanium isopropoxide, TIP (Fluka, 97%)
19. Vanadium (III) chloride, VCl_3 (Merck, 99.0%)

3.2.2 Chemicals for benzene hydroxylation

1. Acetonitrile, CH_3CN (Fisher Scientific, 99.9%)
2. Benzene, C_6H_6 (Carlo Erba, 99%)
3. Benzoquinone, $C_6H_4O_2$ (Merck, 99%)
4. Cycloheptanone, $C_7H_{12}O$ (Aldrich, 99%)

5. Hydrogen peroxide, H_2O_2 (Merck, 30%)

6. Hydroquinone, $C_6H_6O_2$ (Merck, 99.5%)

7. Phenol, C_6H_5OH (Merck, 99%)

8. Pyrocatechol, $C_6H_4O_2$ (Merck, 99%)

3.2.3 Chemicals for iodometric titration

1. Ammonium molybdate, $(NH_4)_6Mo_7O_{24}.4H_2O$ (Baker Analyzed, 81.5%)

2. Potassium iodate, KIO_3 (Ajax Finechem, 99.4%)

3. Potassium iodide, KI (Carlo Erba, 99%)

4. Sodium hydroxide, NaOH (Merck, 99%)

5. Sodium thiosulfate, $Na_2S_2O_3.5H_2O$ (Ajax Finechem, 99.5%)

6. Starch powder (Aldrich)

7. Sulfuric acid, H_2SO_4 (Merck, 95%)

3.3 Catalyst preparation

3.3.1 Microporous materials preparation

3.3.1.1 Silicalite-1 preparation

Silicalite-1 was prepared according to the method described by Yeong et al. [45] using tetraethylorthosilicate (TEOS) as Si source and tetrapropylammonium hydroxide (TPAOH) as structure directing agent. The molar composition of the synthesis solution was 1 TEOS : 0.35 TPAOH : 0.119 EtOH : 20.75 H_2O. In a procedure, 100 g of TPAOH was dissolved in 24 g of deionized water. After that, a mixture of 58 g of TEOS and 1.53 g of ethanol was added dropwise and the solution was stirred at room temperature for 24 h. The synthesis solution was transferred to Teflon-lined autoclave and heat at 175°C for 48 h. The resulting product was filtered, washed with deionized water until the pH of the suspension became 8, dried at 100°C overnight

and calcined at 550°C for 5 h. The procedure for the silicalite-1 preparation was illustrated in Scheme 3.2

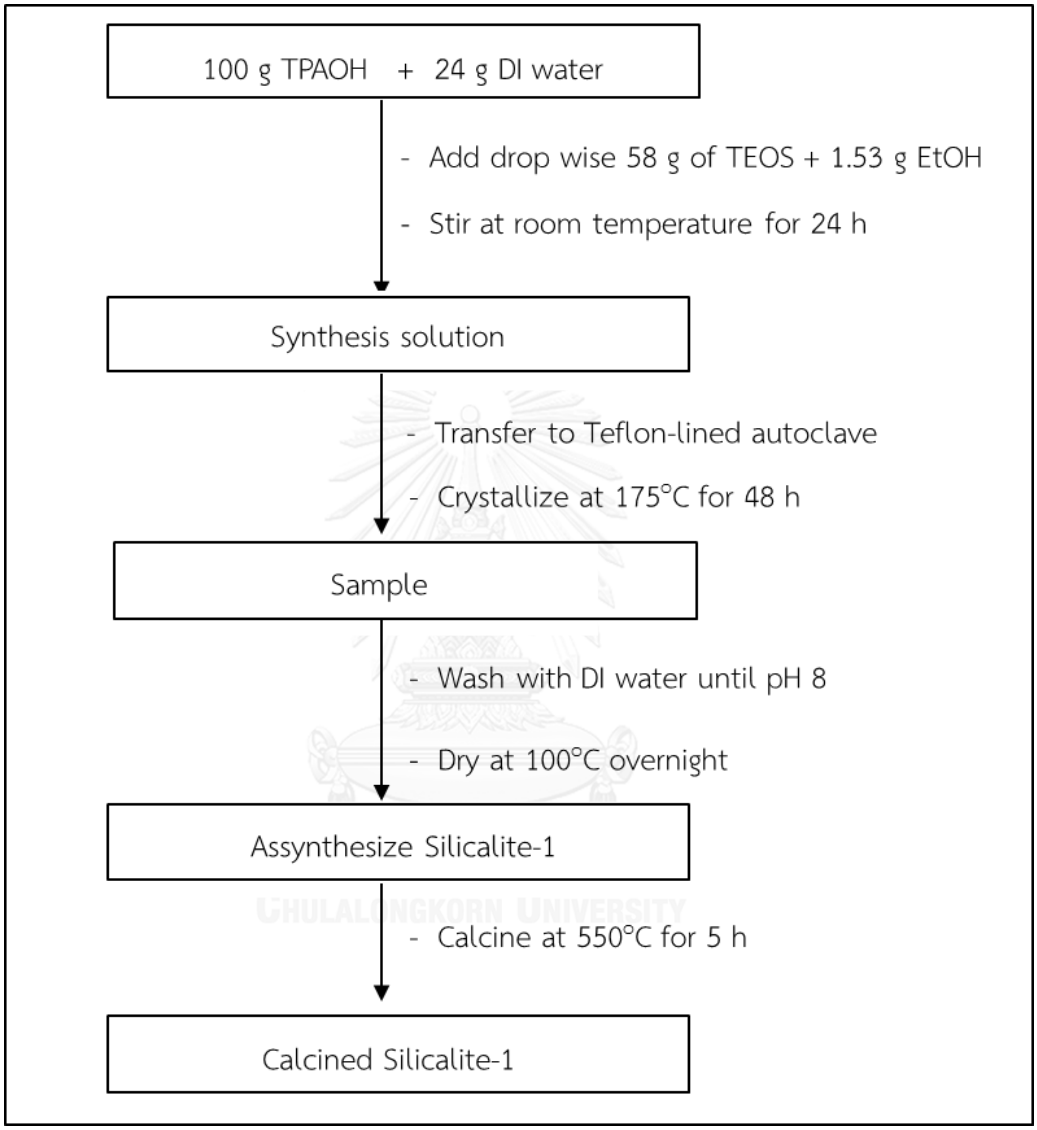

Scheme 3.2 Diagram of silicalite-1 preparation.

3.3.1.2 Titanium silicalite-1 preparation

TS-1 was synthesized following the method reported by Saksit [46]. In the preparation of TS-1 with Si/Ti = 40, using tetrapropylammonium hydroxide (TPAOH) and tetrapropylammonium bromide (TPABr) as template, tetraethyl orthosilicate (TEOS) and tetrabutyl orthotitanate (TBOT) as the Si and Ti source respectively. The molar composition of the gel was 1 TEOS : 0.025 TBOT : 0.18 TPAOH : 0.18 TPABr : 7.56 2-PrOH : 36.35 H_2O. Three aqueous solutions were prepared separately, Solution A was obtained by dissolving 37.82 g of TEOS in 66 g of 2-propanol. Solution B was prepared by dissolving 1.55 g of TBOT in 16.5 g of 2-propanol. Solution C was prepared by dissolving 8.89 g of TPABr in 59 g of deionized water and mixed with 53.16 g of TPAOH. In the ice bath and nitrogen atmosphere, 13.28 g of TPAOH was added drop wise into solution A with stirring for 1 h. After that, solution B was added drop wise into the mixture. After stirring for 1 h, solution C was added drop wise and the mixture was stirred for another 1 h. The resulting solution was heated at 80°C and the pH was adjusted to 11.7 with ammonium solution. The solution was stirred for 1 h in air. Thereafter, the resulting gel was transferred to Teflon-lined autoclave and heated at 170°C for 4 days with rotated at 60 rpm. The solid product was centrifuged at 5000 rpm for 15 min, washed with deionized water and dried at 100°C overnight. The dried product was calcined at 540°C for 10 h. The process for titanium silicalite-1 preparation was illustrated in Scheme 3.

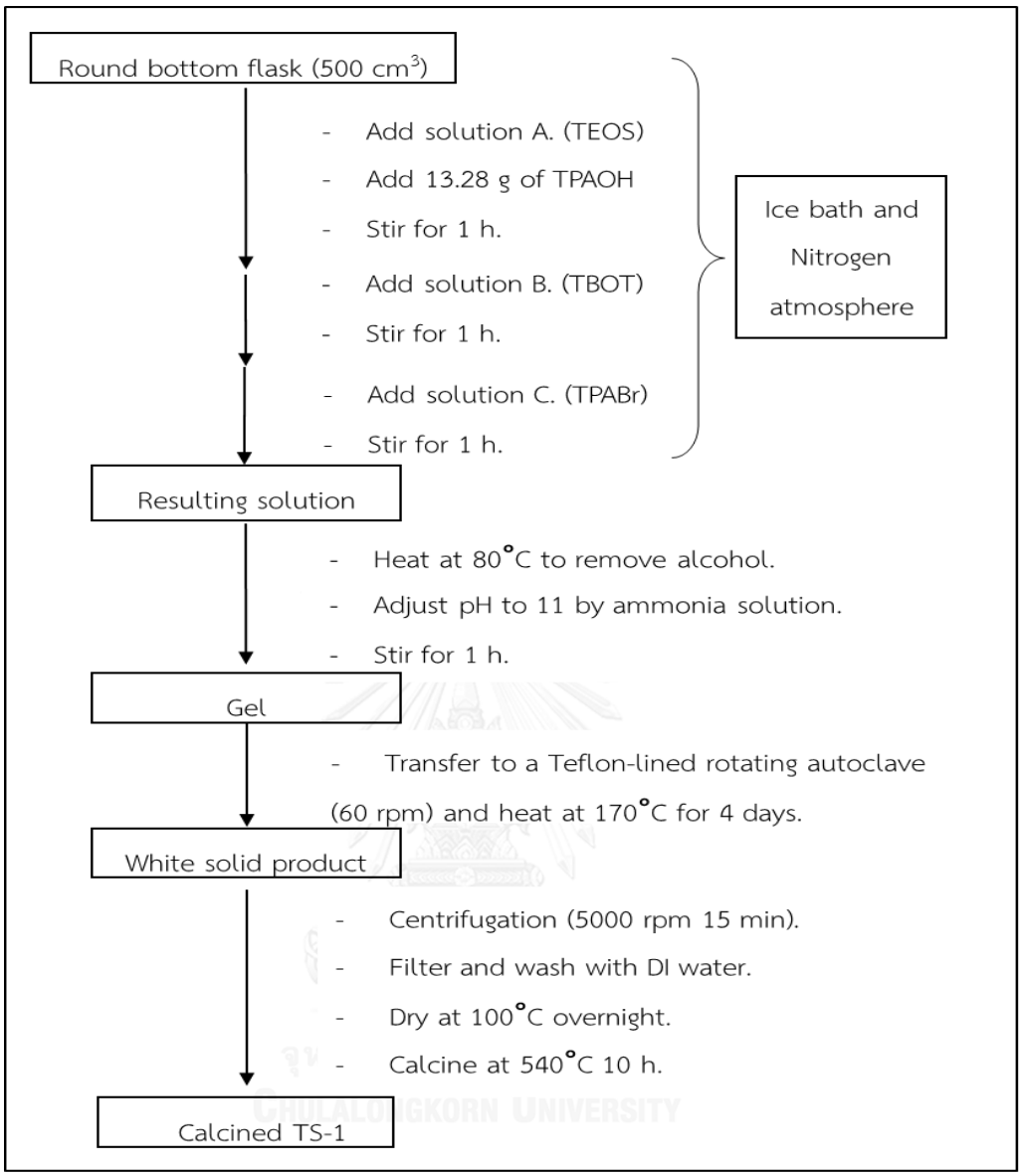

Scheme 3.3 Diagram of titanium silicalite-1 preparation.

3.3.1.3 Ti-MWW preparation

Ti-MWW was prepared by hydrothermal method using fumed silica and tetrabutyl orthotitanate (TBOT) as the Si and Ti sources, respectively [47]. The molar gel composition was SiO_2: $0.025TiO_2$: $0.67B_2O_3$: 1.4HMI: $19H_2O$. In a typical synthesis, 88.1 g of hexamethyleneimine was dissolved in 216 g of deionized water at room temperature. The solution was divided into two equal parts. One of these was added 5.4 g of tetrabutyl orthotitanate under vigorous stirring for 30 min. For another part of solution was added 52.5g of boric acid under vigorous stirring. Then, fumed silica was also divided into two equal parts which were added gradually to the solution containing titanium and boron, respectively. Both solutions were continuously stirred for 1 h. After that, the solutions were mixed together and stirred for 1.5 h. The gel was transferred in to a Teflon-lined autoclave. The temperature program for synthesis was started at 130°C and then 150°C each for 1 day and further at 170°C for 5 days with a stirring rate of 100 rpm. The product was filtered off, washed with deionized water until the pH of the suspension to 9, and dried at 50°C overnight. After that, the resulting product was refluxed with 6 M HNO_3 at 100°C for 20 h. Then, the product was filtered and dried at 50°C overnight. Final product was calcined at 530°C for 10 h to remove of any organic species. The process of Ti-MWW preparation was shown in Scheme 3.4.

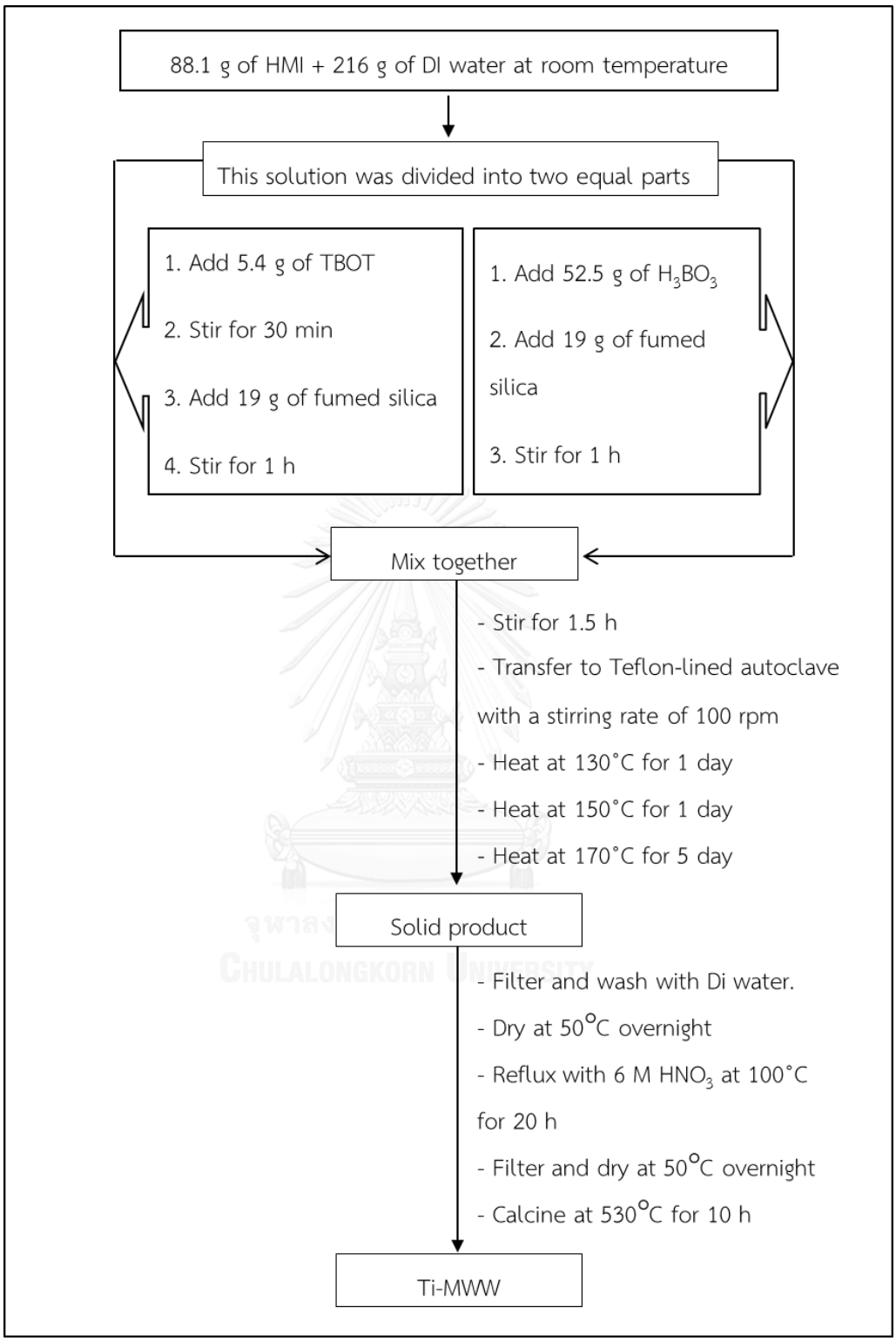

Scheme 3.4 Diagram of Ti-MWW preparation.

3.3.2 Mesoporous materials preparation

3.3.2.1 SBA-15 preparation

Pure SBA-15 was synthesized following the method described by Dongyuan et al. [48] using tetraethyl orthosilicate (TEOS) as a Si source and pluronic P123 triblock copolymer ($PEO_{20}PPO_{70}PEO_{20}$) as a structure directing agent. The molar gel composition of the solution was 1TEOS : 0.0169 P123 : 5.88 HCl : 192 H_2O . In the procedure, 8 g of Pluronic P123 was dissolved in 240 g of 2 M HCl with stirred at room temperature. After 60 min, 60 g of deionized water was added and stirred for 30 min. Thereafter, 17 g of TEOS was added drop wise and the solution was stirred for 60 min at room temperature. After that, the solution was aged at 40°C for 24 h. The resulting solution was transferred to Teflon-lined autoclave and crystallization at 100°C for 48 h. The solid product was filtered, washed with deionized water, dried at 60°C overnight and calcined at 550°C for 5 h. The procedure for preparing SBA-15 was shown in Scheme 3.5.

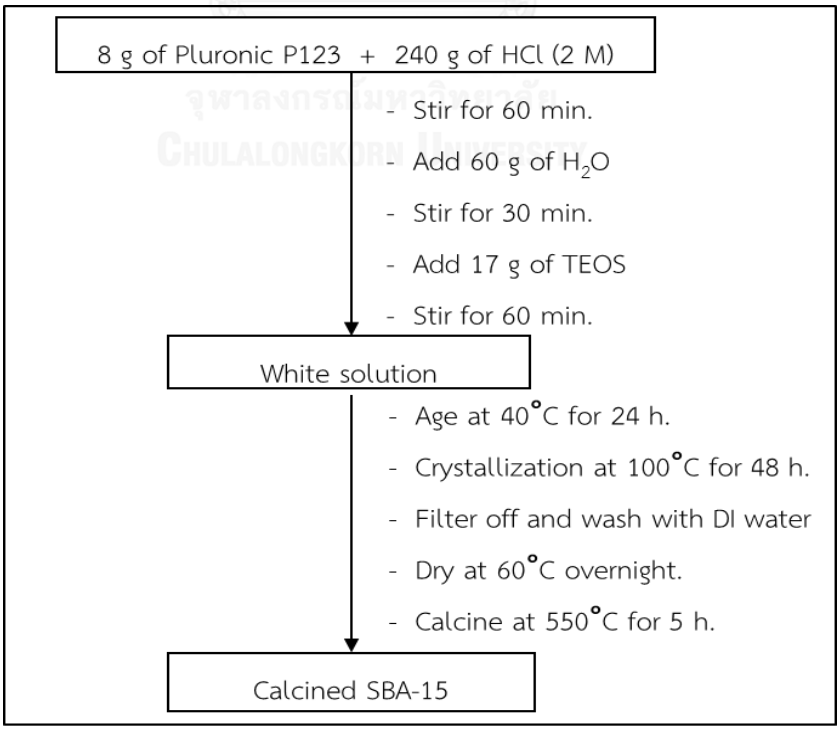

Scheme 3.5 Diagram of SBA-15 preparation.

3.3.2.2 Ti-SBA-15 preparation

Ti-SBA-15 was prepared by directly hydrothermal method reported by Han et al. [49] using pluronic P123 triblock copolymer ($PEO_{20}PPO_{70}PEO_{20}$) as a structure directing agent, tetraethyl orthosilicate (TEOS) and titanium isopropoxide as the Si and Ti sources, respectively. The molar gel composition of Ti-SBA-15 with Si/Ti=40 was 1 TEOS : 0.025 TIP : 0.0169 P123 : 5.88 HCl : 192 H_2O. In the procedure, 4 g of pluronic P123 was added to 120 g of 2 M HCl and 30 g of deionized water. The mixture was stirred to homogeneous at 35°C. After that, 8.5 g of TEOS was drop wise into the solution and stirred for 10 min. Then, 0.29 g of titanium isopropoxide was slowly added into the solution under vigorously stirred at 35°C for 20 h. The resulting solution was transferred to Teflon-lined autoclave and hydrothermally treated at 90°C for 24 h. The precipitated product was filtered, washed with deionized water, dried at 60°C for 24 h and calcined at 550°C for 4 h. The process of Ti-SBA-15 preparation was shown in Scheme 3.6.

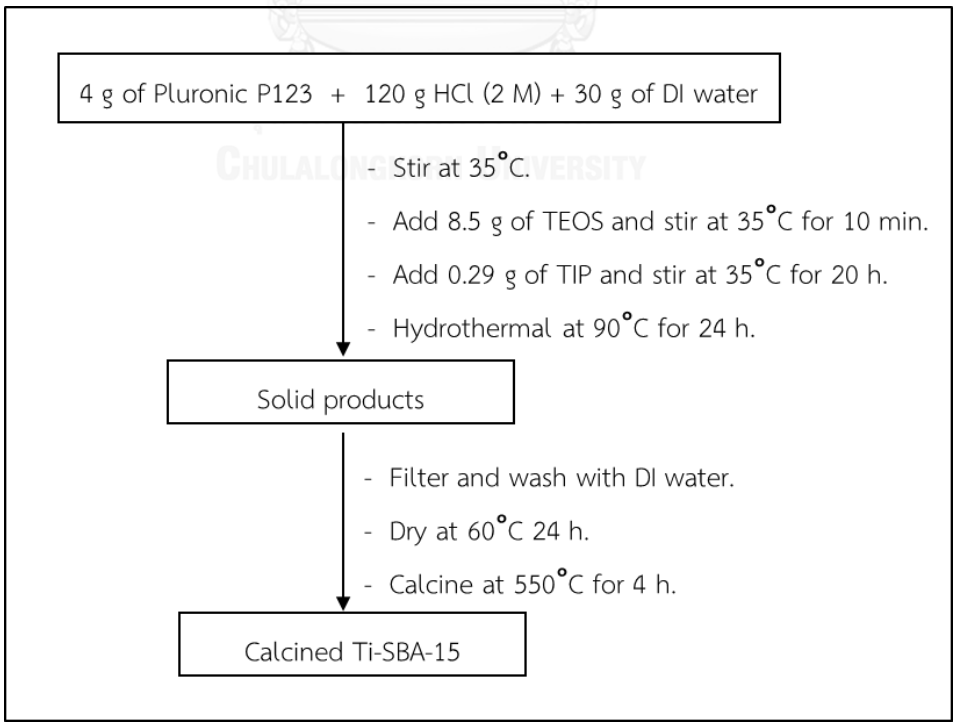

Scheme 3.6 Diagram of Ti-SBA-15 preparation.

3.3.2.3 Ti-MCA preparation

Ti-MCA was prepared by directly hydrothermal method which modified from Kubota's method using pluronic P123 triblock copolymer (PEO_{20}-PPO_{70}-PEO_{20}) as a structure directing agent, tetraethyl orthosilicate (TEOS) and titanium isopropoxide as the Si and Ti sources, respectively [34]. The molar gel composition of Ti-MCA with mole ratio of Si/Ti=40 was 1TEOS : 0.025 TIP : 0.018 P123 : 0.089 MPTMS : 2 HCl : 148 H_2O. In the procedure, 4 g of Pluronic P123 was added to 7.8 g of HCl and 30 g of deionized water. The mixture was stirred to homogeneous at room temperature for 1 h. After that, 8.5 g of TEOS and 0.69 g of MPTMS were added to the solution and stirred for 10 min. Then, 0.29 g of TIP was slowly added into the solution under vigorously stirred at 40°C for 24 h. The resulting solution was transferred to Teflon-lined autoclave and crystallized at 100°C for 48 h. The precipitated product was filtered, washed with deionized water, dried at 60°C for 24 h and calcined at 550°C for 4 h. The procedure for synthesizing the Ti-MCA was shown in Scheme 3.7.

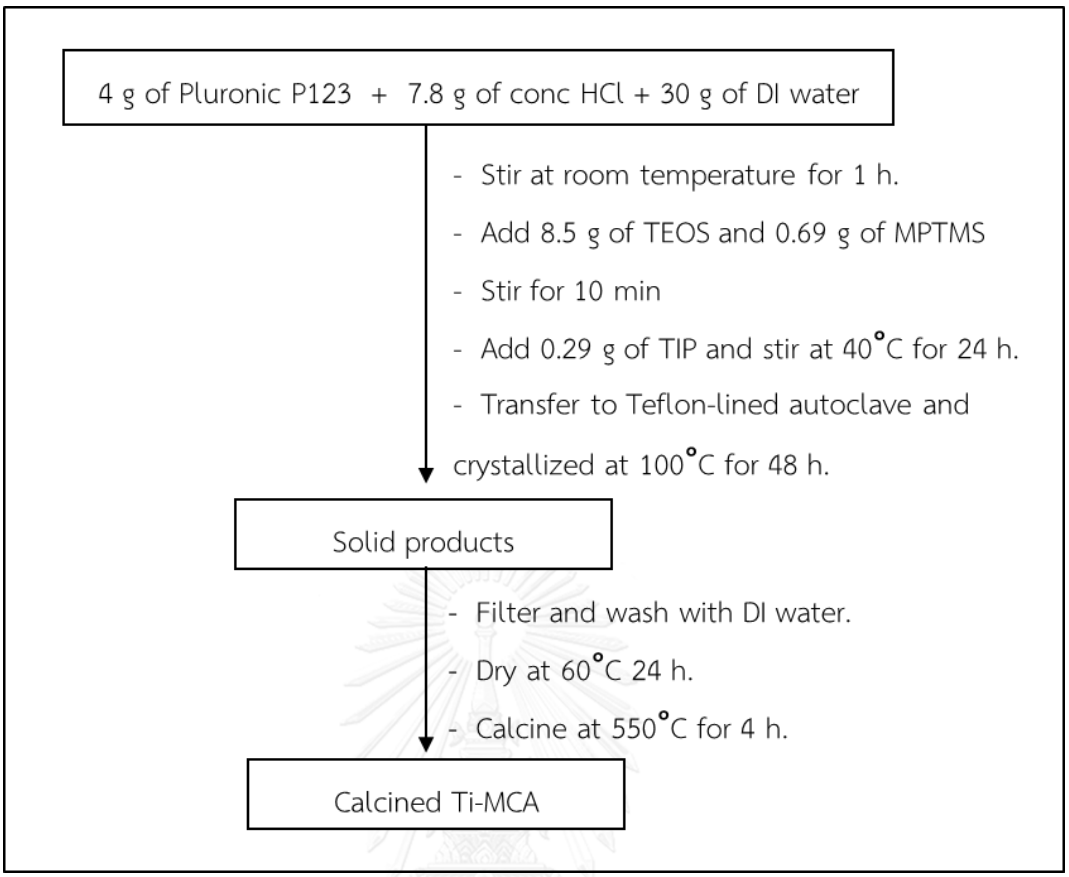

Scheme 3.7 Diagram of Ti-MCA preparation.

3.3.3 Bimetallic catalyst preparation

Second metals (Ce, Cu, Fe, V) supported on titanosilicate supports (TS-1, Ti-MWW, Ti-MCA, Ti-SBA-15) were prepared by wetness impregnation method from cerium (III) nitrate hexahydrate, copper (II) nitrate trihydrate, iron (III) nitrate nonahydrate and vanadium (III) chloride. The appropriate contents of metal was loaded at room temperature under stirring for 6 h. Afterwards, the mixture was heated at 100°C, dried at 50°C overnight and calcined at 400° for 4 h. The resulting products were denoted as M/TS-1, M/Ti-MWW, M/Ti-MCA and M/Ti-SBA-15 where M represented to the second metals. The procedure for preparing bimetallic catalyst was shown in Scheme 3.8.

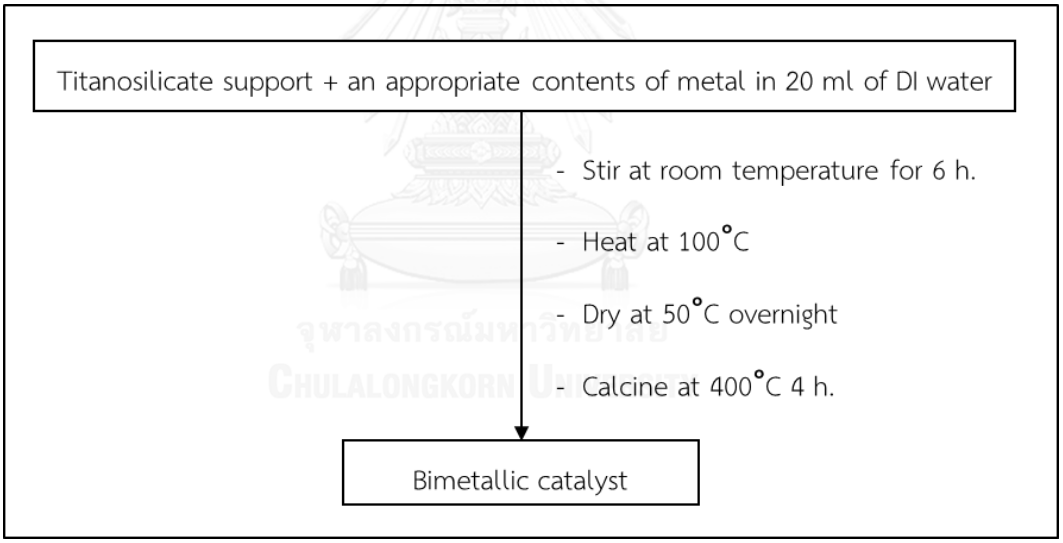

Scheme 3.8 Diagram of bimetallic catalyst preparation.

3.3.4 VO-propyl-NH_2-anchoring on Ti-MWW preparation

VO-propyl-NH_2-anchoring on Ti-MWW was prepared by method which modified from Jiang's method[50]. This method consisted of two parts.

3.3.4.1 Propyl-NH_2-anchoring on Ti-MWW

1 g of calcined Ti-MWW was added to 200 mL of toluene. After stirred for 30 min, 5 g of 3-aminopropyltrimethoxysilane was added. The mixture was refluxed at 110°C overnight. Then, the product was filtered, washed and dried under vacuum.

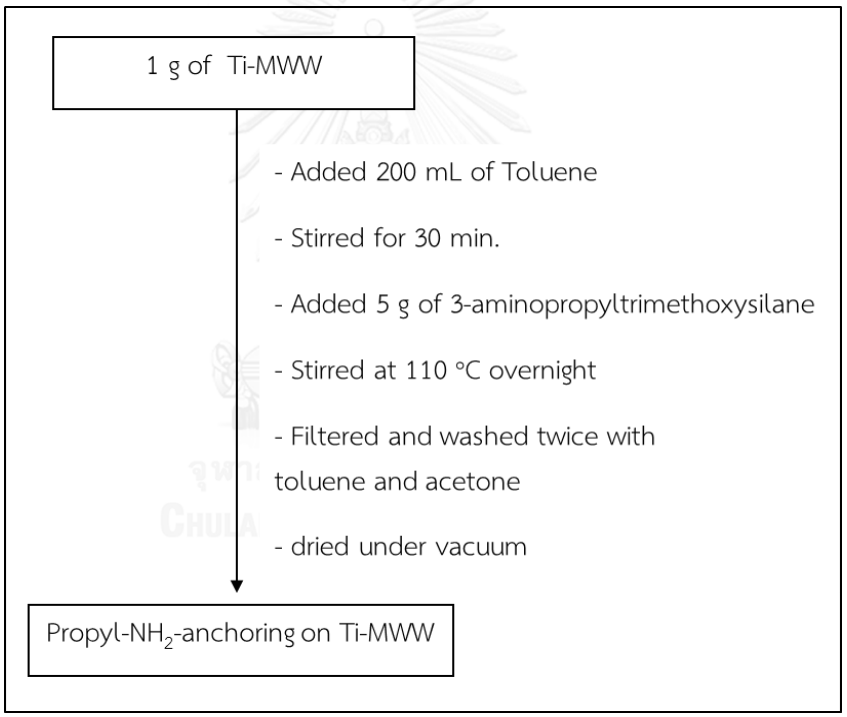

Scheme 3.9 Diagram of Propyl-NH_2-anchoring on Ti-MWW preparation.

3.3.4.2 (VO)-propyl-NH_2-anchoring on Ti-MWW

The appropriate contents of $VOSO_4$ in 20 mL of DI water was loaded on Propyl-NH_2-anchoring on Ti-MWW and stirred for 1 h. After that, the solid products was filtered and washed with DI water. Then, the sample was dried under vacuum.

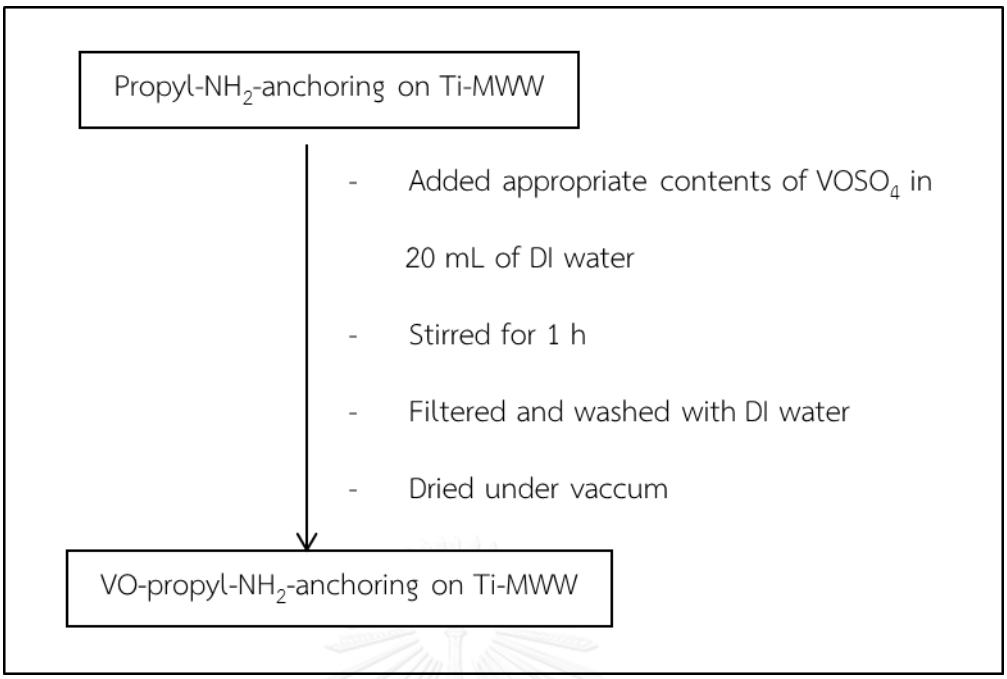

Scheme 3.10 Diagram of VO-Propyl-NH_2-anchoring on Ti-MWW preparation.

3.4 Procedure in benzene hydroxylation reaction

The catalytic activity was investigated in benzene hydroxylation reaction using H_2O_2 as an oxidant. The procedure was carried out in a three-necked round bottomed flask connected with a reflux condenser. A typical reaction was carried out as the follows: catalyst, 1.75 g of benzene (22.4 mmol) and 5.66 g of acetonitrile were added into the flask. After heating the mixture to set temperature, 30 wt.% of hydrogen peroxide was added dropwise. Then, the reaction mixtures were further stirred. After reaction, the catalysts were separated from the reaction mixture by centrifugation. The reaction mixture was analyzed by gas chromatography.

3.5 Iodometric titration process

3.5.1 Standardization of Sodium Thiosulfate

20 mL of potassium iodate solution (0.1 N) was pipetted into Erlenmeyer flask which containing 100 mL of H_2O. After that, 20 mL of potassium iodide solution (0.1 N) was added and mixed well following the adding of 25 mL of acid mixture, stoppered the flask, and waited for five minutes. Then, titrated with the sodium thiosulfate solution until the brown triiodide color is nearly dispersed to a pale straw color. 1 mL of Starch solution was added and then titrated until the solution changes sharply from blue to colorless. The titration volume was recorded, calculated the normality of the sodium thiosulfate solution and repeated procedure two additional times.

3.5.2 Determination of Hydrogen Peroxide

3 g of sample was loaded into Erlenmeyer flask. After that, 200 mL of water, 20 mL of potassium iodide solution, and 25 mL of the acid mixture were added. The resulting solution was mixed, stoppered, and waited for five minutes. Then, the solution was titrated with sodium thiosulfate solution (0.1N) until the brown color of triiodide was reduced to a light straw color. The starch solution was added into the solution and then continued titrating until the blue color of the solution changed to colorless. The titration procedure was repeated without the addition of sample and recorded as blank titration volume.

3.6 Parameter affecting benzene hydroxylation reaction

3.6.1 Effect of transition metal

The transition metals in this study were cerium, copper, iron and vanadium.

3.6.2 Effect of benzene to hydrogen peroxide mole ratio

The effect of benzene to hydrogen peroxide mole ratio was investigated at the value of 1:1-1:13.

3.6.3 Effect of catalytic amount

The amount of catalyst was varied from 0, 1.4, 2.9, 4.3, 5.7, and 8.6 wt.% based on weight of benzene.

3.6.4 Effect of reaction time

The reaction time was varied in range of 0.5-5 h.

3.6.5 Effect of reaction temperature

The reaction temperature was varied in range of 50-70°C.

3.6.6 Effect of vanadium content

The content of vanadium was investigated at the value of 5, 10, 15 and 20 wt.%.

3.6.7 Effect of Si/Ti mole ratio

The mole ratio of Si/Ti was studied in the range of 20-100.

3.6.8 Effect of solvent

The solvents in this study were acetonitrile, methanol, acetone and water.

3.6.9 Activity of reused catalyst

The used catalyst was washed with acetone and dried at 60°C before reused in next batch.

CHAPTER IV
RESULTS AND DISCUSSIONS

4.1 The physico-chemical properties of bimetallic titaniumsilicalite-1

4.1.1 Effect of second metal (M/TS-1)

4.1.1.1 XRD results

Figure 4.1(a) showed the small-angle XRD patterns of silicalite-1 and metal supported on TS-1. All products exhibited the pattern of diffraction peaks that can be assigned to MFI structure [45]. Moreover, XRD spectra of TS-1 showed a little bit lower intensity than silicalite-1. The incorporation of titanium atom in the framework of TS-1 caused a decrease of the crystallinity that affected on the intensity of diffraction peak. In addition, XRD spectra of TS-1 did not show the characteristic peak of the anatase phase at $2\theta \approx 25.3°$, 37.8° and 48.0° [51]. This was resulted from the absence or trace amount of the anatase phase. After impregnation, the XRD results suggested that the MFI structure of TS-1 was still remained during the preparation of modified metal catalysts. Furthermore, the intensity of the XRD pattern of bimetallic catalysts was found to be reduced, resulting in decrease of crystalinity. Furthermore, the wide-angle XRD patterns of the catalysts are shown in Figure 4.1(b). It should be noticed that the characteristic diffraction peaks of CeO_2 structure at 2θ = 28.5, 47.5 and 56.4° were observed. It means that crystallites and amorphous phase of CeO_2 are present in Ce/TS-1 sample [52]. Additionally, the XRD patterns of Cu/TS-1 exhibited the diffraction peaks at 2θ = 35.5, 38.7 and 48.5° that corresponding to the characteristic peak of CuO [53]. Moreover, the diffraction peaks at 2θ = 33.1, 35.6, 49.4, 54.0, 62.4 and 63.9° represented the presence of Fe_2O_3 in Fe/TS-1 sample [54], while the characteristic diffraction peaks of V_2O_5 at 2θ = 20.27, 26.21 and 31.05° were well defined in the diffractogram of V/TS-1 sample [55]. These

results are in a good agreement with the results from DR-UV spectroscopy and TEM micrographs.

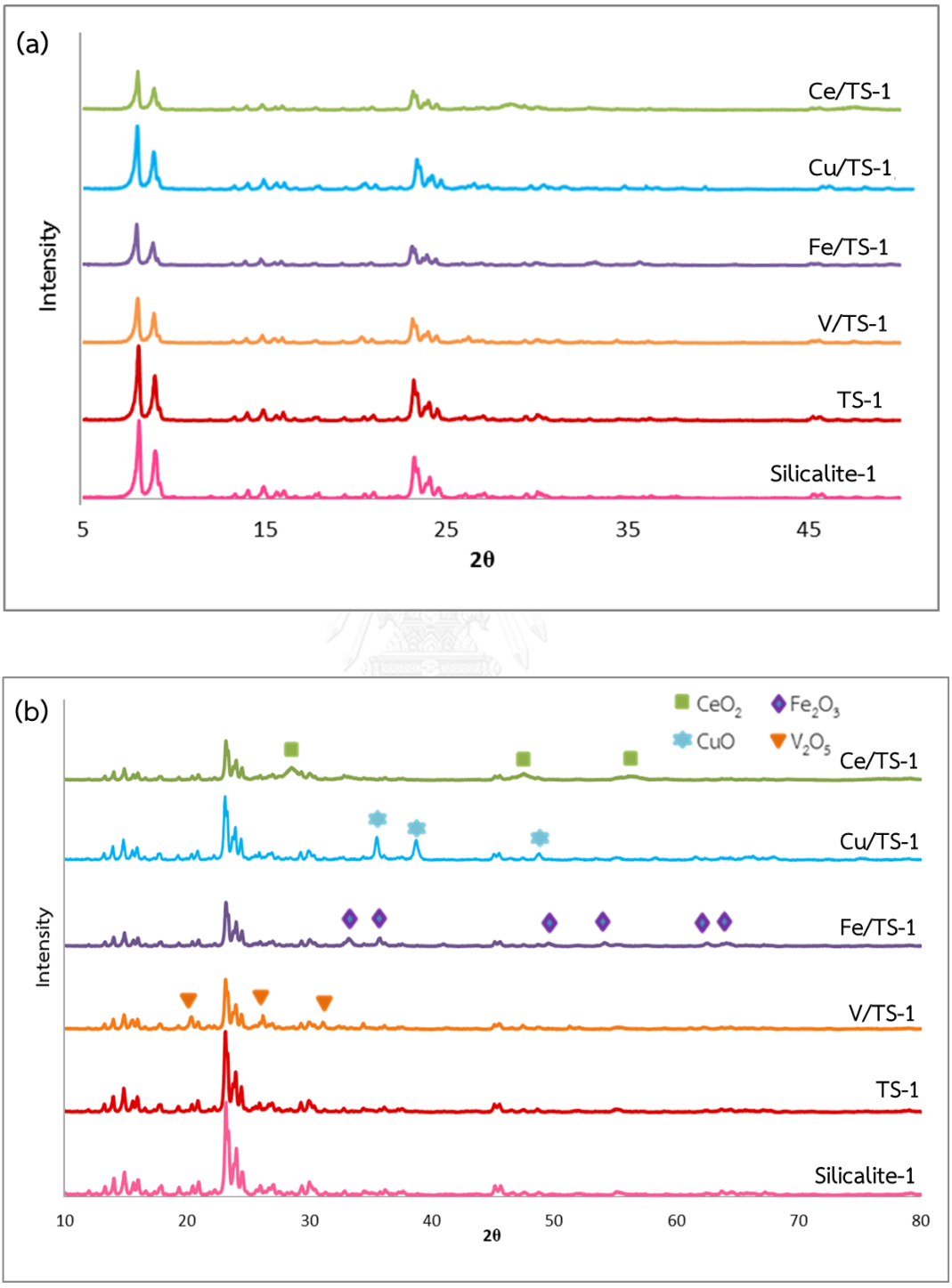

Figure 4.1 X-ray powder diffraction patterns of bimetallic titaniumsilicalite-1 (M/TS-1) in the range of (a) small-angle and (b) wide-angle.

4.1.1.2 DR-UV results

DR-UV spectra of TS-1 showed the absorption peaks at 210 and 320 nm. The strong peak at 210 nm can be ascribed to a charge transfer from oxygen to tetracoordinated titanium and the peak at 320 nm was attributed to anatase phase [56], as shown in Figure 4.2. The major amount of titanium atom located at the tetrahedrally coordinating position in the framework of TS-1. After insertion of second metal, an intense absorption peak at about 210 nm that attributed to the tetrahedrally coordinated titanium was detected in all the samples. For Ce/TS-1 catalyst, a broad absorption peaks at 290 and 340 nm were found. These peaks can be attributed to the bond $O^{2-} \rightarrow Ce^{4+}$ of CeO_2 and small CeO_2 crystallites, respectively [57]. It might be indicate that the Ce on the TS-1 support existed as CeO_2 particle, which was consistent with XRD results. In addition, the spectra of Cu/TS-1 sample displayed the absorption band at 210-270 nm. This result indicated to the Cu ions that occupied isolated sites. Moreover, the band over 350 nm indicated the formation of Cu clusters to bulk CuO form [58]. In the case of Fe/TS-1, the shoulder peak which assigned to octahedral Fe^{3+} occurs at 280 nm. Moreover, the absorption peak at 380 nm can be ascribed to small clusters or microaggregates of Fe_2O_3 particles and the intense peaks at 420, 500 and 540 nm related to the aggregated Fe_2O_3 clusters [59, 60]. Thus, aggregated iron oxide clusters were mainly observed for Fe/TS-1 sample. Furthermore, seven absorption peaks at 210, 280, 340, 380, 420, 460 and 500 nm appear on V/TS-1. The peaks at 210 and 280 nm can be attributed to the isolated tetrahedral V^{5+} species [61], while two absorption peaks at 340 and 380 nm indicated the presence of low oligomeric tetrahedral coordinated V^{5+} species [61, 62]. Moreover, the absorption peak at 420 nm corresponding to the octahedral V^{5+} species [63], as well as the absorption region at 450-550 nm associated to bulk V_2O_5 [64]. From the results, VO_x structure can be present in the form of tetrahedral VO_4 species, low polymeric and crystalline V_2O_5.

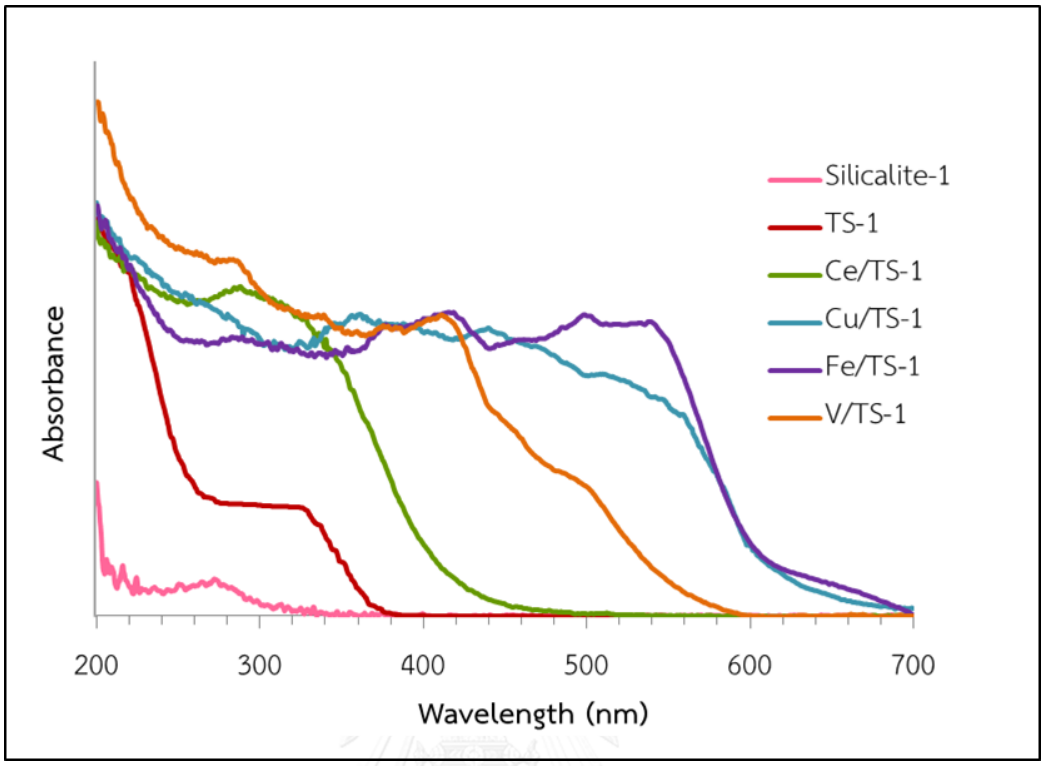

Figure 4.2 DR-UV spectra of M/TS-1.

4.1.1.3 Sorption properties

The nitrogen adsorption/desorption isotherms of silicalite-1 and metal supported on TS-1 catalyst were shown in Figure 4.3(a). It is clear that the nitrogen adsorption/desorption isotherms of silicalite-1 and TS-1 showed the typical type I as defined by IUPAC for microporous materials and a placid hysteresis loop with a small closed area [45]. This hysteresis loop resembles the H4 type in the IUPAC classification, which indicates to slit-like micropore. After the impregnation of second metal, the isotherms of M/TS-1 catalysts retained their shape, which could be an indication for maintenance of the microscopic order of the parent material. The pore size distribution of all products was shown in Fig. 4.3(b). The samples exhibited pore size distribution centered mostly at 0.7 nm. However, a small portion of the pores were located near 1.0 and 0.9 nm for silicalite-1 and M/TS-1, respectively. The physical properties of the samples were summarized in Table 4.1. From the result, the surface area and pore volume were sharply decreased after the addition of second metal. This result indicated that a portion of the metal oxide particles have entered into the pores leading to partial blockage by some agglomerates.

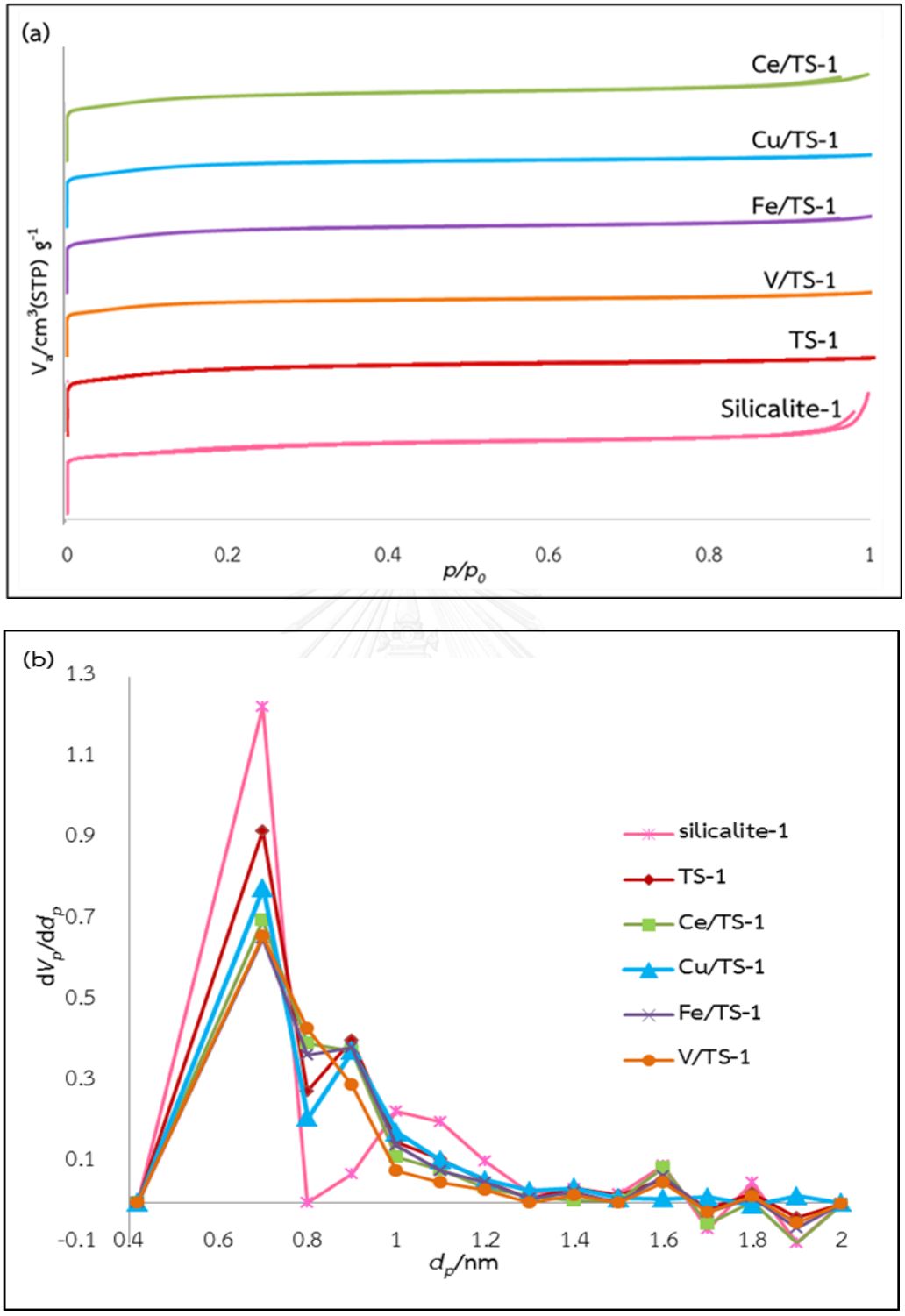

Figure 4.3 (a) N_2 adsorption/desorption isotherms and (b) pore size distributions of bimetallic TS-1.

Table 4.1 Textural properties of the metal containing TS-1 (M/TS-1).

Sample	Si/Ti	N_2 Adsorption/desorption		
		Specific surface area (BET)[a] ($m^2 g^{-1}$)	Pore volume ($cm^3 g^{-1}$)[b]	Pore diameter (nm)[b]
Silicalite-1	-	414	0.1769	0.7
TS-1	40	446	0.2072	0.7
Ce/TS-1[c]	40	403	0.1784	0.7
Cu/TS-1[c]	40	391	0.1821	0.7
Fe/TS-1[c]	40	390	0.1775	0.7
V/TS-1[c]	40	365	0.1614	0.7

[a]BET was calculated by $S_{BET} = S_{total}/a$; S_{BET} = the total surface area, S_{total} = the specific surface area, a = mass of the adsorbent

$S_{total} = (V_m N s)/V$; s = the adsorption cross section of the adsorbing species, N = Avogadro's number, V = the molar volume of the adsorbat gas, V_m= units of volume which are also the units of the molar volume of the adsorbate gas.

[b]reported by MP plot

[c]10wt.% metal supported on TS-1

4.1.1.4 SEM images

The morphology of synthesized silicalite-1, TS-1 and bimetallic TS-1 were further evident from the SEM observation. Figure 4.4(a) represented the SEM images of silicalite-1, which consisted of cubic-liked particles with an average diameter of 94 nm. In the part of TS-1, the crystal shape consisted of cubic-liked and hexagonal prismatic particles. The particle size increased to 187 × 187 nm and 190 × 250 nm for TS-1 and bimetallic TS-1 cubic-liked and hexagonal prismatic particles, respectively. After metal impregnation, the particle size was slightly changed. Bimetallic TS-1 particles were smaller than TS-1. The particle size of Ce/TS-1, Cu/TS-1, Fe/TS-1 and V/TS-1 were 187 nm, 184 nm, 156 nm and 125 nm, respectively.

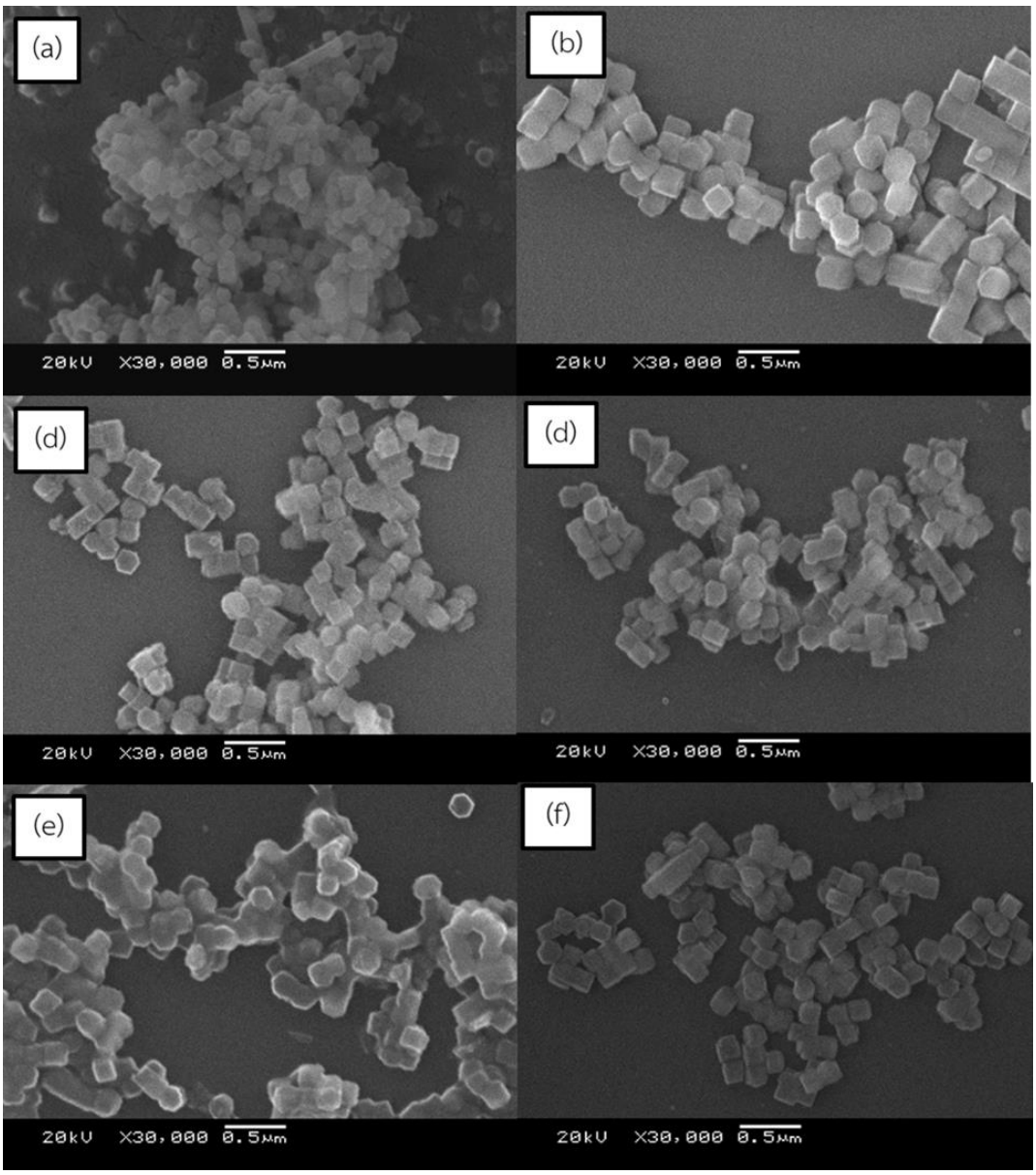

Figure 4.4 The SEM images of (a) silicalite-1, (b) TS-1, (c) Ce/TS-1, (d) Cu/TS-1, (e) Fe/TS-1 and (f) V/TS-1.

4.1.1.5 TEM images

TEM images of bimetallic TS-1 catalysts were depicted in Figure 4.5. The morphology of pure TS-1 comprised of the crystal with mean dimension around 193 × 246 nm and having well defined edges (Fig.4.5(a)). On the surface of Ce/TS-1, Cu/TS-1 and Fe/TS-1, metal particles consisted of large and irregular aggregated particle with size in the range of 30-125 nm, 137-158 nm and 63–250 nm for Ce/TS-1, Cu/TS-1 and Fe/TS-1, respectively. These results were consistent with the XRD results, which exhibited the high intense characteristic peak of CeO_2, CuO and Fe_2O_3. Therefore, the TEM images could be confirmed that the bulk CeO_2, CuO and Fe_2O_3 particles could form on the external surface of Ce/TS-1, Cu/TS-1 and Fe/TS-1, respectively. Additionally, the randomly spherical particles of V_2O_5 could be observed on the surface of V/TS-1 (Fig. 4.5(e)) with mean dimensions around 12.5 × 25 nm.

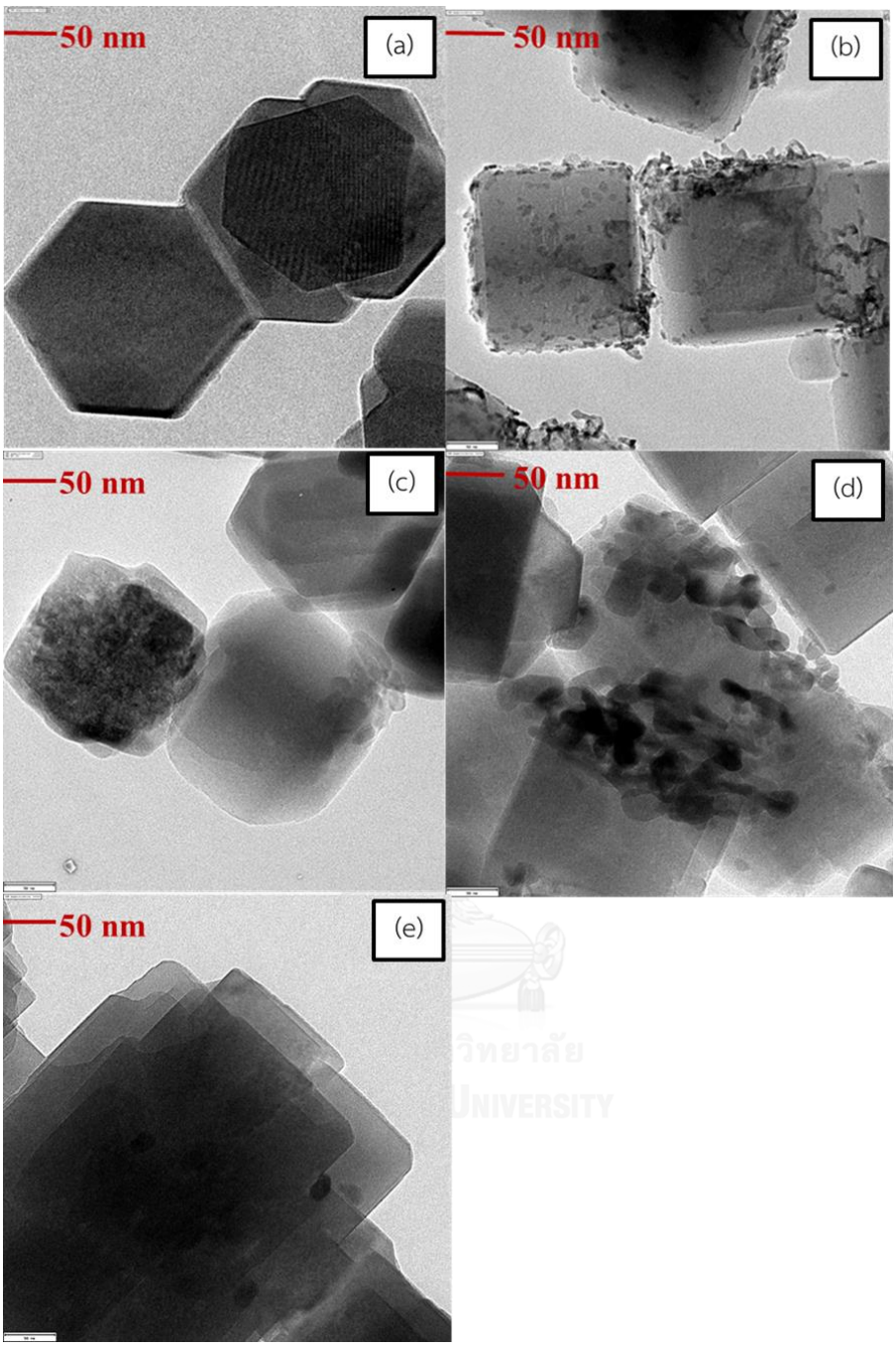

Figure 4.5 TEM images of (a) TS-1, (b) Ce/TS-1, (c) Cu/TS-1, (d) Fe/TS-1 and (f) V/TS-1.

4.1.2. Effect of vanadium content

4.1.2.1 XRD results

Figure 4.6 showed the wide-angle X-ray diffraction patterns of V/TS-1 with different V-contents. All samples exhibited the diffraction patterns similar to parent TS-1 which indicated the MFI structure. Furthermore, it was obviously observed that the peak intensity of MFI structure gradually decreased with increasing V-content from 5 to 20 wt.%. A significant decrease in peak intensity was caused by the reduction of the regularity of pore structure which was attributed to the addition of V species and the formation of bulk V_2O_5. At the 5 wt.% V/TS-1, the XRD spectrum was similar to parent TS-1 and no observed characteristic reflections of V_2O_5 phase. This resulted from the formation of the high dispersed V species on the surface of TS-1. With the increasing of V loading, the characteristic peaks of V_2O_5 were observed at 2θ = 20.27, 26.21 and 31.05° [55] and their intensity grew with the V-content. At 20 wt.% of V loading, the characteristic peaks of V_2O_5 indicated the highest intensity. These results revealed a decreasing V dispersion on the surface of TS-1 with increasing V loading, which can be confirmed by TEM results.

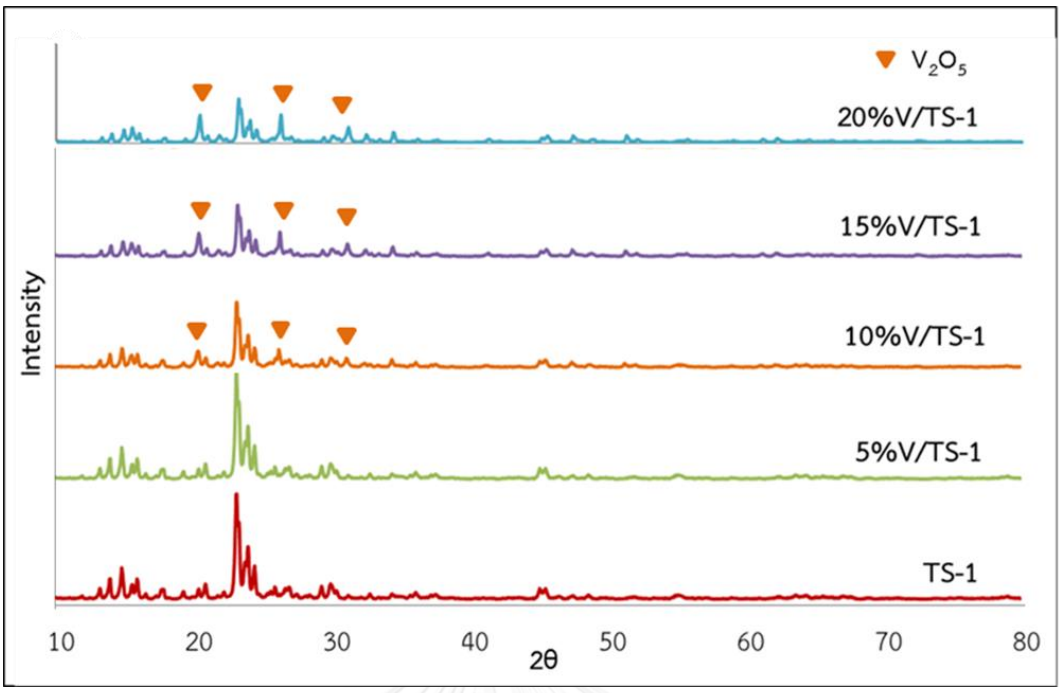

Figure 4.6 X-ray powder diffraction patterns of V/TS-1 with different V-contents.

4.1.2.2 DR-UV results

The DR-UV spectra of V/TS-1 with different V-contents were shown in Figure 4.7. For all the V/TS-1 samples, the DR-UV spectra displayed the absorption peak at about 210 nm which was assigned to tetrahedrally coordinated titanium. At low V loading (5%V/TS-1), the profile of sample exhibited the characteristic peak at around 280 and 340 nm, which can be ascribed to the isolated tetrahedral V^{5+} of VO_4 species and the low oligomeric tetrahedral coordinated V^{5+} species, respectively [61, 62]. Furthermore, a weak shoulder bands at about 420, 460 and 500 nm that related to the octahedral V^{5+} species and bulk V_2O_5 [63, 64]. This result indicated that the vanadium species were mainly presented in the form of isolated tetrahedral and low oligomeric tetrahedral V^{5+} for sample with low V-content. As the vanadium content was up to 10 wt.%, one additional absorption band approximately at 380 nm was observed. This band can be ascribed to low oligomeric tetrahedral coordinated V^{5+} species. Moreover, the intensity of the absorption peaks at around 380, 420, 460 and

500 nm increased significantly when the amount of V loading increased from 5 wt.% to 20 wt.%. That corresponded to the results of XRD. At the high amount of V loading (15 and 20 wt.%), the absorption peaks at 460 and 500 nm became broader and their intensities increased, which indicated that more bulk V_2O_5 was obtained. At the same time, the intensity of the band which assigned to tetrahedral VO_4 decreased. These results reveal that the aggregation of isolated tetrahedral VO_4 species occurred to form bulk V_2O_5 with increasing V-content [65]. Therefore, the structures of vanadium species in the synthesized catalysts are strongly influenced by the vanadium concentration.

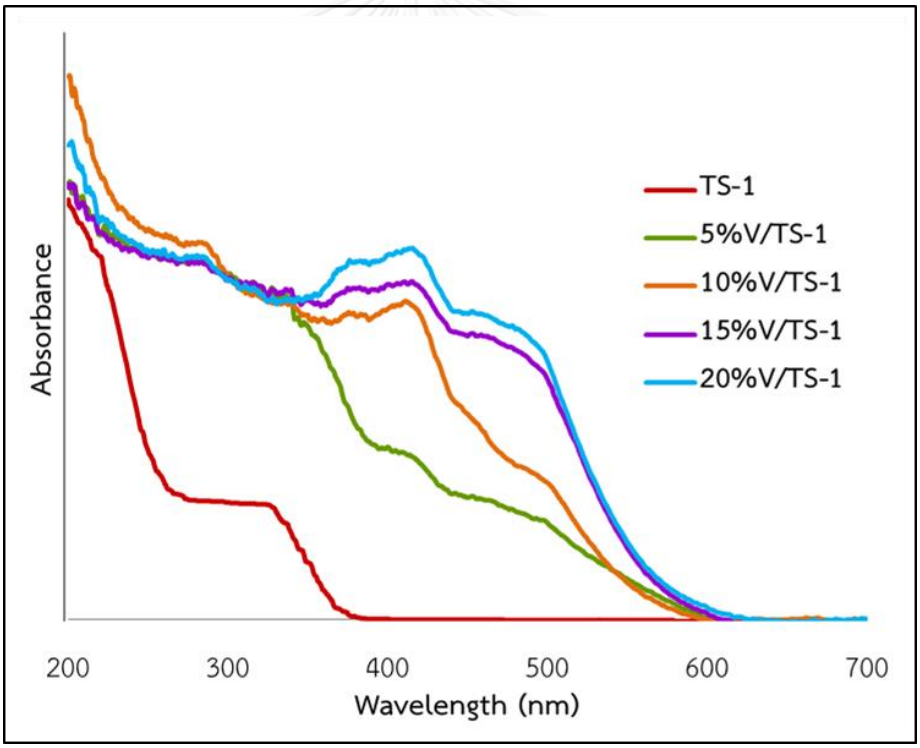

Figure 4.7 DR-UV spectra of V/TS-1 with different V-contents.

4.1.2.3 Sorption properties

Figure 4.8 illustrated the nitrogen adsorption/desorption isotherms and pore size distributions of V/TS-1 with various V-contents (0-20 wt.%). All the samples exhibited nitrogen adsorption/desorption isotherms type I with a H4 hysteresis loop, which is the characteristic of microporous material according to the IUPAC classification. Moreover, the pore sized distributions of samples exhibited pore diameter centered mostly at 0.7 nm with a small portion of pore at 0.9 nm. The textural properties of the samples are summarized in Table 4.2. With the increasing of the V-content from 0 to 20 wt.%, the surface area of the catalyst was decreased from 446 to 295 m^2g^{-1}, accompanied with the decreasing of the pore volume from 0.2072 to 0.1336 cm^3g^{-1}. This result suggested that the vanadia species was located inside the pores that caused a decrease in nitrogen adsorption capacity, reflecting a reduction in surface area and pore volume. Thus, the amounts of nitrogen up take in the samples depending on the content of vanadium. In addition, the unchangeable pore diameter with larger decrease in the pore volume and surface area was observed for V/TS-1 with high V-content. This explained that the partial pores were blocked by the vanadium oxide species as Tsoncheva et al. described [66]. These nitrogen adsorption data were in well agreement with the XRD and TEM results.

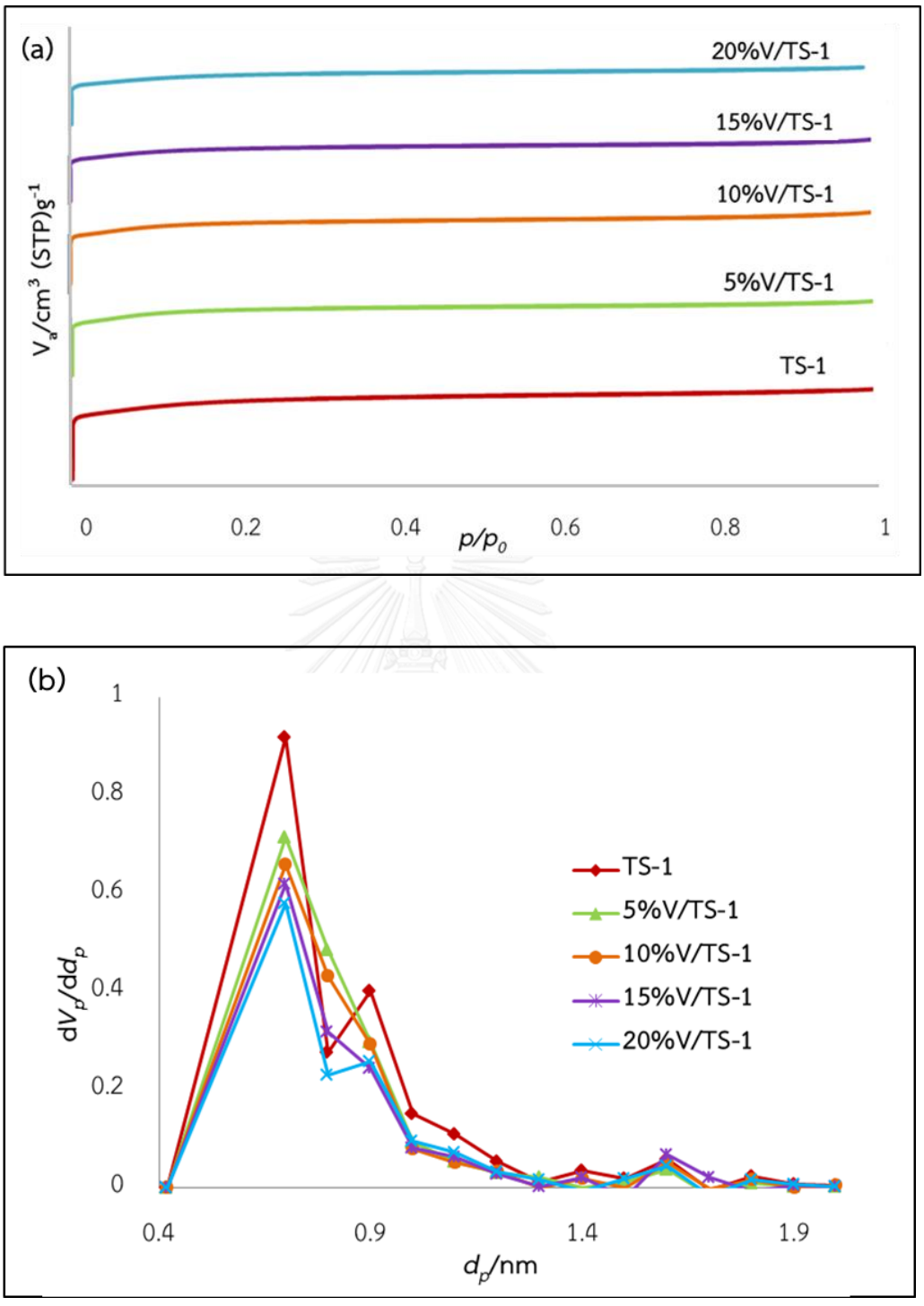

Figure 4.8 (a) N_2 adsorption/desorption isotherms and (b) pore size distributions of V/TS-1 with different V-contents.

Table 4.2 Surface properties of V/TS-1 with different V-content.

Sample	Metal content (wt.%)	N_2 Adsorption/desorption		
		Specific surface area (BET)[a] ($m^2 g^{-1}$)	Pore volume[b] ($cm^3 g^{-1}$)	Pore diameter[b] (nm)
TS-1[c]	-	446	0.2072	0.7
V/TS-1[c]	5	387	0.1734	0.7
	10	365	0.1614	0.7
	15	317	0.1414	0.7
	20	295	0.1336	0.7

[a]BET was calculated by $S_{BET} = S_{total}/a$; S_{BET} = the total surface area, S_{total} = the specific surface area, a = mass of the adsorbent

$S_{total} = (V_m Ns)/V$; V_m = units of volume which are also the units of the molar volume of the adsorbate gas, N = Avogadro's number, s = the adsorption cros section of the adsorbing species, V = the molar volume of the adsorbat gas.

[b]reported by MP plot

[c]Si/Ti =40

4.1.2.4 SEM images

SEM micrographs of the bimetallic TS-1 with different V-content are shown in Figure 4.9. After vanadium addition, the crystal shape of V/TS-1 remained the same as pure TS-1 while the particle sizes are slightly decreased. Furthermore, the average particles size of all impregnated samples was not changed as the increased V-content. The average particle sizes of all samples were 125 nm and 187 nm for cubic-liked and hexagonal prismatic particles, respectively.

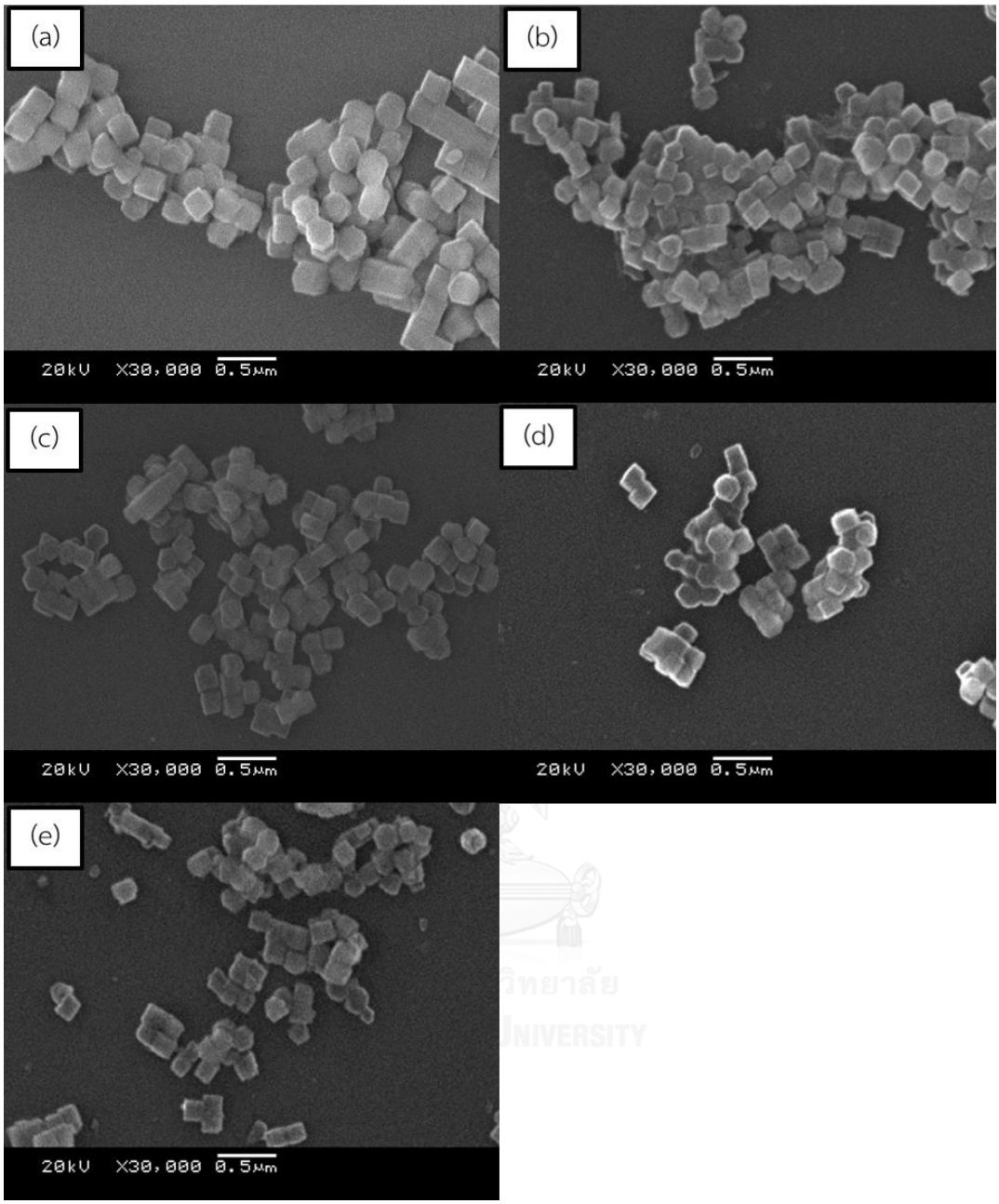

Figure 4.9 The SEM images of V/TS-1 with different V-content; (a) TS-1, (b) 5wt.% V/TS-1, (c) 10wt.% V/TS-1, (d) 15wt.% V/TS-1 and (e) 20wt.% V/TS-1.

4.1.2.5 TEM images

Comparison of the V distribution over the various V content, TEM micrographs of V/TS-1 with various amount of V loading were presented in Figure 4.10. The synthesized V/TS-1 with 5, 15 and 20 wt.% of V exhibited the particles with mean dimensions around 183 × 183 nm while the particle size of 10 wt.% V/TS-1 cannot determine due to the aggregation of particles. Furthermore, the TEM images of 5 wt.% (Fig. 4.10(a)) and 10 wt.% (Fig. 4.10(b)) V/TS-1, vanadium showed the pleasing dispersion on the TS-1 surface with small metallic particles in sizes about 8 × 8 nm and 12.5 × 25 nm, respectively. As the V-content increased to 15 and 20 wt.%, the TEM images presented the agglomeration of V metallic particles in irregular form with size in the range 60-170 nm and 133-317 nm for 15 and 20 wt.% V/TS-1, respectively.

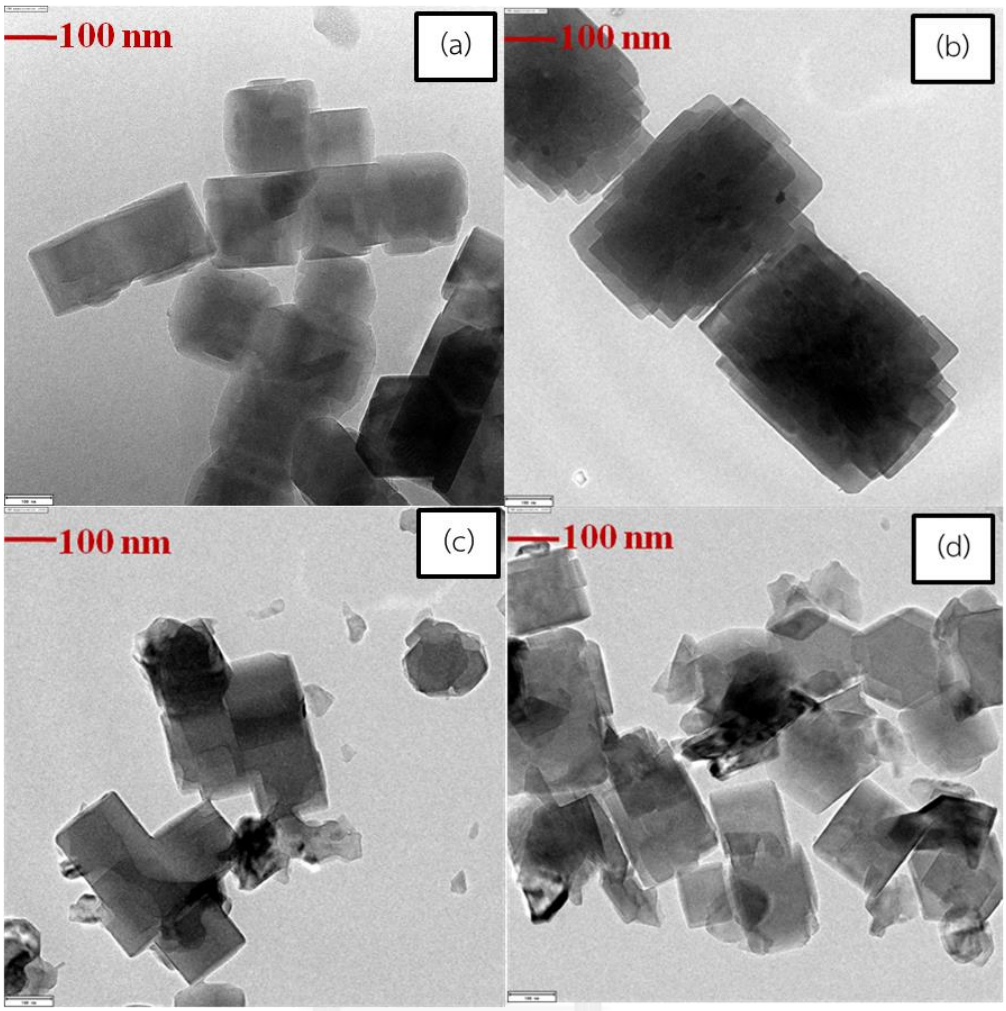

Figure 4.10 TEM images of V/TS-1 with different V-content; (a) 5wt.% V/TS-1, (b) 10wt.% V/TS-1, (c) 15wt.% V/TS-1 and (d) 20wt.% V/TS-1.

4.1.2.6 ICP-MS results

Inductively Coupled Plasma Mass Spectrometry (ICP-MS) was used for determination of the concentration of Si and Ti in the synthesized catalyst. The metal compositions were presented in Table 4.3. The Si/Ti mole ratio of TS-1, 5 wt.%, 10 wt.%, 15 wt.% and 20 wt.% of V/TS-1 were 51, 50, 51, 51 and 54, respectively. The results exhibited a higher deviation of Si/Ti mole ratio than the amount of metal in solution loading (Si/Ti mole ratio = 40) because some parts of Ti still remained in solution. Furthermore, the V-content in the catalysts was also

determined. The results of 5 wt.% and 10 wt.% V/TS-1 showed that the V-content was closed to stoichiometric values as 4.15 wt.% and 9.16 wt.%, respectively. On the contrary, the results of 15 wt.% and 20 wt.% V/TS-1 showed the amount of vanadium much lower than the V-content in impregnation solution. Therefore, the result suggests the parts of vanadium are in the structure of catalyst.

Table 4.3 Metal content analysis of V/TS-1 with different V-content.

Catalyst	Si/Ti mole ratio[a]	V-content (wt.%)[a]
TS-1	51	-
5wt.%V/TS-1	50	4.15
10wt.%V/TS-1	51	9.16
15wt.%V/TS-1	51	13.42
20wt.%V/TS-1	54	17.25

[a]Inductively Coupled Plasma Mass Spectrometry (ICP-MS)

4.2 The physico-chemical properties of bimetallic Ti-MWW

4.2.1 Effect of second metal (M/Ti-MWW)

4.2.1.1 XRD results

XRD patterns of as-synthesized and bimetallic Ti-MWW were showed in Figure 4.11. For as-synthesized Ti-MWW, XRD spectrum of sample showed a 001 diffraction at 2θ of 3.5° which is a characteristic peak of lamellar MWW structure [47]. After calcination, the 001 peak disappeared due to the removal of organic molecules between the layers while the h00 and hk0 peak still remained. This result indicated that the lamellar structure was transformed to three-dimensional MWW structure upon calcination process [47]. Following impregnation with second metal, all prepared materials exhibited the pattern of diffraction peaks corresponding to MWW structure between the 2θ from 5° to 30° which suggested that the Ti-MWW parent support was well retained. However, the peak intensity of bimetallic Ti-MWW catalysts was found to be reduced, resulting in decreasing of crystallinity. In addition, the higher angle diffraction was used to get more details about the loaded metal. Figure 4.11(b) showed the crystal structure of metallic phase. XRD pattern of Ce/Ti-MWW exhibited the peak corresponding to CeO_2 at 2θ = 28.5, 33.3, 47.5 and 56.4°. In the case of Cu/Ti-MWW, the diffraction peaks of CuO phase were observe at 2θ = 35.4, 38.5, 48.5, 57.9, 61.1, 67.5 and 75.5°. Furthermore, several peaks, which assigned to the Fe_2O_3 appeared at 2θ = 33.1, 35.6, 41.0, 49.4, 54.0, 62.4 and 63.9°for Fe/Ti-MWW. Additionally, the diffraction peaks at 2θ = 15.3, 20.3, 31.1 and 51.2°represented the presence of V_2O_5 in V/Ti-MWW sample. These results substantiated that the second metals were located on Ti-MWW.

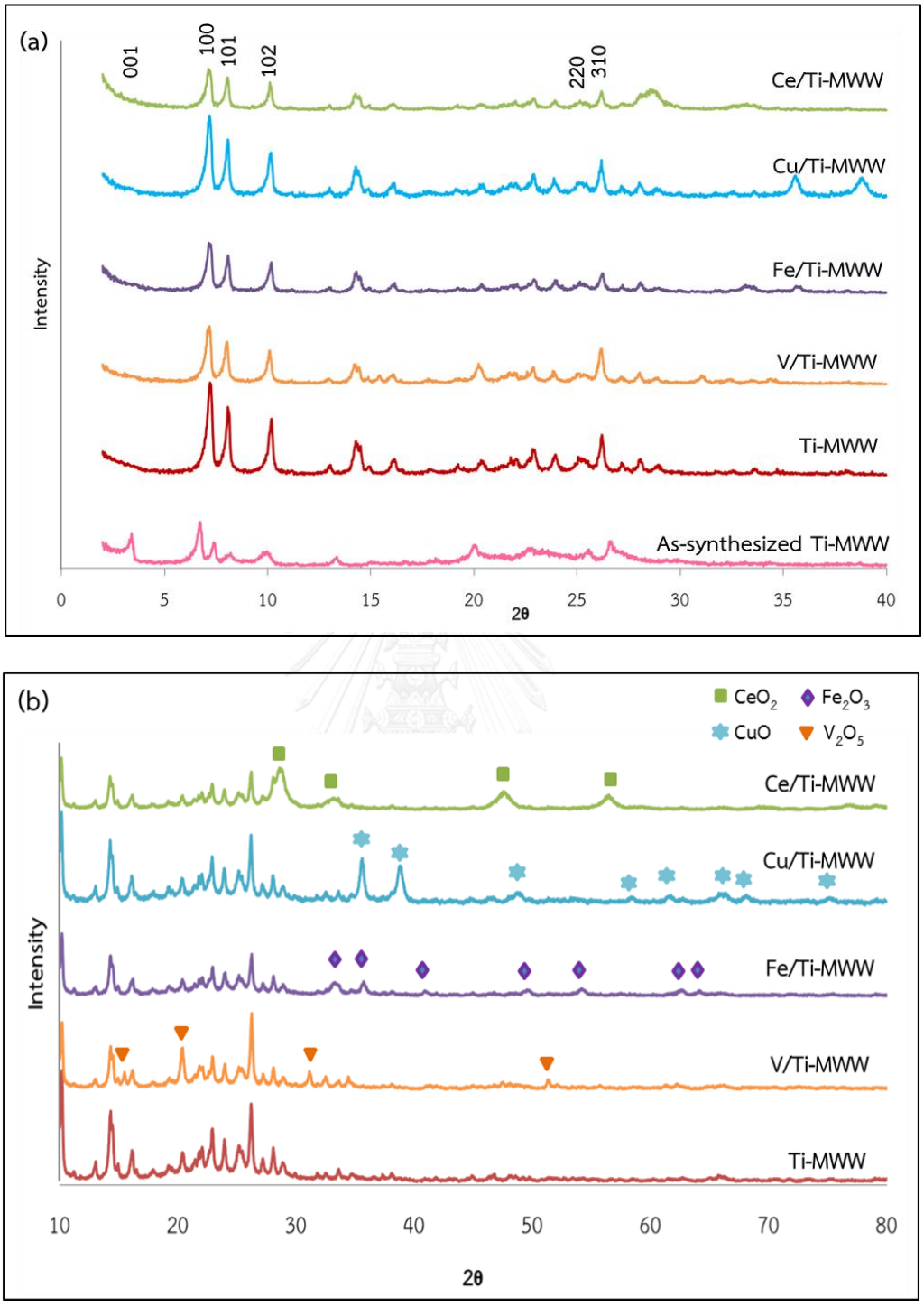

Figure 4.11 X-ray powder diffraction patterns of bimetallic Ti-MWW (M/Ti-MWW) in the range of (a) small-angle and (b) wide-angle.

4.2.1.2 DR-UV results

DR-UV spectra of metal supported on Ti-MWW were shown in Figure 4.12. For Ti-MWW support, the profile of sample displayed the strong absorption peaks at 210 and 320 nm, which can be ascribed to tetrahedral titanium and anatase phase, respectively. These results suggested the most of Ti atom occupy in tetrahedral position and small amount of anatase in the framework of Ti-MWW. After impregnation of second metals, a broad absorption peaks at 290 and 340 nm appeared for Ce/Ti-MWW. These peaks can be attributed to CeO_2 and small CeO_2 crystallites [57]. In the case of Cu/Ti-MWW, the absorption band at 210-270 nm corresponding to Cu ions that occupied isolated sites, while the band over 350 nm indicated the formation of Cu clusters to bulk CuO form [58]. Furthermore, the Fe/Ti-MWW exhibited the absorption band at 380, 420, 460, 500 and 540 nm. The band at 380 nm can be ascribed to small clusters or microaggregates of Fe_2O_3 particles and the strong peaks at 420, 460, 500 and 540 nm can be assigned to the aggregated Fe_2O_3 clusters [59, 60]. For V/Ti-MWW, DR-UV spectrum showed the absorption peaks at 210, 280, 340, 380, 420 and 500 nm. The intense peaks at 210 and 280 nm related to isolated tetrahedral V^{5+} species [61], while the peaks at 340 and 380 nm associated to low oligomeric tetrahedral V^{5+} species [61, 62]. Moreover, the absorption peaks at 420 and 500 nm indicated the presence of octahedral V^{5+} species and bulk V_2O_5, respectively [63, 64]. These results are consistent with XRD results, which reported the presence of metallic phase as CeO_2, CuO, Fe_2O_3 and V_2O_5 for the Ce/Ti-MWW, Cu/Ti-MWW, Fe/Ti-MWW and V/Ti-MWW catalysts, respectively.

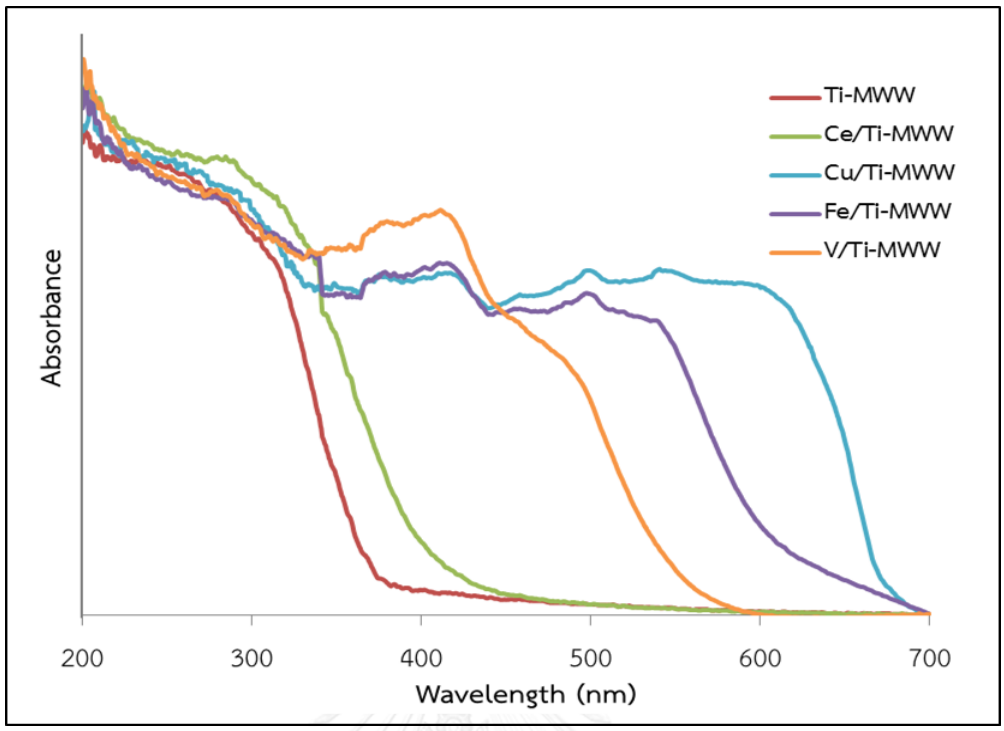

Figure 4.12 DR-UV spectra of M/Ti-MWW.

4.2.1.3 Sorption properties

N_2 adsorption/desorption isotherms of metal containing Ti-MWW were depicted in Figure 4.13. Ti-MWW exhibited isotherm type I with a H4 hysteresis loop, which is the characteristic of microporous material according to the IUPAC classification [67]. After impregnation of second metals, N_2 adsorption/desorption isotherms of bimetallic Ti-MWW was similar to parent material. This result indicated that the microporous structure of the materials was preserved after metal impregnation and calcination. Furthermore, the prepared catalysts mostly exhibited the main pore size distribution at 0.7 nm, as can be seen in Figure 4.13(b). However, some portion of the pores was around 1.6 nm. The textural properties of samples were shown in Table 4.4. The decrease of physical properties in terms of specific surface area and pore volume was caused by the deposition of metal oxide on the pore resulting in the clogging of the micropore.

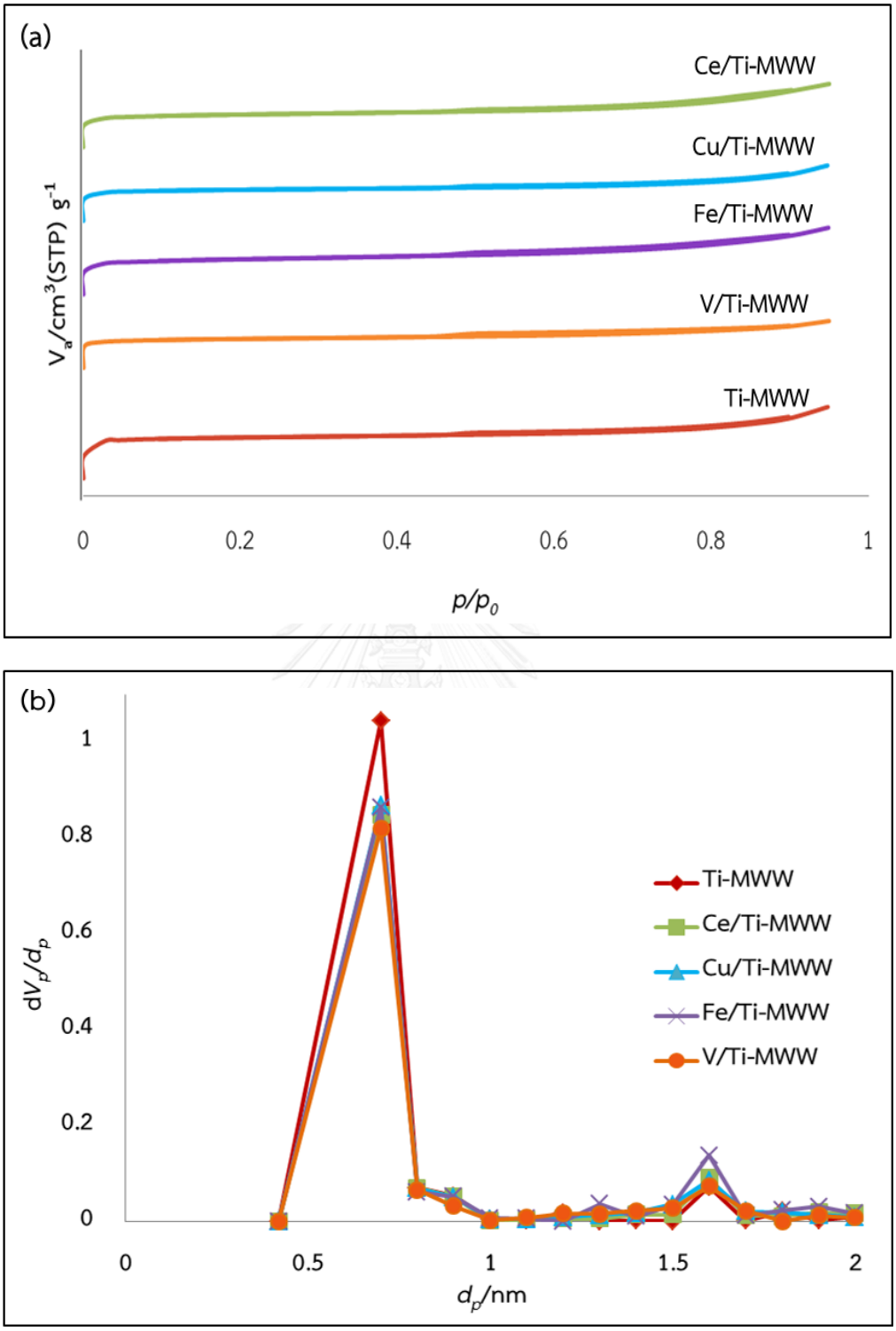

Figure 4.13 (a) N_2 adsorption/desorption isotherms and (b) pore size distributions of bimetallic Ti-MWW.

Table 4.4 Textural properties of the metal containing Ti-MWW (M/Ti-MWW).

Sample	Si/Ti	N_2 Adsorption/desorption		
		Specific surface area (BET)[a] ($m^2 g^{-1}$)	Pore volume ($cm^3 g^{-1}$)[b]	Pore diameter (nm)[b]
Ti-MWW	40	315	0.0858	0.7
Ce/Ti-MWW[c]	40	263	0.0727	0.7
Cu/Ti-MWW[c]	40	260	0.0754	0.7
Fe/Ti-MWW[c]	40	276	0.0783	0.7
V/Ti-MWW[c]	40	248	0.0740	0.7

[a]BET was calculated by $S_{BET} = S_{total}/a$; S_{BET} = the total surface area, S_{total} = the specific surface area, a = mass of the adsorbent

$S_{total} = (V_m N s)/V$; s = the adsorption cross section of the adsorbing species, N = Avogadro's number, V = the molar volume of the adsorbat gas, V_m= units of volume which are also the units of the molar volume of the adsorbate gas.

[b]reported by MP plot

[c]10wt.% metal supported on Ti-MWW

4.2.1.4 SEM images

Scanning electron micrographs of bimetallic Ti-MWW were shown in Figure 4.14. The micrograph of Ti-MWW exhibited the morphology of thin plate having the size about 2.2 μm in length and 0.25 μm in thickness. After impregnation of second metal, bimetallic Ti-MWW still retained thin plate morphology. Moreover, the thickness of Ce/Ti-MWW (0.18 μm), Fe/Ti-MWW (0.15 μm) and V/Ti-MWW (0.18 μm) particles was less than parent material whereas Cu/TiMWW (0.24 μm) was close to Ti-MWW.

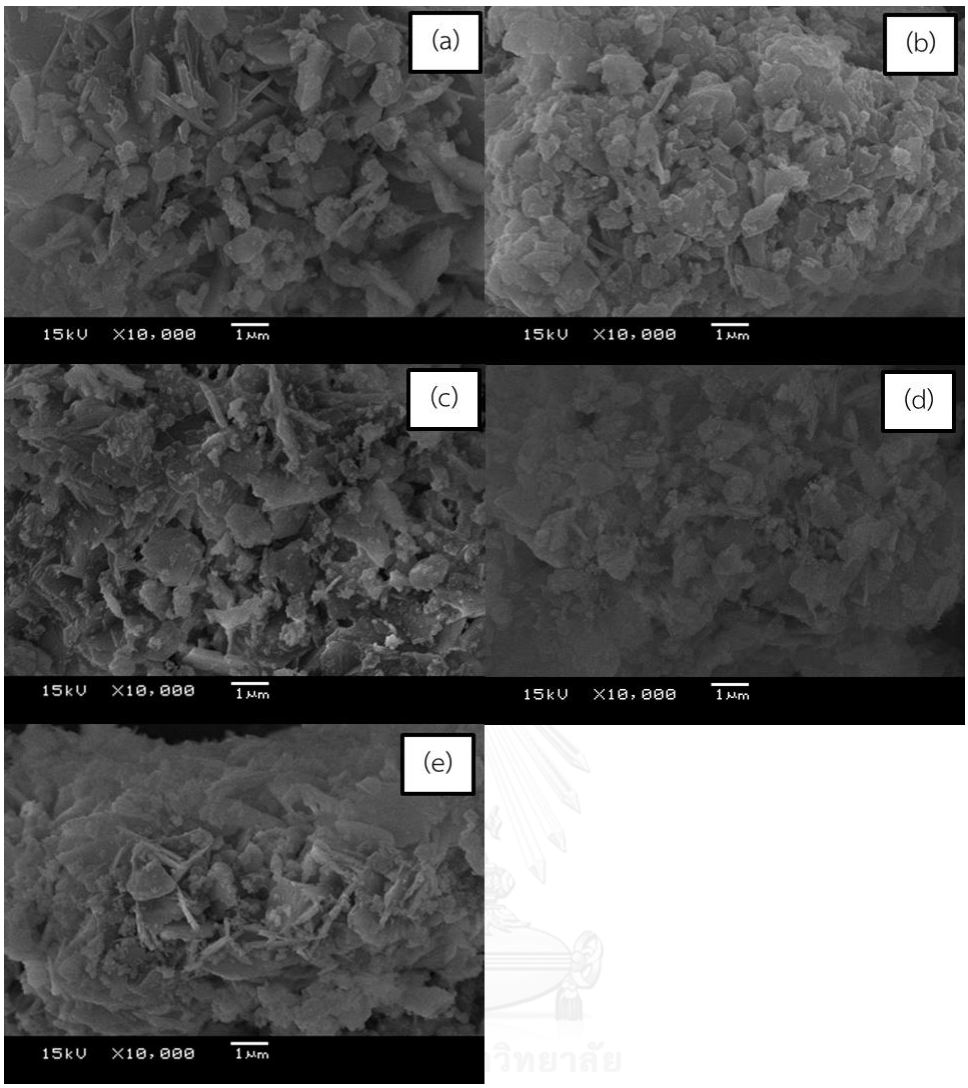

Figure 4.14 The SEM images of (a) Ti-MWW, (b) Ce/Ti-MWW, (c) Cu/Ti-MWW, (d) Fe/Ti-MWW and (e) V/Ti-MWW.

4.2.1.5 TEM images

The dispersion of metallic particles over Ti-MWW was investigated by transmission electron microscopy (TEM). As can be seen in Figure 4.15, TEM micrographs of Ce/Ti-MWW and Fe/Ti-MWW illustrated the aggregation of metal particles to form bulk metal oxide cluster on the surface of parent material. The sizes of CeO_2 and Fe_2O_3 were observed to be *ca.* 150-230 nm and 120-150 nm, respectively. These results were in agreement with the XRD results, which exhibited the high intense characteristic peak of CeO_2 and Fe_2O_3. Moreover, metallic particles of CuO exhibited a various sizes in the range of 10-140 nm. Among these bimetallic catalysts, V/Ti-MWW gave a better dispersion of metal particles with a narrow range of particle sizes about 10-50 nm. All of samples displayed evident bulk metallic species on the surface of Ti-MWW, which was consistent with XRD, N_2 adsorption/desorption and DR-UV results.

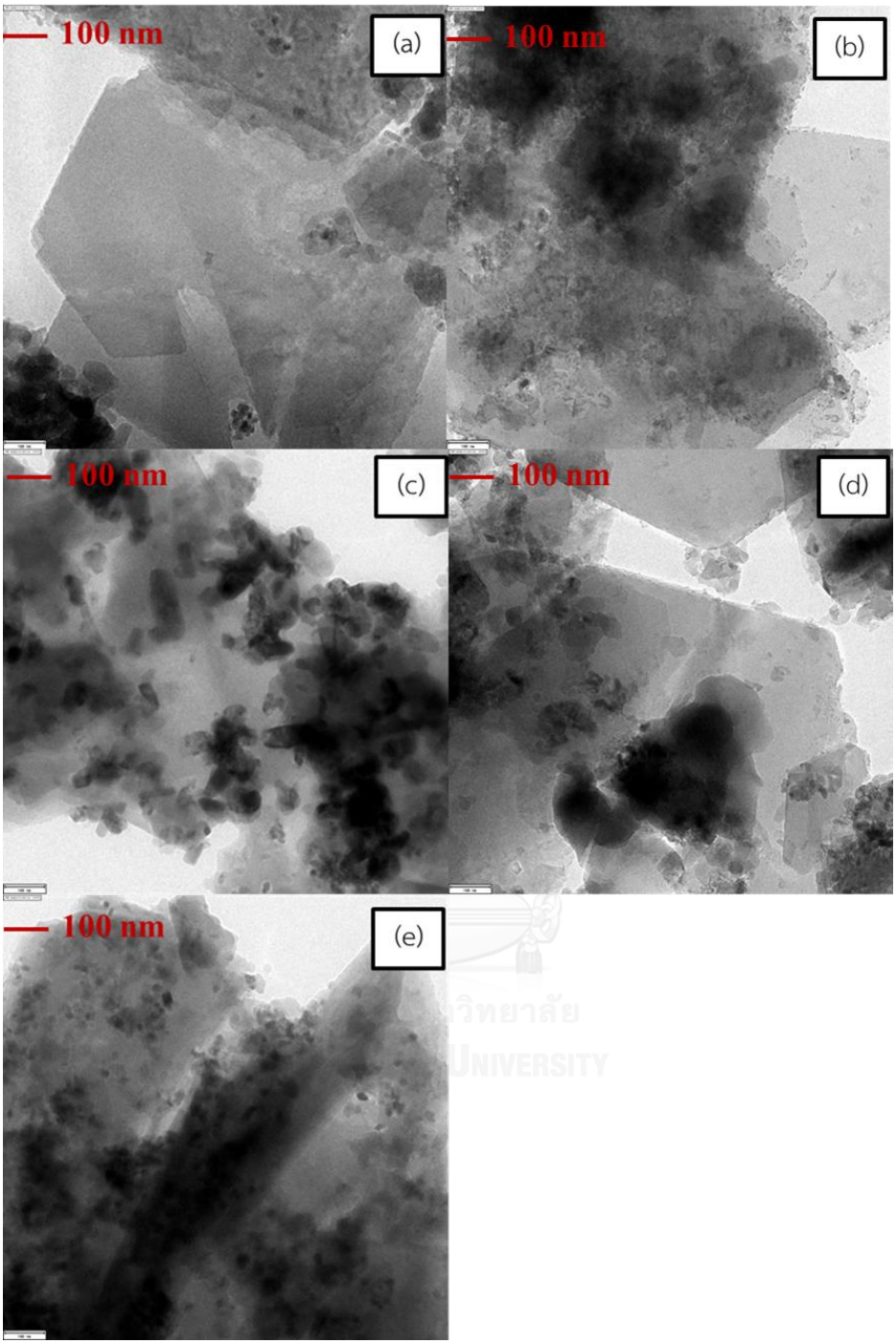

Figure 4.15 TEM images of (a) Ti-MWW, (b) Ce/Ti-MWW, (c) Cu/Ti-MWW, (d) Fe/Ti-MWW and (e) V/Ti-MWW.

4.2.2 Effect of vanadium content (V/Ti-MWW)

4.2.2.1 XRD results

Figure 4.16 showed the X-ray powder diffraction patterns of vanadium supported on Ti-MWW with different V-contents in the range of small-angle and wide-angle. All synthesized catalysts exhibited the pattern of diffraction peaks between the 2θ from 5° to 30°that corresponding to MWW structure. This result suggested that the MWW structure was maintained after modification. However, the intensity of diffraction peaks gradually decreased with increasing the amount of V loading due to crystallinity attenuation. To compare the crystalline phase, the wide-angle X-ray diffraction was also determined. The results are shown in Figure 4.16(b). Characteristic diffraction peaks of vanadium species were not found in VO-propyl-NH_2-anchoring on Ti-MWW diffractogram. In the case of V/Ti-MWW, at 2.5 wt.% V/Ti-MWW, the characteristic peak of V_xO_y was not observed which indicated good dispersion of the loaded vanadium on the surface of Ti-MWW. With the vanadium concentration up to 5 wt.%, low intense characteristic diffraction peaks of V_2O_5 were found at 2θ = 20.3, 31.1 and 51.2°. Furthermore, five additional peaks of V_2O_5 at 2θ = 15.3, 32.4, 34.3, 61.1 and 62.3°were observed for V/Ti-MWW at 10 wt.% of vanadium. With the increase of vanadium loading to 20wt.%, although the peak position of V_2O_5 does not change considerably when compared with XRD pattern of 15 wt.% V/Ti-MWW, the intensity of those peaks increased obviously. It means that more bulk V_2O_5 was obtained. Therefore, V dispersion on the surface of Ti-MWW decreased with increasing V loading, resulting in the formation of bulk V_2O_5. These results can be confirmed by TEM micrographs.

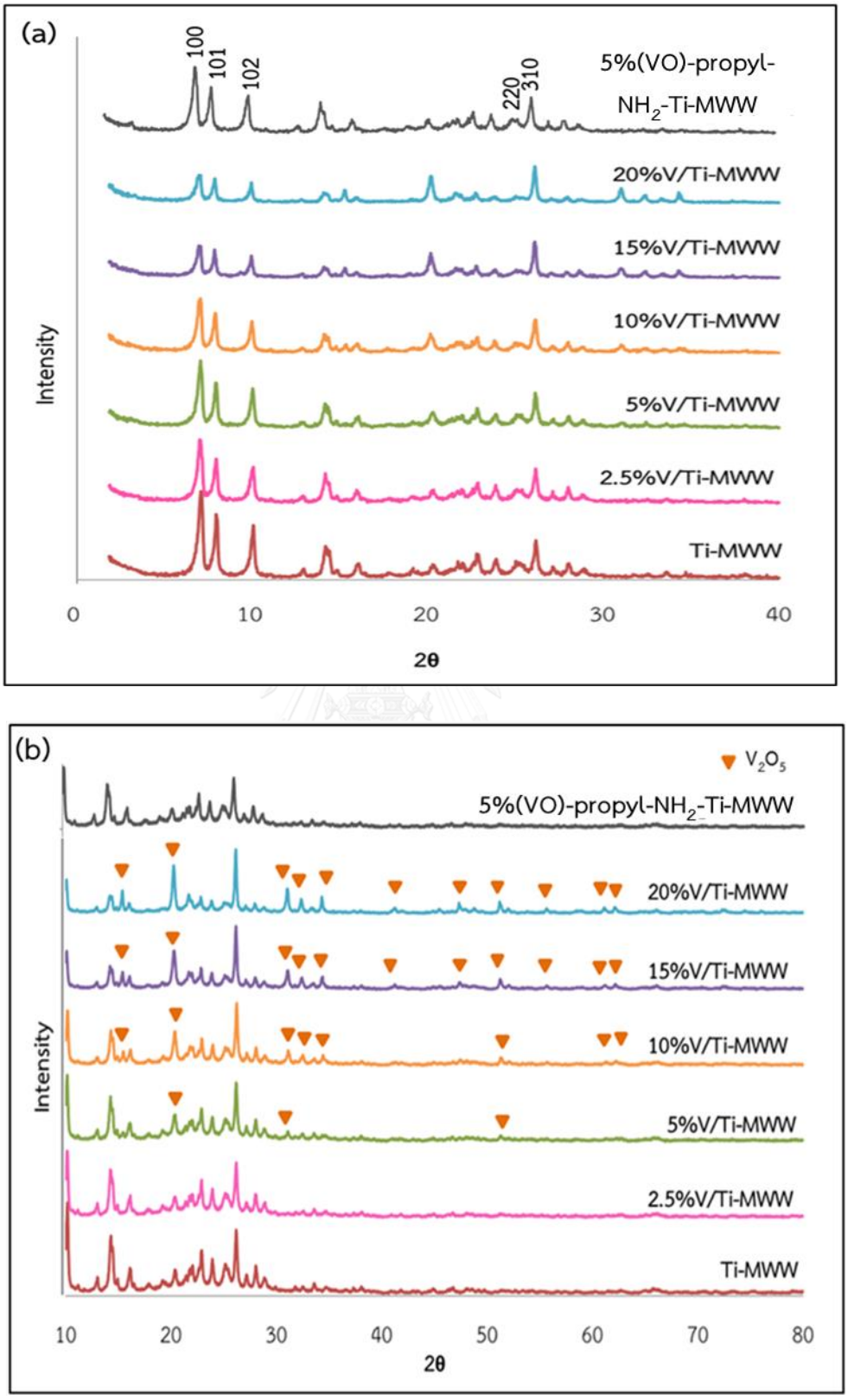

Figure 4.16 X-ray powder diffraction patterns of V/Ti-MWW with different V-contents in the range of (a) small-angle and (b) wide-angle.

4.2.2.2 DR-UV results

DR-UV spectra of VO-propyl-NH_2-anchoring on Ti-MWW and V/Ti-MWW with different V-contents were recorded. The results were shown in Figure 4.17. For VO-propyl-NH_2-anchoring on Ti-MWW, DR-UV spectrum showed absorption bands at 280 and 340 nm that can be ascribed to tetrahedrally coordinated V^{5+} species and low oligomeric tetrahedral coordinated V^{5+} species, respectively [61, 62]. Moreover, weak broad absorption band at 600-700 nm which corresponding to $(VO)^{2+}$ was also found [50]. In the case of V/Ti-MWW, at the lowest content of vanadium (2.5 wt.%), an intense bands at 210 and 280 nm, which can be attributed to the isolated tetrahedral V^{5+} species were observed [61]. Moreover, the absorption band at 380 and 420 nm with a shoulder band at 500 nm were also found. The band at 380 can be ascribed to low oligomeric tetrahedral V^{5+} species, while two absorption band at 420 and 500 nm indicated to octahedral V^{5+} species and bulk V_2O_5, respectively [62-64]. As vanadium concentration was up to 5wt.%, the intensities of both absorption bands at 210 and 280 nm increased significantly. It means that more isolated tetrahedral V^{5+} species was obtained when increasing amount of V loading. At the same time, the intensities of the absorption bands at 420 and 500 nm were also increased because high formation of octahedral V^{5+} species and bulk V_2O_5. At the higher amount of V loading (10-20 wt.%), the increase of the intensities of the absorption bands at 420 and 500 nm with increasing vanadium content related to the presence of vanadium species with a larger polymerization degree to bulk V_2O_5 formation. DR-UV spectroscopy has confirmed that the isolated tetrahedral V^{5+} species and low oligomeric tetrahedral V^{5+} species is mainly form of V species at low vanadium content while octahedral V^{5+} species and bulk V_2O_5 become more abundant at higher V loading.

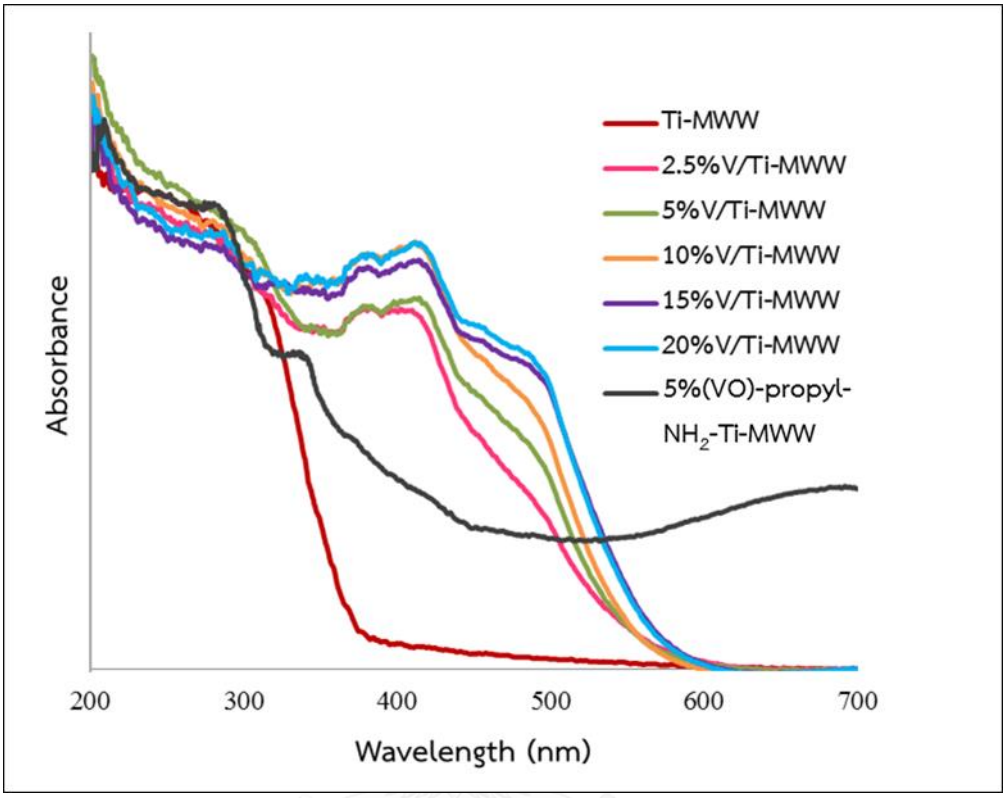

Figure 4.17 DR-UV spectra of V/TS-1 with different V-contents.

4.2.2.3 Sorption properties

Nitrogen adsorption/desorption isotherms and pore size distributions of V/Ti-MWW with various V-contents (0-20 wt.%) were presented in Figure 4.18. All of prepared materials displayed microporous texture with characteristic type I isotherms and H4-type hysteresis loop. This result indicated that the microscopic order of parent material was maintained. In addition, the pore sized distributions of all samples showed a narrow peak centered at 0.7 nm with a small portion of pore at 1.6 nm. The surface properties of the samples were summarized in Table 4.5. The increase of vanadium content resulted in a decrease in N_2 adsorption capacity, reflecting a reduction in surface area and pore volume. The loss of pore volume indicated that the loaded metals entered the pore of Ti-MWW. This phenomenon was also found in VO-propyl-NH_2-anchoring on Ti-MWW. However, at the high V-content (15-20 wt.%), the larger decrease in the pore volume and surface area was observed but the pore diameter of samples was not changed. These results were confirmed to be caused by the clogging of partial pores by vanadium oxide species.

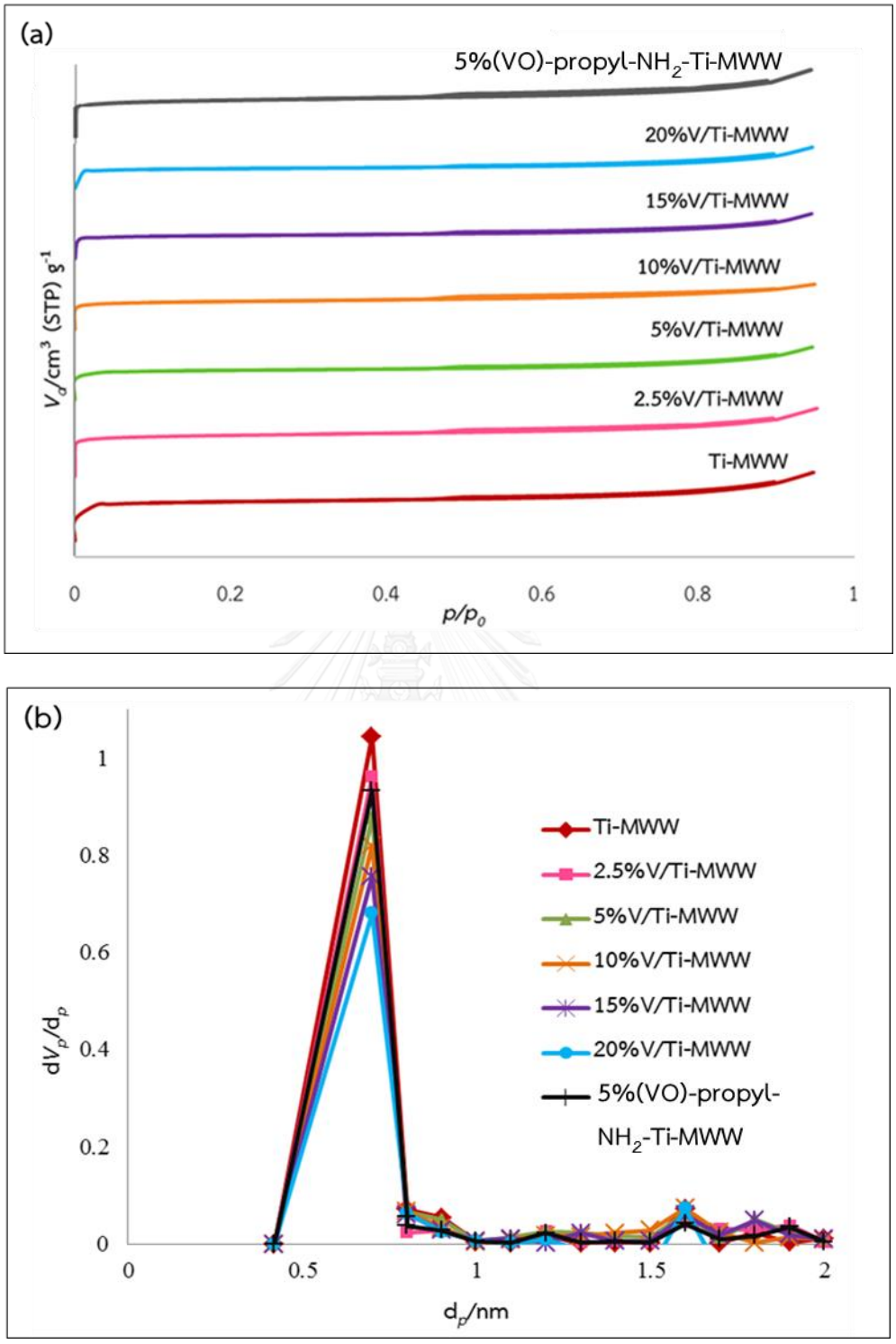

Figure 4.18 (a) N_2 adsorption/desorption isotherms and (b) pore size distributions of V/Ti-MWW with different V-contents.

Table 4.5 Textural properties of the vanadium containing Ti-MWW with various V-contents.

Sample	Metal content (wt.%)	Si/Ti	N_2 Adsorption/desorption		
			Specific surface area (BET)[a](m^2g^{-1})	Pore volume (cm^3g^{-1})[b]	Pore diameter (nm)[b]
Ti-MWW	-	40	315	0.0858	0.7
V/Ti-MWW	2.5	40	290	0.0767	0.7
	5	40	256	0.0758	0.7
	10	40	248	0.0740	0.7
	15	40	224	0.0667	0.7
	20	40	204	0.0551	0.7
VO-propyl-NH_2-Ti-MWW	5	40	270	0.0764	0.7

[a]BET was calculated by $S_{BET} = S_{total}/a$; S_{BET} = the total surface area, S_{total} = the specific surface area, a = mass of the adsorbent

$S_{total} = (V_mNs)/V$; s = the adsorption cross section of the adsorbing species, N = Avogadro's number, V = the molar volume of the adsorbat gas, V_m= units of volume which are also the units of the molar volume of the adsorbate gas.

[b]reported by MP plot

4.2.2.4 SEM images

The morphologies of V/Ti-MWW with various V-contents were monitored by Scanning electron microscope (SEM). The results were shown in Figure 4.19. SEM micrographs of all samples displayed thin plate morphology. At the lower vanadium content (2.5-10wt.%), the thickness of plate was less than Ti-MWW and it was agglomerated to large particles when increasing the amount of V loading to 15 and 20 wt.%. The plate thickness of V/Ti-MWW with low vanadium content (2.5-10 wt.%), as well as VO-propyl-NH_2-anchoring on Ti-MWW, is in the range of 0.08-0.19 μm whereas 0.14-0.30 μm for V/Ti-MWW with high concentration of vanadium at 15 and 20 wt.%.

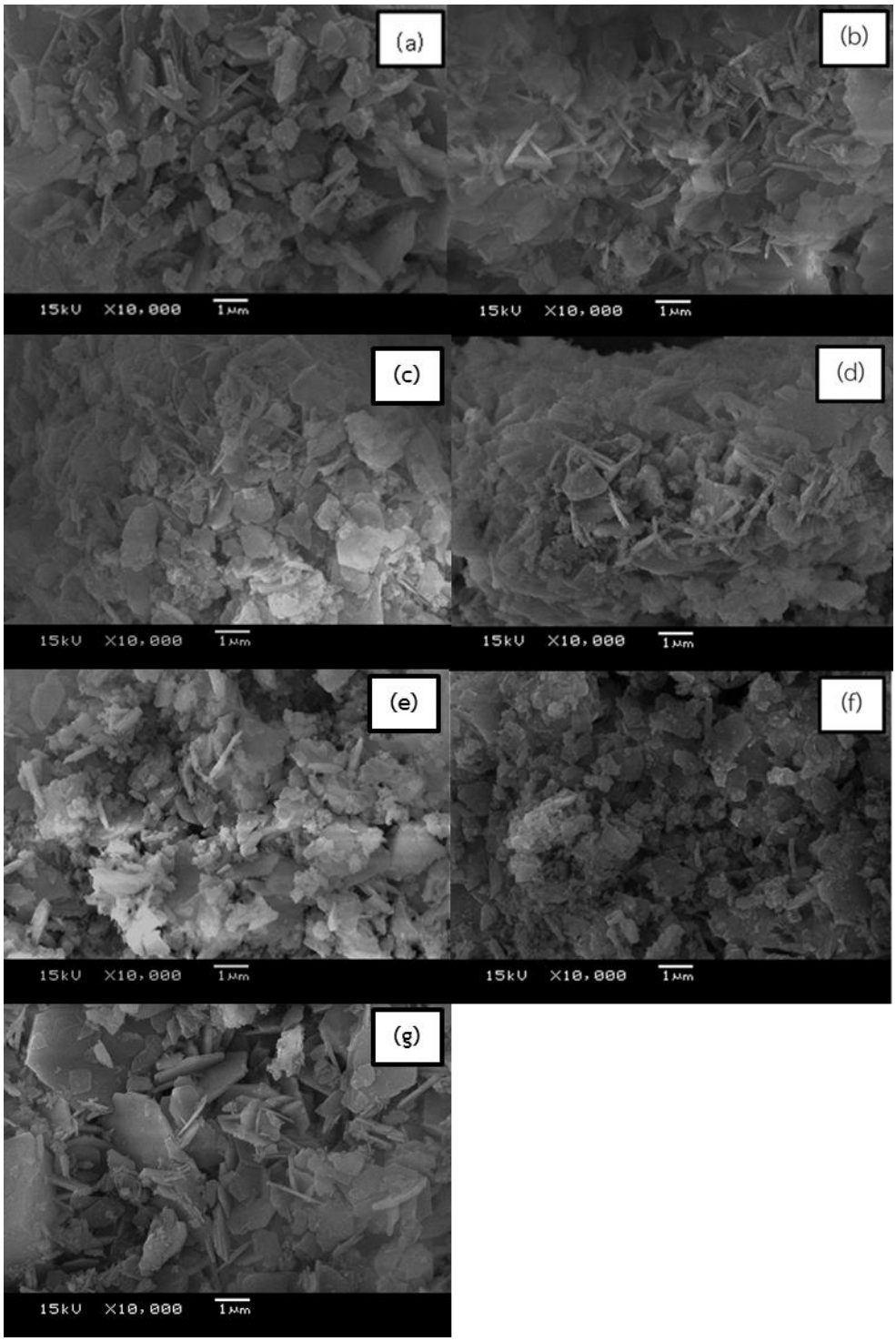

Figure 4.19 The SEM images of V/Ti-MWW with different V-content; (a) Ti-MWW, (b) 2.5wt.% V/Ti-MWW, (c) 5wt.%V/Ti-MWW, (d) 10wt.% V/Ti-MWW, (e) 15wt.%V/Ti-MWW, (f) 20wt.%V/Ti-MWW and (g) 5%VO-propyl-NH_2-anchoring on Ti-MWW.

4.2.2.5 TEM images

TEM micrographs of V/Ti-MWW with different V-content were shown in Figure 4.20. At 5-15 wt.%, vanadium oxide particles, which dispersed on the surface of Ti-MWW, consisted of small and aggregated particles. The small metallic particles were observed with sizes in the range 7-14 nm, 10-21 nm and 14-21 nm for 5, 10 and 15 wt.% V/Ti-MWW, respectively. In the case of aggregated particles, vanadium oxide species were agglomerated having size 15-29 nm, 22-36 nm and 22-100 nm by increasing the amount of V loading to 5, 10 and 15 wt.%, respectively. In addition, on the surface of V/Ti-MWW with 20 wt.% of vanadium, majority of the vanadium oxide particles were present in the form of aggregated particles with mean particle diameter of 39-143 nm. For 5 wt.% VO-propyl-NH_2-anchoring on Ti-MWW, highly dispersion of small particles of vanadium oxide with sizes in the range 5-11 nm was observed. These results can be confirmed that metal dispersion capacity depended on the concentration of loaded metal.

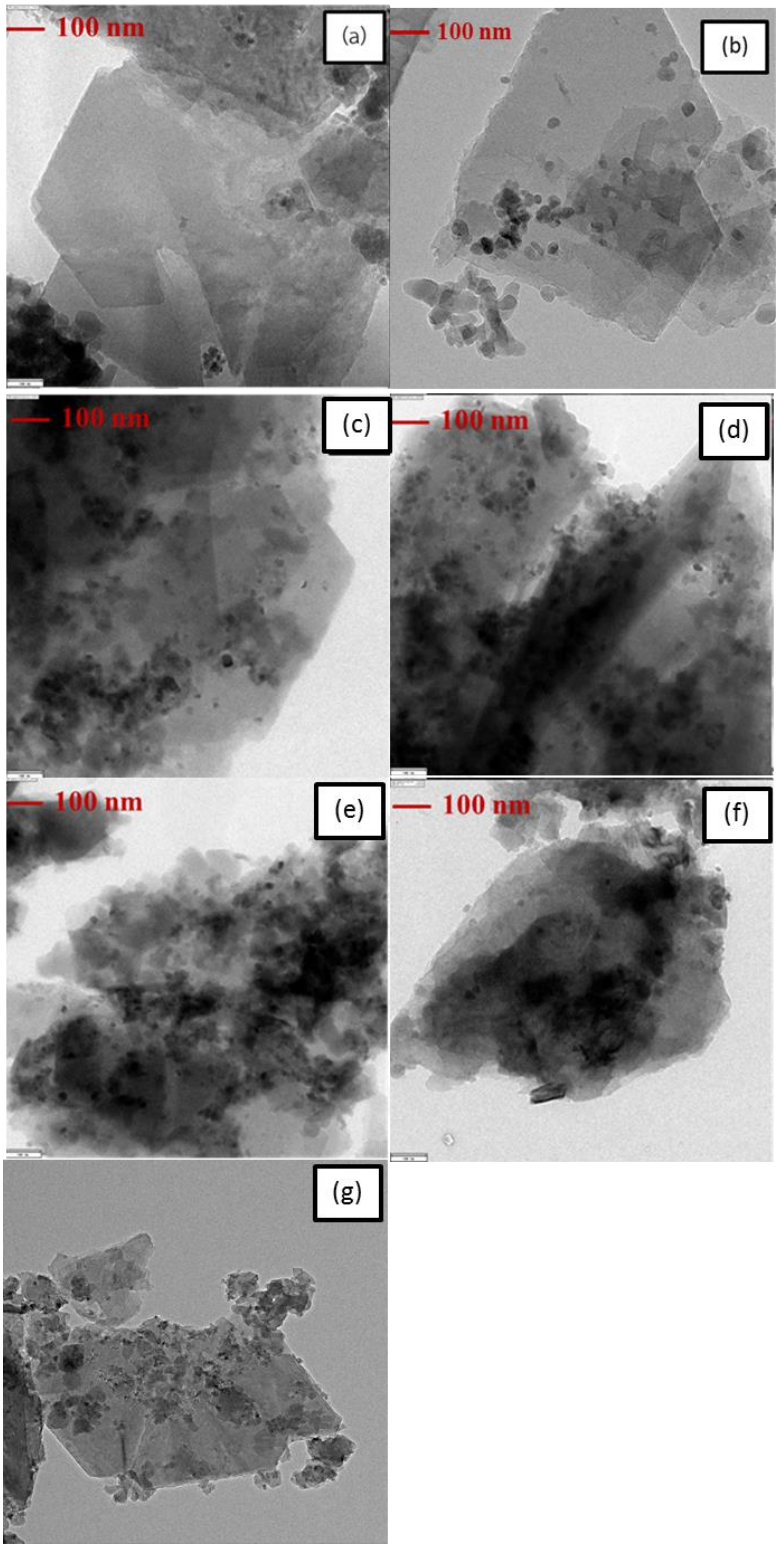

Figure 4.20 The TEM images of V/Ti-MWW with different V-content; (a) Ti-MWW, (b) 2.5wt.% V/Ti-MWW, (c) 5wt.% V/Ti-MWW, (d) 10wt.% V/Ti-MWW, (e) 15wt.% V/Ti-MWW, (f) 20wt.% V/Ti-MWW and (g) VO-propyl-NH_2-anchoring on Ti-MWW.

4.2.2.6 ICP-MS results

Table 4.6 showed the elemental analysis data of V/Ti-MWWs with different amount of V loading. The content of metals was determined by Inductively Coupled Plasma Mass Spectrometer (ICP-MS). From the result, the Si/Ti mole ratio, which determined by ICP-MS was nearly to the amount of metal in the impregnated solution. Additionally, the vanadium content of 2.5, 5, 10 and 15 wt.% of V/Ti-MWW from ICP-MS was closed to the value from impregnation solution whereas the amount of vanadium at 20 wt.% V/Ti-MWW and 5 wt.% VO-propyl-NH_2-anchoring on Ti-MWW showed much lower than the stoichiometric adding value.

Table 4.6 Metal content analysis of V/Ti-MWW with different V-content.

Catalyst	Si/Ti mole ratio[a]	V-content (wt.%)[a]
Ti-MWW	47	-
2.5wt.%VTi-MWW	41	2.32
5wt.%V/Ti-MWW	39	4.35
10wt.%V/Ti-MWW	38	9.20
15wt.%V/Ti-MWW	42	14.04
20wt.%V/Ti-MWW	38	17.40
5wt.% VO-propyl-NH_2-anchoring on Ti-MWW	44	3.97

[a]Inductively Coupled Plasma Mass Spectrometry (ICP-MS)

4.2.2.7 FT-IR results

Figure 4.21 showed the FT-IR spectra in the 500-4000 cm^{-1} region of prepared materials. All of materials exhibited the characteristic bands of Si–O–Si asymmetric stretching (1100 and 1220 cm^{-1}), Si–O–Si symmetric stretching (680 and 800 cm^{-1}), Si-O-Si bending (500, 550 and 600 cm^{-1}), Ti-O-Ti stretching (1400 cm^{-1}) and Ti-O-Si bonds (950 cm^{-1}) [68-70]. In addition, the spectra presented two bands of O-H bending (1630 cm^{-1}) and stretching (3440 cm^{-1}) of water[71]. In the case of propyl-NH_2- anchoring on Ti-MWW (Figure 4.21(b)) and (VO)-propyl-NH_2-anchoring on Ti-MWW (Figure 4.21(c)), the band of N-H stretching cannot be seen in the spectra because it overlapped with 3440 cm^{-1} band of hydroxyl group. However, FT-IR spectra of two samples displayed the N-H bending, C-H stretching (2940 cm^{-1}) and Si-C bonds (740 cm^{-1})[50]. For propyl-NH_2-anchoring on Ti-MWW (Figure 4.21(b)), FT-IR spectrum displayed the N-H bending (695 and 1550 cm^{-1}) and C-H stretching (2940 cm^{-1}) of the propyl group[50]. This result indicated the presence of $–Si-(CH_2)_3NH_2$ on the surface of Ti-MWW. In the FT-IR spectrum of (VO)-propyl-NH_2-anchoring on Ti-MWW (Figure 4.21(c)), the original N-H bending at 1550 cm^{-1} was shifted to 1510 cm^{-1} due to the presence of vanadium. The IR spectra substantiated that amino groups were coordinated with $(VO)^{2+}$ ions and it was presented on the surface of Ti-MWW.

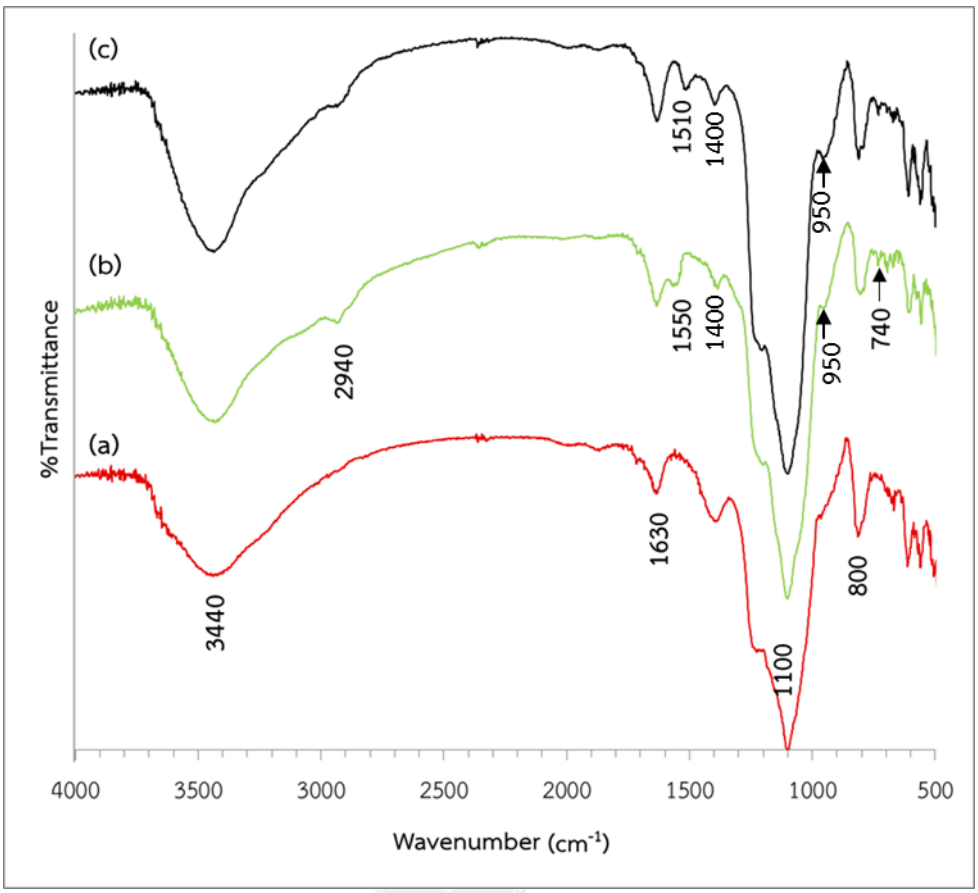

Figure 4.21 FT-IR spectra of (a) Ti-MWW, (b) propyl-NH_2-anchoring on Ti-MWW and (c) (VO)-propyl-NH_2-anchoring on Ti-MWW.

4.2.2.8 NMR results

The ^{13}C NMR spectrum of propyl-NH_2-anchoring on Ti-MWW (Figure 4.22(a)) exhibited the resonance peaks at **δ** = 11.0, 21.5 and 43.5 ppm, which were associated to the three carbon atoms of 3-aminopropyl groups (–Si-$^{1}CH_2$-$^{2}CH_2$-$^{3}CH_2$-NH_2) at ^{1}C, ^{2}C and ^{3}C, respectively[72]. After immobilization of vanadium, the ^{13}C NMR spectrum of (VO)-propyl-NH_2-anchoring on Ti-MWW (Figure 4.22(b)) showed signals that attributed to the ^{1}C, ^{2}C and ^{3}C carbon species of propyl group. This result confirmed that the grafted 3-aminopropyltrimethoxysilane functionalities preserved their structural integrity after modification and amino propyl group was in the structure of catalysts.

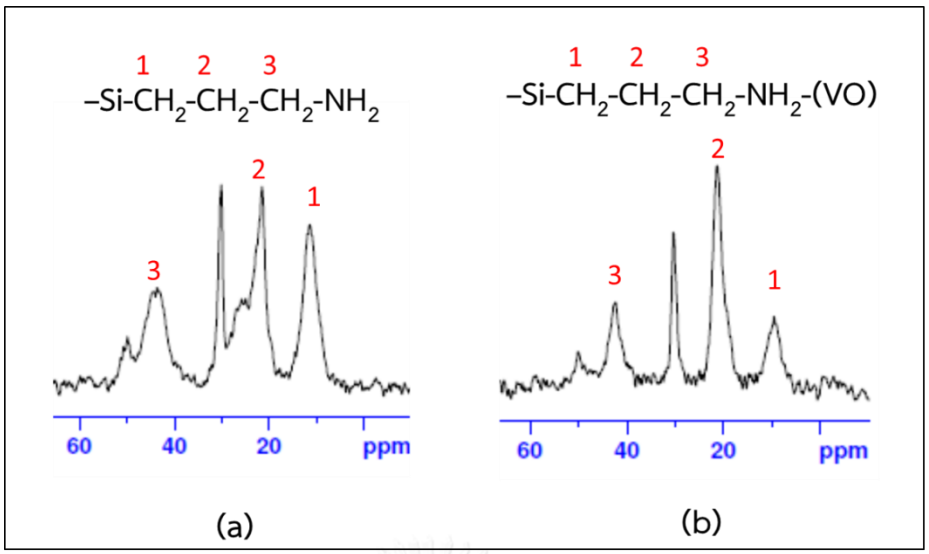

Figure 4.22 ^{13}C NMR spectra of (a) propyl-NH_2-anchoring on Ti-MWW and (b) (VO)-propyl-NH_2-anchoring on Ti-MWW

4.2.3 Effect of Si/Ti mole ratio

4.2.3.1 XRD results

X-ray powder diffraction patterns of Ti-MWW with Si/Ti ratio in gel about 40, 70 and 100 were shown in Figure 4.21. All samples exhibited diffraction peaks that corresponding to MWW structure. However, the intensity of peaks decreased significantly when increasing the amount of Ti (decrease of Si/Ti mole ratio). This result indicated that the incorporation of titanium atom caused the loss of ordered MWW structure that affecting on the crystallinity. At the higher angle (Fig. 4.21), the characteristic diffraction peaks of anatase phase were not observed due to the absence of the anatase phase or the trace amount of anatase phase that cannot be detected by XRD.

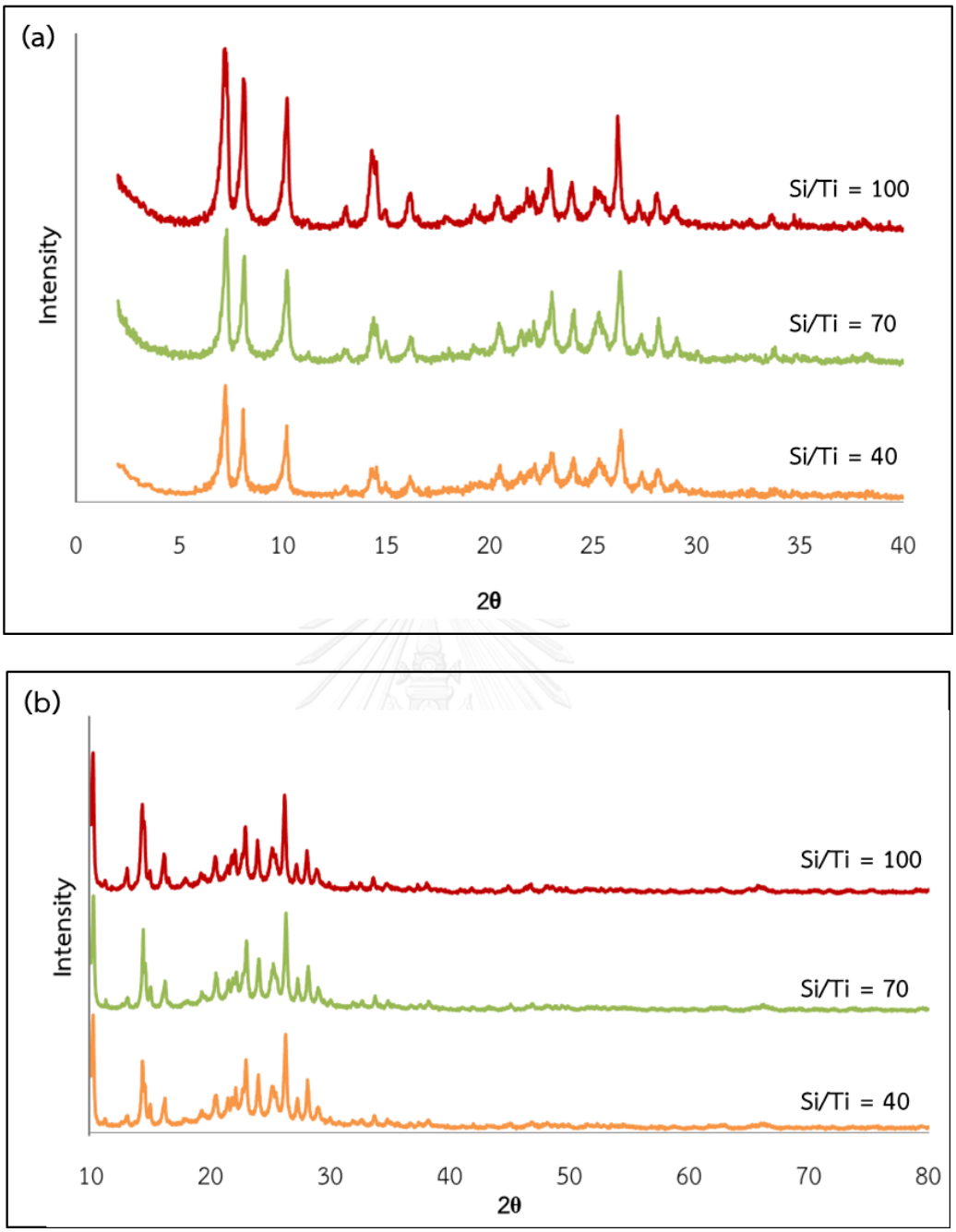

Figure 4.23 X-ray powder diffraction patterns of Ti-MWW with different Si/Ti mole ratio in the range of (a) small-angle and (b) wide-angle.

4.2.3.2 DR-UV results

DR-UV spectra of Ti-MWW at three Si/Ti mole ratios were shown in Figure 4.22. At Si/Ti mole ratio 70 and 100, both prepared materials displayed the strong absorption band only at ≈210 nm that can be ascribed to a charge transfer from oxygen to tetracoordinated titanium. With increasing Ti concentration (Si/Ti mole ratio 40), not only band at 210 nm was observed, the absorption band at 320 nm was also found. The band at 320 nm is a characteristic band of anatase phase. The above results suggested that the major amount of titanium atom located at the tetrahedral coordinating position for Ti-MWW with Si/Ti = 70 and 100 whereas Ti atom of Ti-MWW at Si/Ti = 40 occupy in tetrahedral position and small amount of anatase.

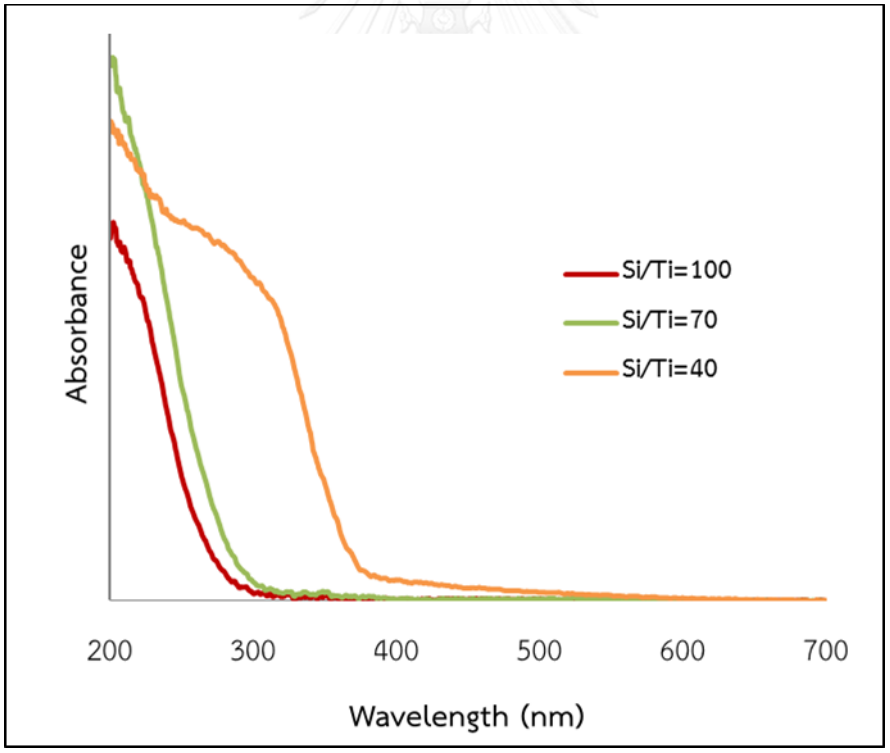

Figure 4.24 DR-UV spectra of Ti-MWW with different Si/Ti mole ratio.

4.2.3.3 Sorption properties

The nitrogen adsorption/desorption measurements suggested that the isotherms for all products showing the typical type I as defined by IUPAC for microporous material, as can be seen from Figure 4.23(a). In addition, the pore size distributions became broader as the content of Ti atom increased, which indicated the decreasing structural ordering of sample. However, pore size distribution of all samples centered mostly at 0.7 nm. The surface properties of Ti-MWW with different Si/Ti mole ratio were summarized in Table 4.7. The increase of titanium caused a decrease of specific surface area and pore volume due to the diameter of titanium atom is larger than silicon atom.

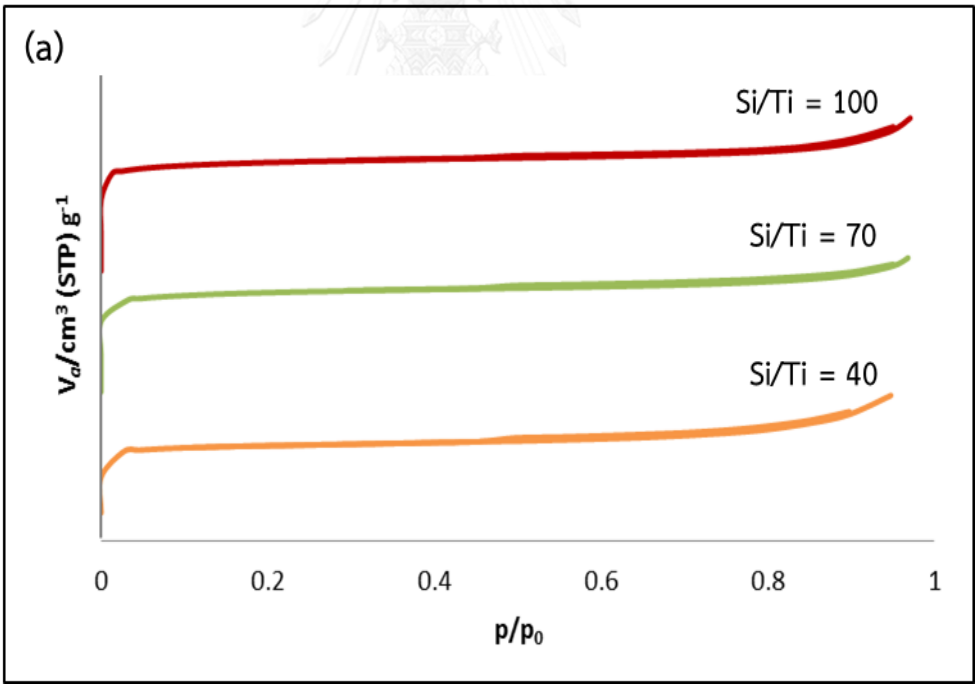

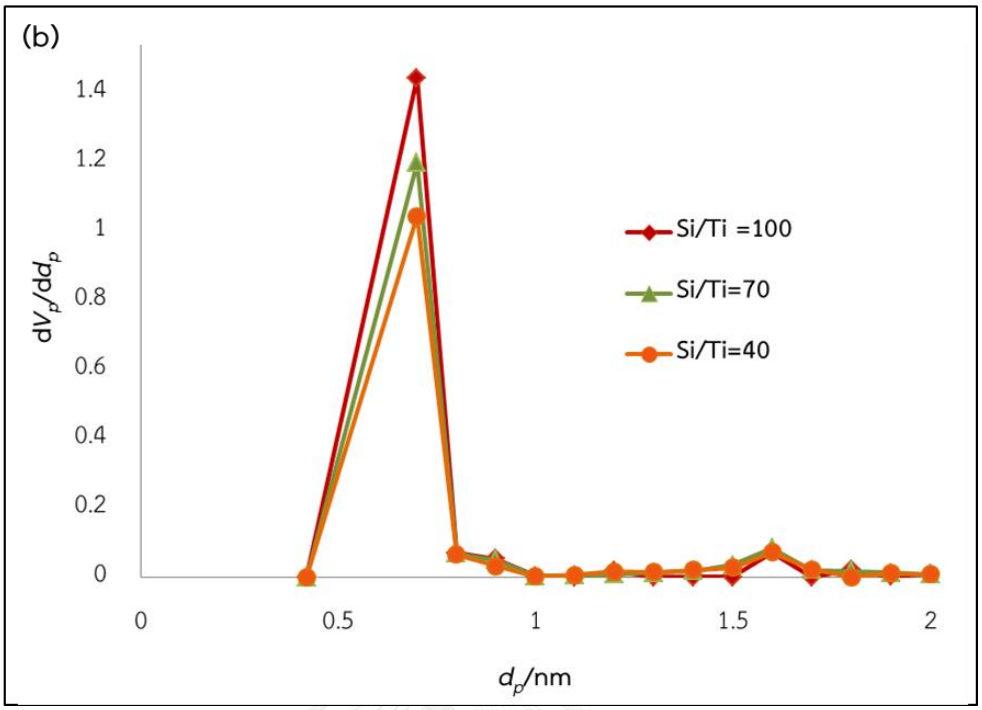

Figure 4.25 (a) N_2 adsorption/desorption isotherms and (b) pore size distributions of Ti-MWW with different Si/Ti mole ratio.

Table 4.7 Textural properties of the Ti-MWW with different Si/Ti mole ratio

Sample	Si/Ti	N_2 Adsorption/desorption		
		Specific surface area (BET)[a] ($m^2 g^{-1}$)	Pore volume ($cm^3 g^{-1}$)[b]	Pore diameter (nm)[b]
Ti-MWW	100	351	0.0884	0.7
	70	334	0.0869	0.7
	40	315	0.0853	0.7

[a]BET was calculated by $S_{BET} = S_{total}/a$; S_{BET} = the total surface area, S_{total} = the specific surface area, a = mass of the adsorbent

$S_{total} = (V_m N s)/V$; s = the adsorption cross section of the adsorbing species, N = Avogadro's number, V = the molar volume of the adsorbat gas, V_m= units of volume which are also the units of the molar volume of the adsorbate gas.

[b]reported by MP plot

4.2.3.4 SEM images

Figure 4.24 illustrated scanning electron micrographs of Ti-MWW which synthesized at different Si/Ti mole ratio. Morphology of all prepared materials displayed thin plate shape with size 0.25 μm in thickness.

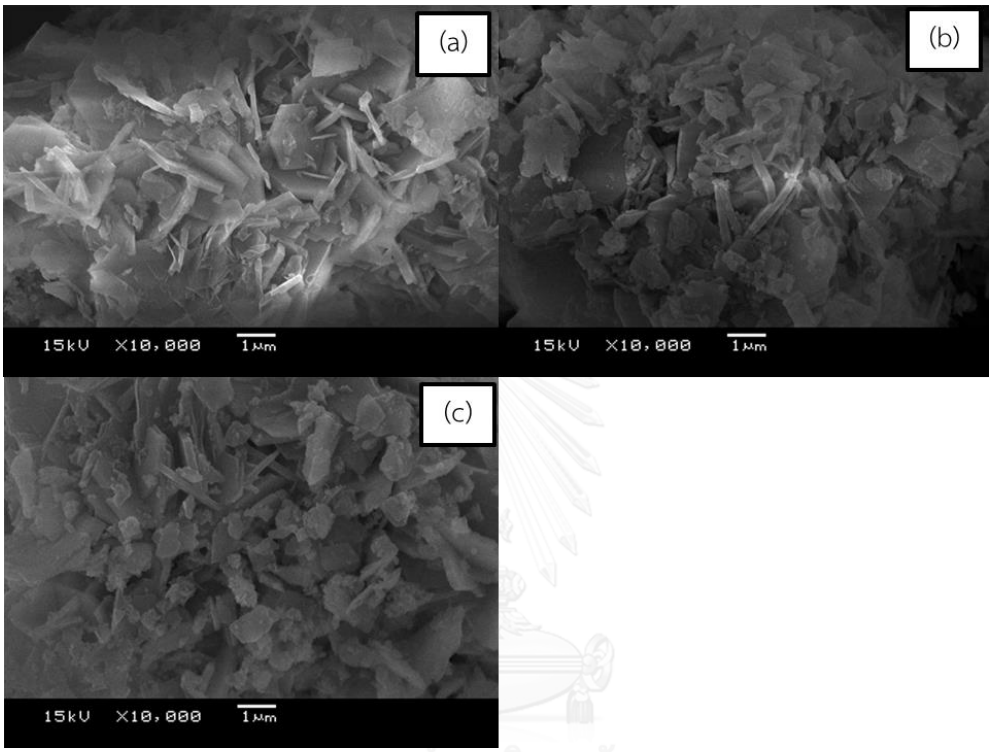

Figure 4.26 SEM image of Ti-MWW with different Si/Ti mole ratio; (a) Si/Ti=100, (b) Si/Ti=70 and (c) Si/Ti=40.

4.2.3.5 ICP-MS results

The amount of Ti in the MWW structure was analyzed by ICP-MS. The results are shown in Table 4.8. The Si/Ti mole ratio in all materials showed a higher value than the theoretical ratio resulting from a lower Ti-content. This result indicated that the some part of Ti still remained in solution.

Table 4.8 Metal content analysis of Ti-MWW with different Si/Ti mole ratio.

Catalyst	Si/Ti mole ratio in gel	Si/Ti mole ratio from ICP[a]
Ti-MWW	100	110
	70	77
	40	47

[a]Inductively Coupled Plasma Mass Spectrometry (ICP-MS)

4.3 The physico-chemical properties of bimetallic Ti-MCA

4.3.1 Effect of second metal (M/Ti-MCA)

4.3.1.1 XRD results

XRD patterns of bimetallic Ti-MCA were evaluated in the range of small-angle and wide-angle X-ray diffraction, as shown in Figure 4.25. Ti-MCA material exhibited two main diffraction peaks of cubic Ia-3d structure at 2θ that corresponding to 211 and 220 [34]. That indicated the titanium-incorporated cubic Ia-3d mesoporous silica (Ti-MCA) was successfully synthesized by directly hydrothermal method. After impregnation, the patterns of M/Ti-MCA were similar to the parent material. These results suggested that the cubic Ia-3d structure of Ti-MCA was still remained during the preparation of bimetallic catalysts. Furthermore, the peak intensity of bimetallic catalysts was found to be reduced because of decreasing of crystallinity, especially for Ce/Ti-MCA. Regarding to wide-angle diffraction, Figure 4.25(b) showed the crystalline phases of materials. All products exhibited the characteristic peak of the anatase phase at 2θ around 25.3°, 37.8° and 48.0° [51]. It means that the incorporated Ti was also found in the form of anatase. Additionally, the XRD patterns of Ce/Ti-MCA exhibited the high intense characteristic diffraction peaks of CeO_2 at 2θ = 28.5, 33.3, 47.5 and 56.4°. For the Cu/Ti-MCA, XRD pattern showed the diffraction peaks that corresponding to the CuO at 2θ =35.5, 38.7 and 48.5° while low intense characteristic peaks of Fe_2O_3 at 2θ = 33.1, 35.6 was found in the Fe/Ti-MCA diffractogram. These results implied that metallic phase of CeO_2, CuO and Fe_2O_3 are present in the Ce/Ti-MCA, Cu/Ti-MCA and Fe/Ti-MCA catalysts, respectively. However, the XRD pattern of V/Ti-MCA does not show the characteristic diffraction peak of V_xO_y phase. This result indicated that V-species are highly dispersed on the surface of material [13].

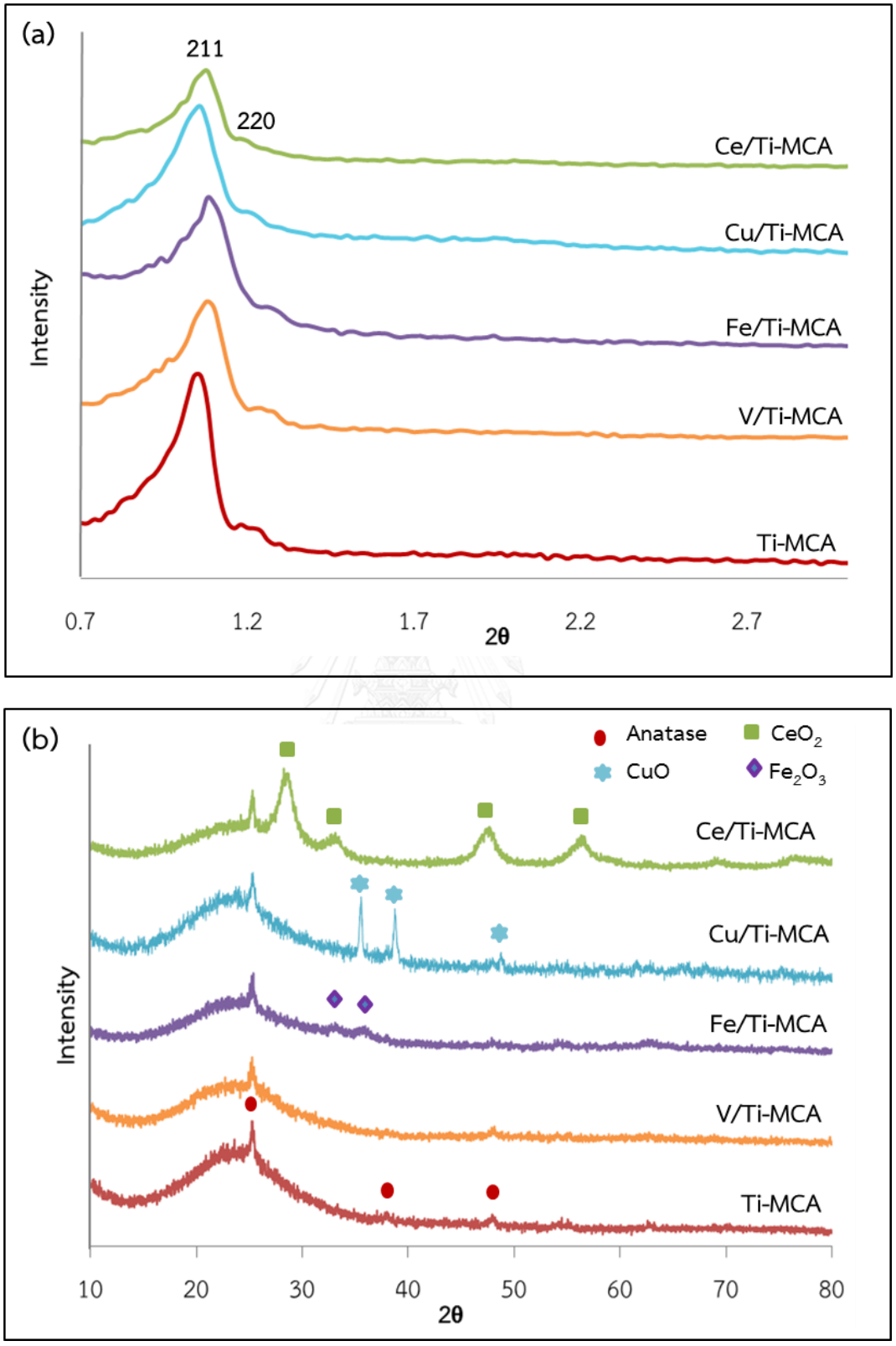

Figure 4.27 X-ray powder diffraction patterns of bimetallic Ti-MCA (M/Ti-MCA) in the range of (a) small-angle and (b) wide-angle.

4.3.1.2 DR-UV results

The DR-UV spectra of bimetallic catalysts were shown in Figure 4.26. All of the samples exhibited an intense band at 210 nm and the shoulder band at 320 nm corresponding to tetrahedrally coordinated titanium and anatase phase, respectively [56]. These results suggested the most of Ti atom in parent material occupy in tetrahedral position and small amount of anatase in the Ti-MCA framework. Moreover, the spectrum of Ce/Ti-MCA sample displayed absorption band at about 300 nm that described as the CeO_2 [57]. In the case of Cu/Ti-MCA, the absorption bands at 210-270 nm not only referred to tetrahedral Ti but also indicated to the Cu ions that occupied isolated sites. Furthermore, the bands over 350 nm indicated the formation of Cu clusters to bulk CuO form [58]. In addition, the Fe/Ti-MCA exhibited the absorption bands at 380, 420, 460, 500 and 540 nm, which can be ascribed to the aggregated Fe_2O_3 clusters [59, 60]. As a result, Ce, Cu and Fe were existed as CeO_2, CuO and Fe_2O_3 particles, respectively. These results were consistent with the XRD data that exhibited the characteristic peak of CeO_2, CuO and Fe_2O_3. Additionally, DR-UV spectra of V/Ti-MCA showed the absorption bands at 210 and 280 nm which can be ascribed to the isolated tetrahedral V^{5+} species [61]. The further bands at 340 and 380 nm indicated the presence of low oligomeric tetrahedral V^{5+} species [61, 62]. The next absorption bands at 420, 460 and 500 nm indicated the presence of octahedral V^{5+} species, bulk V_2O_5 and polymeric vanadium oxide materials, respectively [63, 64]. Comparisons with XRD results, the XRD pattern of V/Ti-MCA does not show the characteristic diffraction peak of bulk V_2O_5 resulting from small amount of bulk V_2O_5.

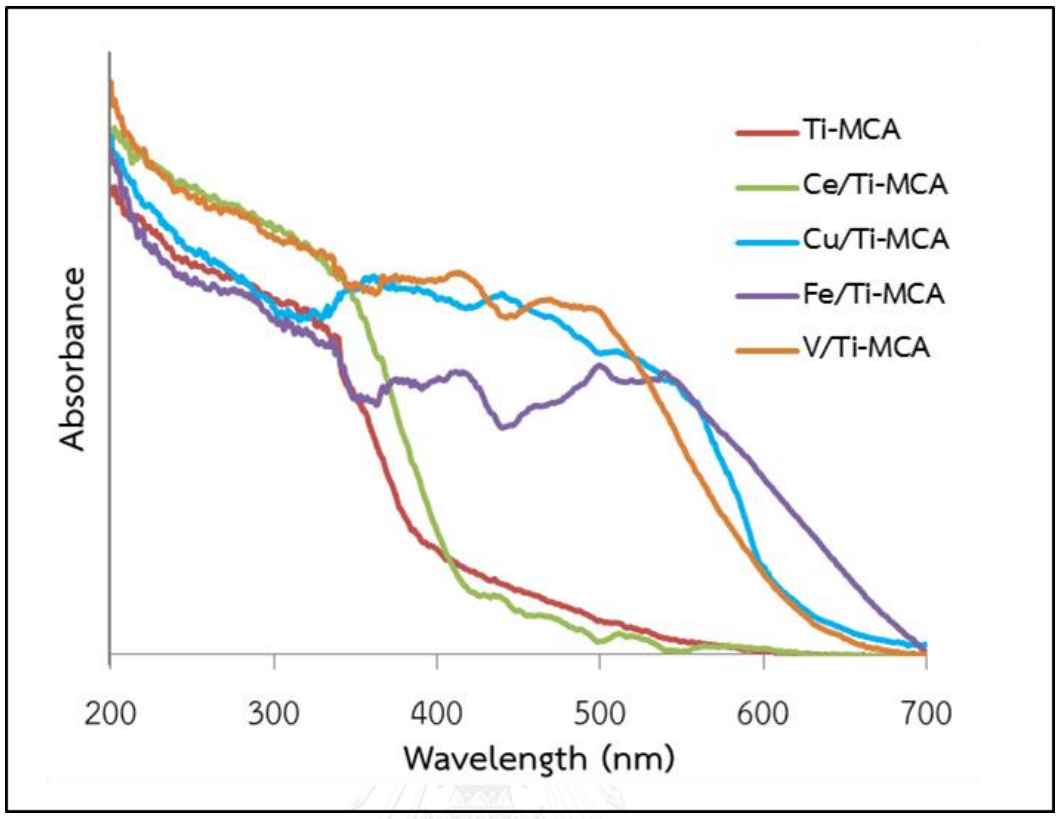

Figure 4.28 DR-UV spectra of M/Ti-MCA.

4.3.1.3 Sorption properties

The nitrogen adsorption/desorption isotherms and pore size distributions of metal supported on Ti-MCA were shown in Figure 4.27. All samples displayed isotherms type IV with a H1 hysteresis loop, which is the characteristic of mesoporous materials [73]. This result indicated that the mesostructure of the materials was preserved after metal impregnation and calcination. For bimetallic catalysts, the sharpness of hysteresis loops was decreased resulting from low uniformity of pore size, as shown in Figure 4.27(b). The metals-modified catalysts exhibited pore size distribution having size around 4.76 nm whereas Ti-MCA showed the narrow pore size distribution centered mostly at 5.41 nm. Furthermore, the surface properties of prepared catalysts are summarized in Table 4.9. The unit cell parameter (a_0) of bimetallic catalysts gave a value in the range of 20.0 - 20.4 nm which is closed to initial material (20.5 nm). The specific surface area and total pore volume of bimetallic catalysts were drastically reduced in comparison with Ti-MCA. This result indicated that the metal oxide particles could be placed in the pores or coating the inner walls of Ti-MCA, which is in accordance with the increase in wall thickness. Bimetallic catalysts showed the thicker wall than Ti-MCA because of the covering of second metals on the pore wall. This result is in good agreement with a study by Macías Esquivel et al. [74]

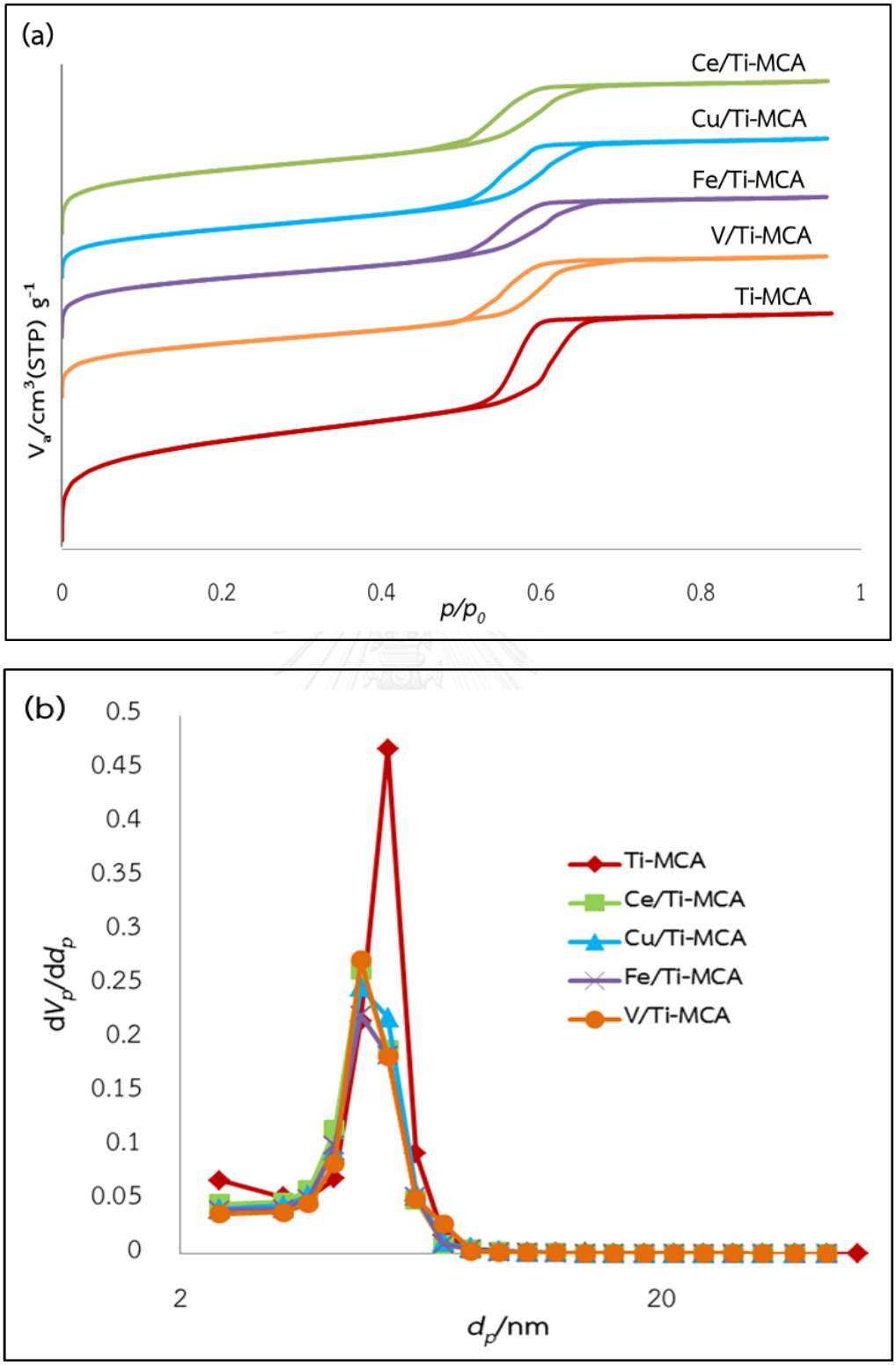

Figure 4.29 (a) N_2 adsorption/desorption isotherms and (b) pore size distributions of bimetallic Ti-MCA.

Table 4.9 Textural properties of metal supported of Ti-MCA materials.

Sample	Si/Ti	a_0 [c]	N_2 Adsorption/desorption			
			Specific surface area (BET)[a] (m^2g^{-1})	Pore volume[b] (cm^3g^{-1})	Pore diameter[b] (nm)	Wall thickness[d] (nm)
Ti-MCA	40	20.5	971	0.7480	5.41	9.1
Ce/Ti-MCA[e]	40	20.0	641	0.5295	4.76	9.4
Cu/Ti-MCA[e]	40	20.4	505	0.5309	4.76	9.7
Fe/Ti-MCA[e]	40	20.0	602	0.4819	4.76	9.4
V/Ti-MCA[e]	40	20.0	554	0.5091	4.76	9.4

[a]BET was calculated by $S_{BET} = S_{total}/a$; S_{BET} = the total surface area, S_{total} = the specific surface area, a = mass of the adsorbent

$S_{total} = (V_mNs)/V$; V_m = units of volume which are also the units of the molar volume of the adsorbate gas, N = Avogadro's number, s = the adsorption cros section of the adsorbing species, V = the molar volume of the adsorbat gas.

[b]reported by BJH plot

[c]cubic unit cell parameter (a_0) = $\sqrt{6} \times d_{211}$; d_{211} = d-spacing data from XRD

[d]wall thickness was calculated by $W = a_0\sqrt{2}/2 - d_p$; W = wall thickness, d_p = pore diameter from BJH plot

[e]Metal content 10wt.%

4.3.1.4 SEM images

The SEM images of metal supported on Ti-MCA are shown in Figure 4.28 (a-e). The particles of Ti-MCA showed stone-like morphology having the size between 2-5 μm. Moreover, the morphology of bimetallic catalysts did not change after metal impregnation and calcination.

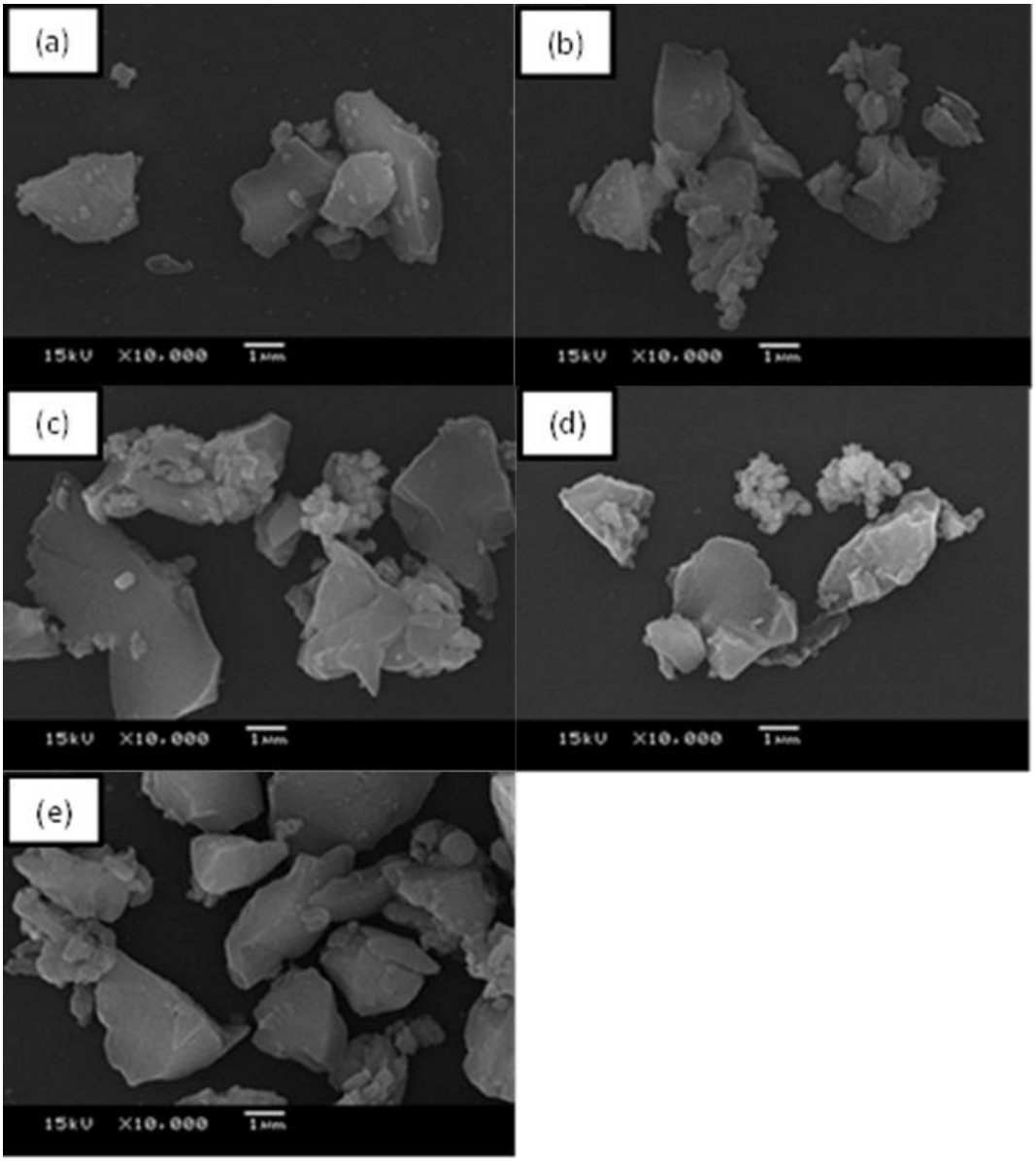

Figure 4.30 The SEM images of (a) Ti-MCA, (b) Ce/Ti-MCA, (c) Cu/Ti-MCA, (d) Fe/Ti-MCA and (e) V/Ti-MCA.

4.3.1.5 TEM images

To further confirm the cubic Ia3d structure of Ti-MCA, transmission electron microscopy (TEM) was evaluated. Figure 4.29 (a-d) showed the TEM images of Ti-MCA taken along the [100], [111], [311] and [110] directions [75]. These images demonstrated that well-ordered cubic Ia3d mesostructure of Ti-MCA was derived. Additionally, the d-spacing and pore size of Ti-MCA at lattice plane [100] are 8.34 nm and 5.24 nm, respectively. These results were in accordance with the value from X-ray diffraction and nitrogen adsorption/desorption data which revealed the d-spacing = 8.36 nm and pore size = 5.41 nm, respectively. It could be confirmed that Ti with three-dimensional cubic Ia3d mesoporous silica was successfully synthesized. The resulting Ti-MCA was utilized for catalyst supporter.

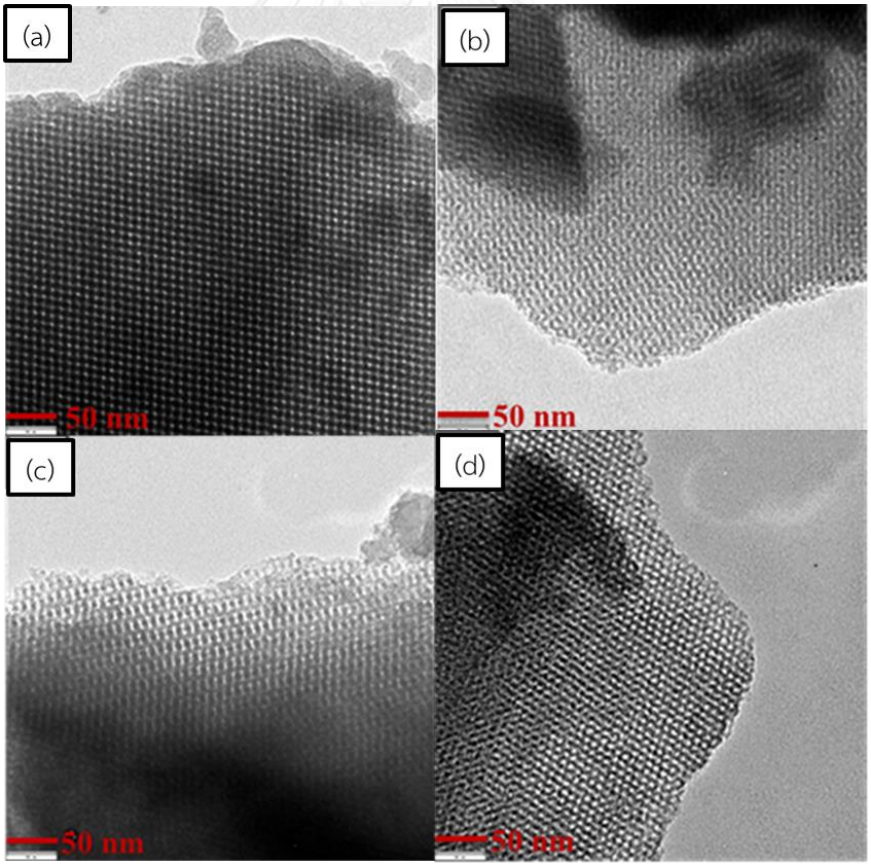

Figure 4.31 TEM images of Ti-MCA taken along the (a) [100], (b) [111], (c) [311] and (d) [110] directions.

TEM images of bimetallic catalysts were depicted in Figure 4.30 (a-d). The images clearly showed that M/Ti-MCA catalysts retained their shape. It indicated that the mesoscopic order of the parent material was maintained after modification. In the case of Ce/Ti-MCA, Cu/Ti-MCA and Fe/Ti-MCA, majority of the metal particles were present on the outer pore. For Ce/Ti-MCA and Cu/Ti-MCA, metal particles dispersion of both catalysts consisted of two types of particle. One is a small metallic particle with mean dimensions around 5 × 5 nm and 8 ×11 nm for Ce/Ti-MCA and Cu/Ti-MCA, respectively. Another is an aggregated particle. Some portions of metal particles were agglomerated having size 29 × 39 nm and 15 ×18 nm for Ce/Ti-MCA and Cu/Ti-MCA, recpectively. In addition, TEM image of Fe/Ti-MCA presented the agglomeration of Fe particles with size in the range 41 - 83 nm. On the other hand, the metal dispersion on TEM image of V/Ti-MCA cannot be clearly observed because vanadium with low atomic number did not generate much contrast. As a result, TEM image of V/Ti-MCA showed the small light particles. These results substantiated that the second metal was located on Ti-MCA which were in accordance with the XRD and DR-UV data.

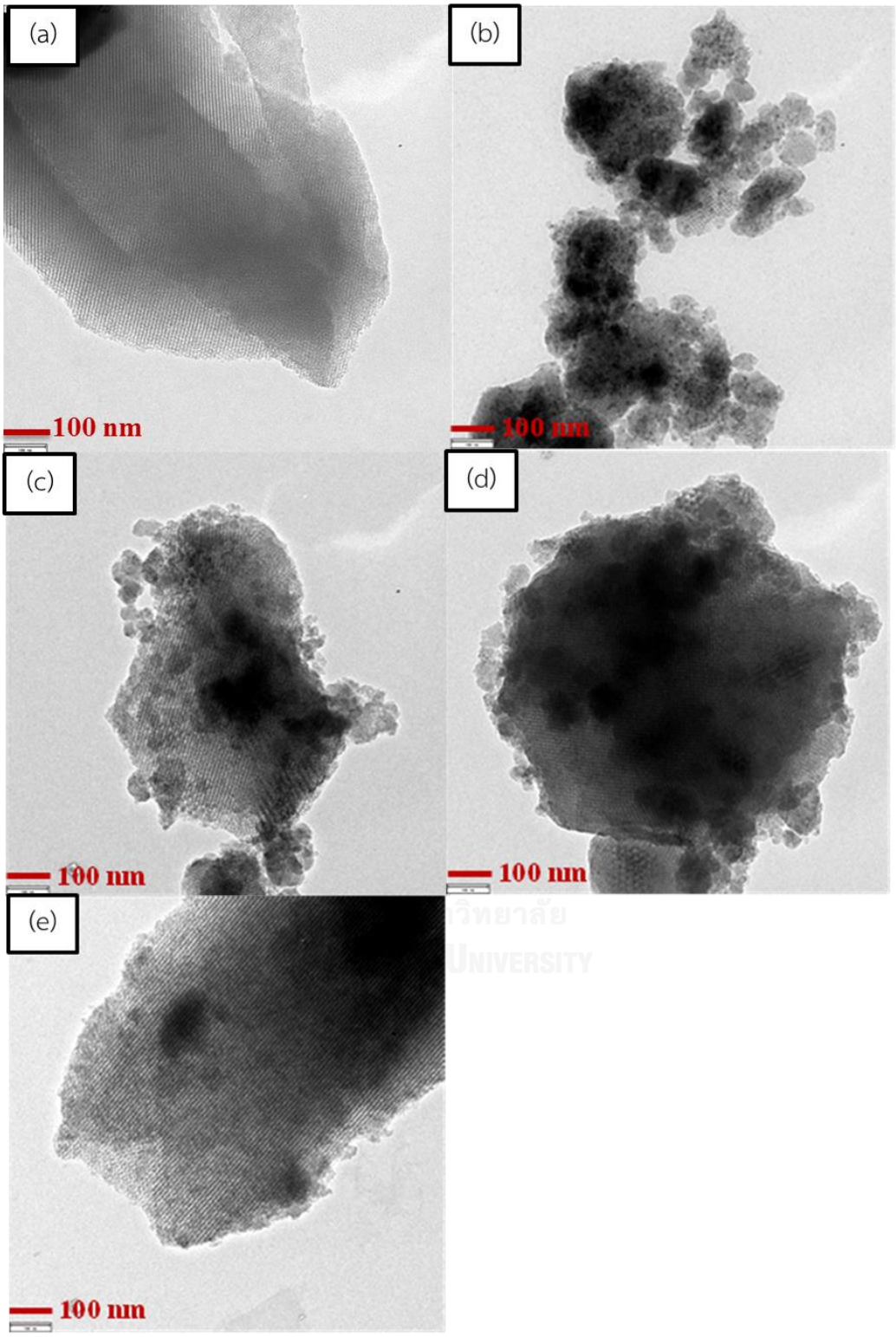

Figure 4.32 TEM images of (a) Ti-MCA, (b) Ce/Ti-MCA, (c) Cu/Ti-MCA, (d) Fe/Ti-MCA and (e) V/Ti-MCA.

4.3.2. Effect of vanadium content (V/Ti-MCA)

4.3.2.1 XRD results

Small-angle X-ray diffraction patterns of V/Ti-MCA with different V-contents are shown in Figure 4.31 (a). The 211 and 220 reflections were clearly observed in the XRD patterns of all catalysts. This result indicated that the cubic Ia-3d structure of Ti-MCA was maintained after modification. However, the intensity of diffraction peak was dramatically decreased with increasing the amount of V loading due to the reduction in crystallinity. The wide-angle X-ray diffraction patterns are also shown in Figure 4.31(b). At lower V loading (5-10 wt.%), a similar XRD profile as parent Ti-MCA was presented and no observed characteristic reflections of V_2O_5 phase. This result implied that the V species were highly dispersed on the surface of Ti-MCA. At the higher V loading (15 wt.%), the characteristic reflection peaks of V_2O_5 were observed at 2θ = 15.3, 20.27, 26.21, 31.05, 34.3, 41.3 and 51.2° [55, 63]. The intensity of V_2O_5 phase was increased when increasing the concentration of vanadium to 20 wt.%, which demonstrated a decrease in V dispersion.

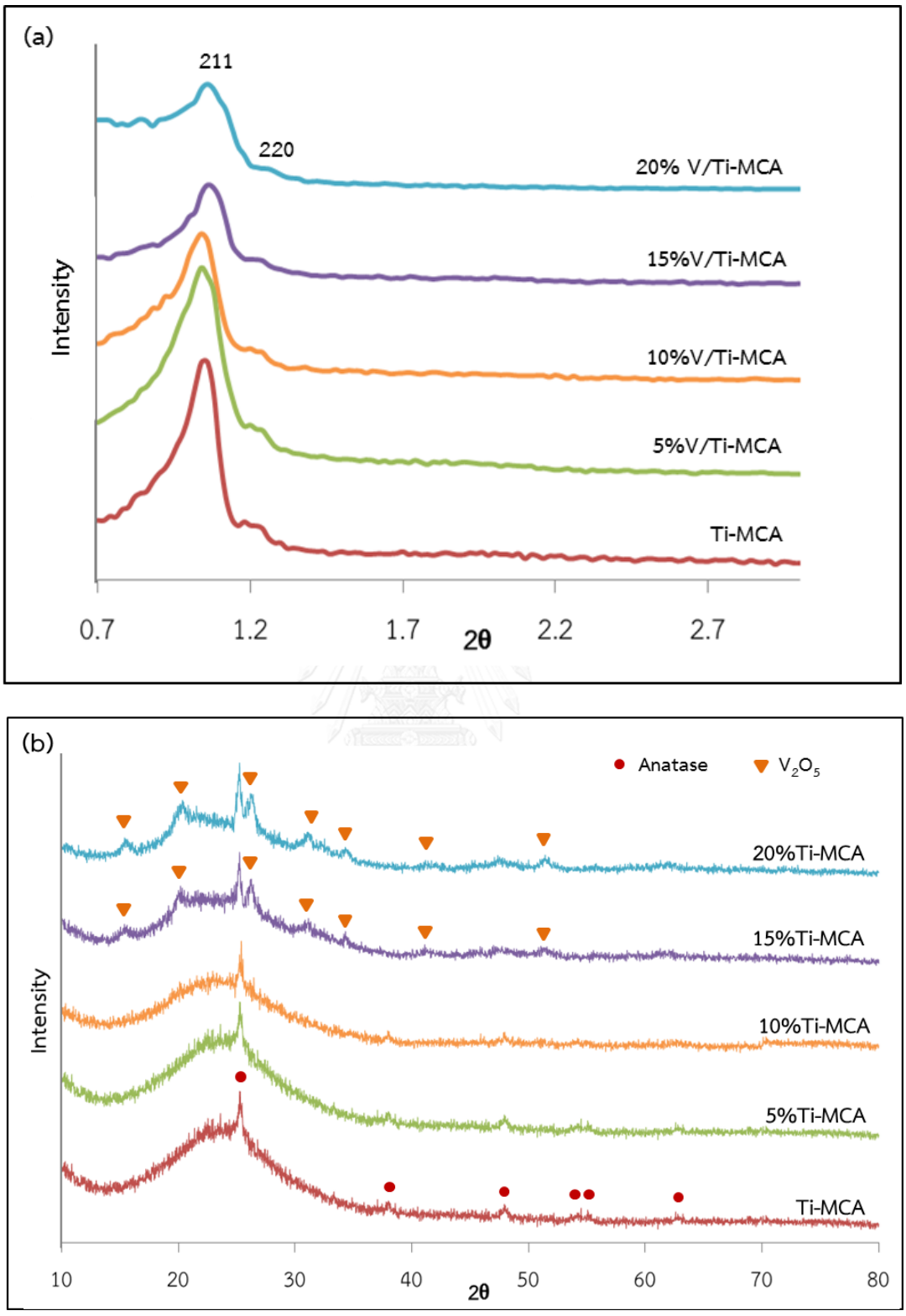

Figure 4.33 X-ray powder diffraction patterns of V/Ti-MCA with different V-contents in the range of (a) small-angle and (b) wide-angle.

4.3.2.2 DR-UV results

The diffuse reflectance UV spectra of V/Ti-MCA with different V-contents are shown in Figure 4.32. The strong absorption peak at 210 nm, assigned to tetrahedrally coordinated titanium, was found for all materials. At lower V loading (5 wt.% V/Ti-MCA), two absorption bands at around 280 and 340 nm was observed. These band can be ascribed to the isolated tetrahedral V^{5+} of VO_4 species and the low oligomeric tetrahedral coordinated V^{5+} species, respectively [61, 62]. Moreover, the DR-UV spectra of 5 wt.% V/Ti-MCA displayed a shoulder bands at about 380, 420, 460 and 500 nm, which can be ascribed to the low oligomeric tetrahedral coordinated V^{5+} species, octahedral V^{5+} species, bulk V_2O_5 and polymeric vanadium oxide materials, respectively [62-64]. As the vanadium content increase, the intensity of the absorption peaks at around 340, 380, 420, 460 and 500 nm increased significantly while the intensity of the absorption peaks at 280 nm was found to be reduce, except for 10 wt.% V/Ti-MCA. These results substantiated that some isolated V species aggregated and changed to be bulk V species with increasing V-content. The DR-UV spectra of V/Ti-MCA with 15 and 20 wt.% showed the broad absorption peaks and high intensity at 460 and 500 nm, which indicated that more bulk V_2O_5 was formed. Thus, the species of V are strongly depended on V-content. These results are in accordant with XRD data.

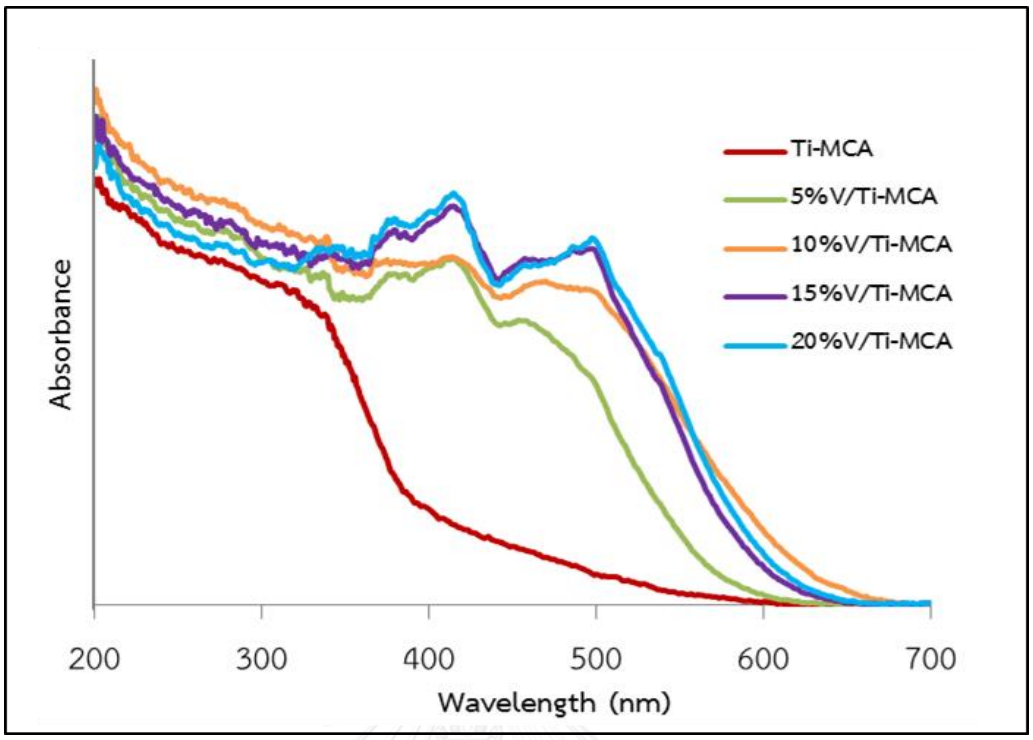

Figure 4.34 DR-UV spectra of V/Ti-MCA with different V-contents.

4.3.2.3 Sorption properties

The nitrogen adsorption/desorption isotherms and pore size distributions of V/Ti-MCA with various amount of V loading were shown in Figure 4.33. It is clear that the N_2 adsorption/desorption isotherms of all catalysts exhibited type IV with a typical H1 hysteresis loop, which is the characteristic of mesoporous materials. The result indicated that the mesoscopic order of Ti-MCA support was maintained after modified by various content of vanadium. In addition, the hysteresis loop became flat and smaller than parent material with increasing the amount of V loading, resulting from a decrease in pore volume after the increase of vanadium concentration. The surface properties of the samples are summarized in Table 4.10. The surface area of the catalyst decreased from 971 to 365 m^2g^{-1} when the V-content increased from 0 to 20 wt.%. In the case of V/Ti-MCA with 5 and 10 wt.% of V, The specific surface area, total pore volume and pore diameter of samples were decreased, accompanied with the increased in wall thickness. These results suggested that the V species could be placed in the pores or coating the inner walls of Ti-MCA. With increasing V-content, the unchangeable in its pore diameter with drastically decrease in the pore volume and surface area observed for 15 and 20 wt.% V/Ti-MCA because the partial pores were blocked by the bulk vanadium oxide species.

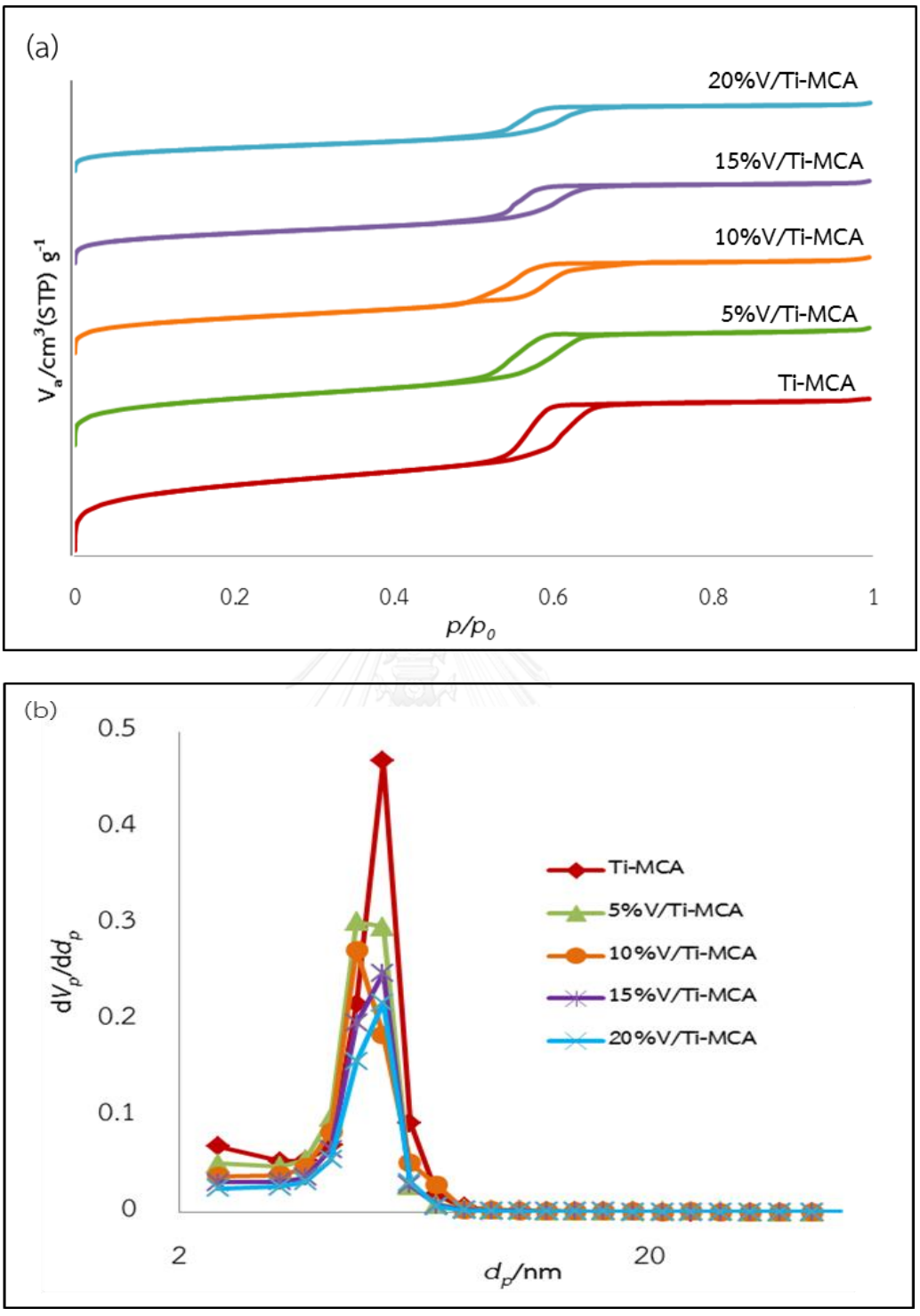

Figure 4.35 (a) N_2 adsorption/desorption isotherms and (b) pore size distributions of V/Ti-MCA with different V-contents.

Table 4.10 Surface properties of V/Ti-MCA with different V-content.

Sample	Metal content (wt.%)	a_0 [c]	N_2 Adsorption/desorption			
			Specific surface area (BET)[a] ($m^2 g^{-1}$)	Pore volume[b] ($cm^3 g^{-1}$)	Pore diameter[b] (nm)	Wall thickness[d] (nm)
Ti-MCA[e]	0	20.5	971	0.7480	5.41	9.1
V/Ti-MCA[e]	5	20.0	712	0.6090	4.76	9.4
	10	20.0	554	0.5091	4.76	9.4
	15	20.2	453	0.4521	5.41	8.9
	20	20.3	365	0.3854	5.41	8.9

[a]BET was calculated by $S_{BET} = S_{total}/a$; S_{BET} = the total surface area, S_{total} = the specific surface area, a = mass of the adsorbent

$S_{total} = (V_m N s)/V$; V_m = units of volume which are also the units of the molar volume of the adsorbate gas, N = Avogadro's number, s = the adsorption cros section of the adsorbing species, V = the molar volume of the adsorbat gas.

[b]reported by BJH plot

[c]cubic unit cell parameter ($\mathbf{a_0}$) = $\sqrt{6} \times \mathbf{d_{211}}$; d_{211} = d-spacing data from XRD

[d]wall thickness was calculated by $W = \mathbf{a_0}\sqrt{2}/2 - d_p$; W= wall thickness, d_p= pore diameter from BJH plot

[e]Si/Ti = 40

4.3.2.4 SEM images

The SEM images of V/Ti-MCA with different V-content are illustrated in Figure 4.34. From the result, the micrograph of V/Ti-MCA with different amount of vanadium loading still retained stone-like morphology having the size between 2-5 μm, which similar to Ti-MCA parent material. This result substantiated that the morphology of catalysts did not change after increasing the vanadium concentration.

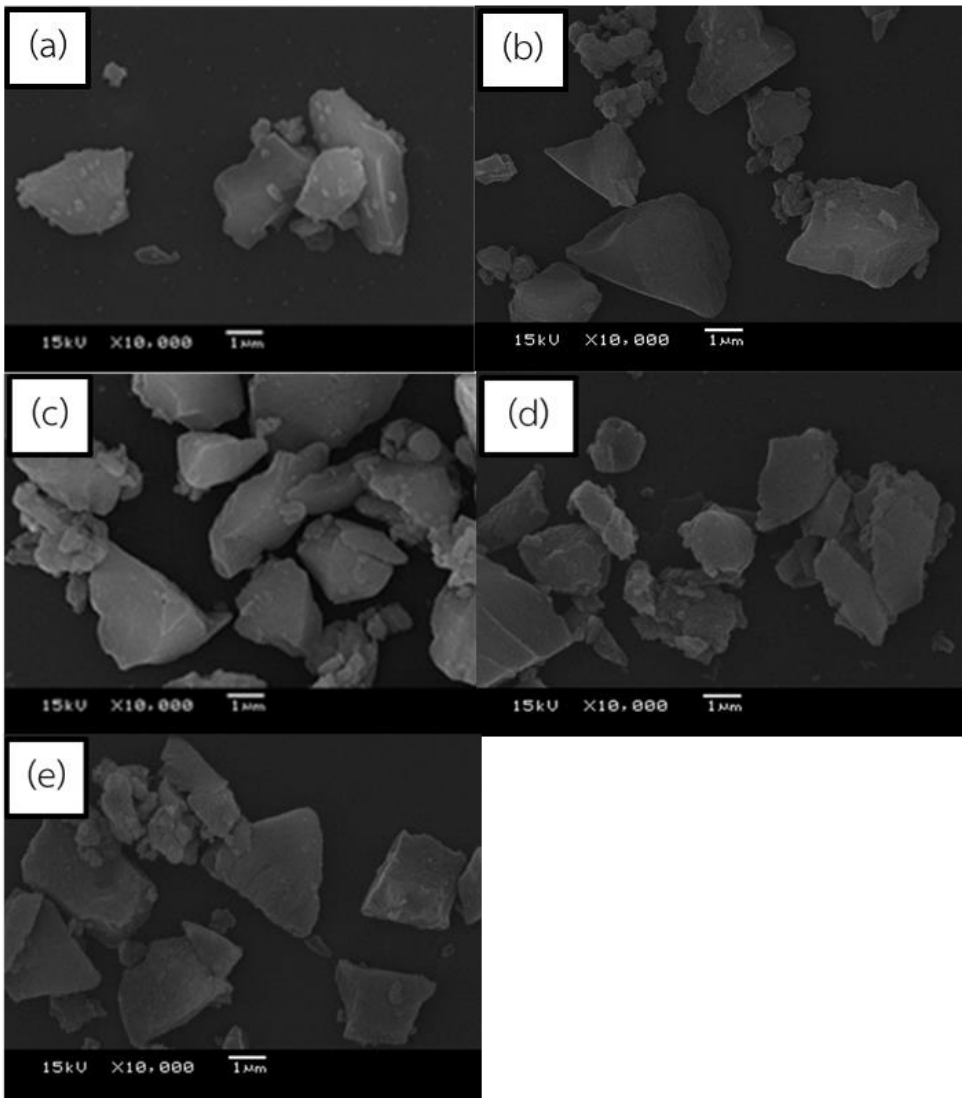

Figure 4.36 The SEM images of V/Ti-MCA with different V-content; (a) Ti-MCA, (b)5wt.% V/Ti-MCA, (c)10wt.% V/Ti-MCA, (d) 15wt.% V/Ti-MCA and (e)20wt.% V/Ti-MCA.

4.3.2.5 TEM images

TEM micrographs of V/Ti-MCA with various amount of V loading were depicted in Figure 4.35. In the case of V/Ti-MCA with 5 and 10 wt.% of V loading, TEM images showed the pleasing dispersion on the Ti-MCA surface with small metallic particles. However, some portions of metal particles were agglomerated having size 11.7-58.8 nm and 11.7-70.6 nm for 5 and 10 wt.% V/Ti-MCA, respectively. With the increase of V loading, TEM images of V/Ti-MCA with 15 wt.% of V loading exhibited the agglomeration of V metallic particles in irregular form with size in the range 35.3-117.6 nm and the size were larger to 35.3-211.8 nm when V loading up to 20 wt.%. These results indicated a strong aggregation of V species with increasing the amount of loaded V, which were in accordance with the XRD and DR-UV spectra.

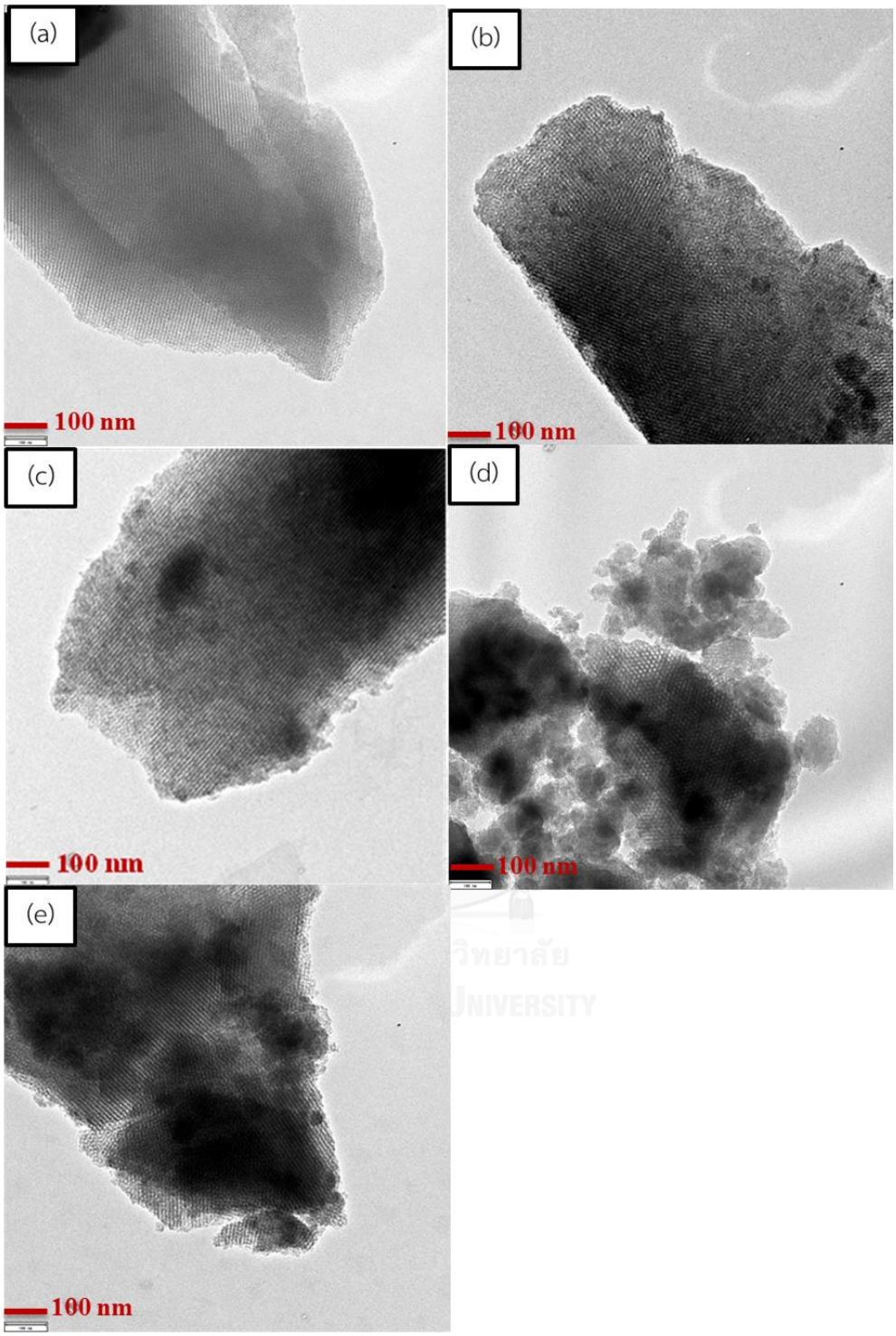

Figure 4.37 TEM images of V/Ti-MCA with different V-content; (a) TS-1, (b) 5wt.% V/TS-1, (c) 10wt.% V/TS-1, (d) 15wt.% V/TS-1 and (e) 20wt.% V/Ti-MCA.

4.3.2.6 ICP-MS results

The content of metals was determined by using Inductively Coupled Plasma Mass Spectrometer (ICP-MS). The elemental analysis data of V/Ti-MCA with different V-content are shown in Table 4.11. The ICP-MS analysis showed a higher deviation of Si/Ti mole ratio than the amount of metal in solution loading (Si/Ti mole ratio = 40) due to remaining Ti in the synthetic gel. Moreover, the amount of vanadium was closed to stoichiometric adding values as 4.75, 9.18, 14.13 and 19.10 wt.% for 5, 10, 15 and 20 wt.% of V/Ti-MCA, respectively.

Table 4.11 Metal content analysis of V/Ti-MCA with different V-content.

Catalyst	Si/Ti mole ratio[a]	V-content (wt.%)[a]
Ti-MCA	66	-
5wt.%V/Ti-MCA	63	4.75
10wt.%V/Ti-MCA	63	9.18
15wt.%V/Ti-MCA	62	14.13
20wt.%V/Ti-MCA	62	19.10

[a]Inductively Coupled Plasma Mass Spectrometry (ICP-MS)

4.4 The physico-chemical properties of bimetallic Ti-SBA-15

4.4.1 Effect of second metal (M/Ti-SBA-15)

4.4.1.1 XRD results

XRD patterns of the synthesized SBA-15 and bimetallic Ti-SBA-15 are shown in Figure 4.36. Pure SBA-15 exhibited XRD pattern with one very intense diffraction peak at around 2θ = 0.9 and two weak peaks at 2θ = 1.5 and 1.8 that corresponded to 100, 110 and 200 reflections, respectively. This refers to the characteristic peak of 2D hexagonal structure. Moreover, XRD spectrum of Ti-SBA-15 was shifted to higher angles and showed a lower intensity when compared with pure SBA-15 spectrum. Because the titanium incorporation into the structure, which was consistent with previous researches [49]. After impregnation of second metal, M/Ti-SBA-15 spectra were similar as Ti-SBA-15 spectrum, indicating the preserved ordering of SBA-15 structure. However, a decrease in the intensity and broadening of the XRD spectrum suggests an irregular organization of order in the SBA-15 structure. Regarding to wide-angle diffraction, Figure 4.36(b) show the crystal structure of metallic phase. The XRD pattern of Ce/Ti-SBA-15 exhibited the diffraction peaks at 28.5, 33.3, 47.5 and 56.4° corresponding to characteristic peak of CeO_2. This observation is similar to the results published by Zhen et al [52]. These results substantiated that crystallites and amorphous phase of CeO_2 are present in the sample. In the case of Cu/Ti-SBA-15, characteristic diffraction peaks of CuO at 2θ = 32.3, 35.4, 38.5, 48.5, 53.1, 57.9, 61.1, 67.5 and 75.5° were observed [53]. It means that the Cu on the Ti-MCA support existed as CuO particles. For the Fe/Ti-SBA-15 catalyst, the iron crystalline phase was detected in the Fe_2O_3 form and showed characteristic peak at 2θ = 35.6° [54]. In the case of V/Ti-SBA-15, the XRD pattern of the sample does not show the characteristic diffraction peak of V_xO_y. This result

indicates that vanadium is well-dispersed on the surface of material or the concentrations of the V_2O_5 are below the level that can be detected.

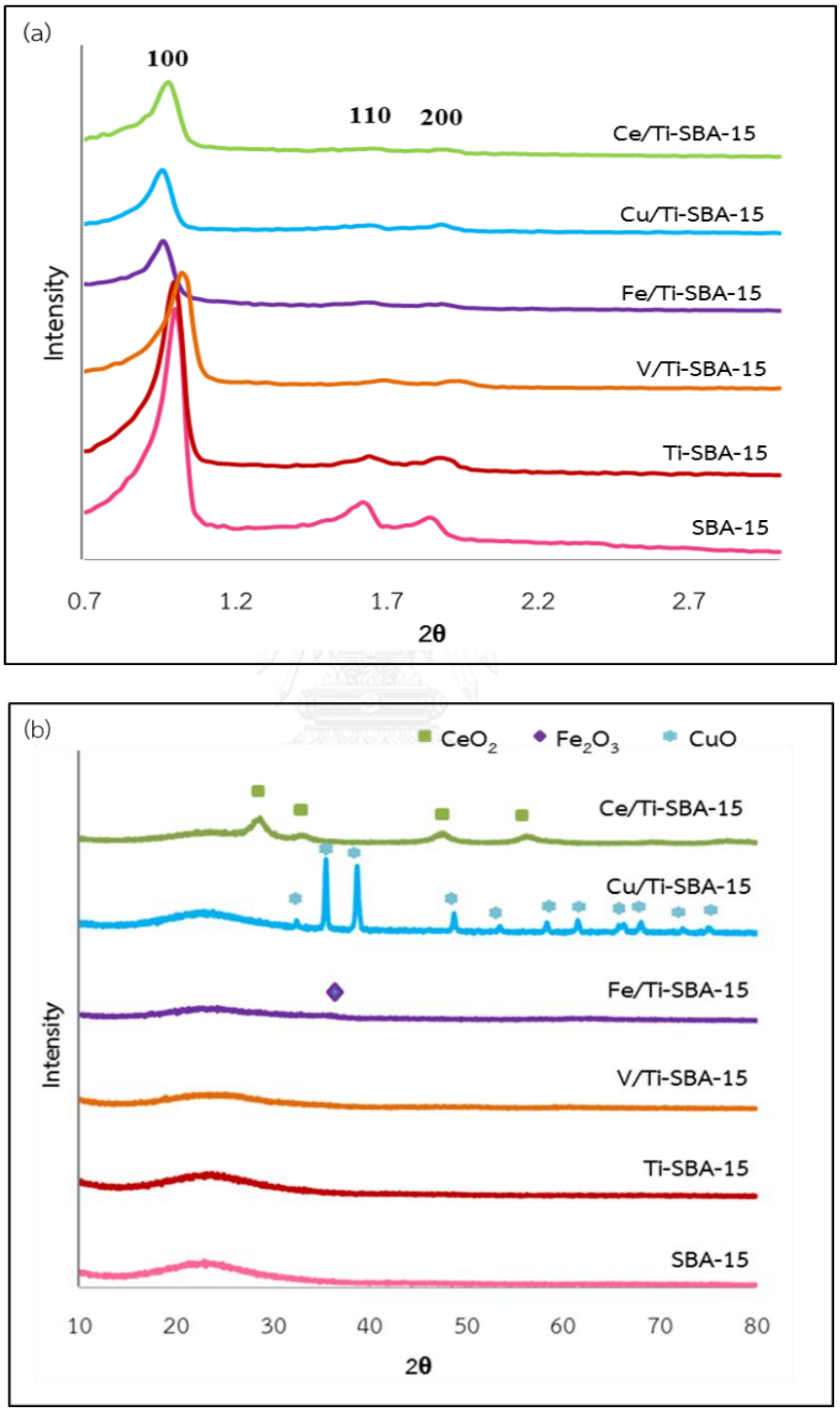

Figure 4.38 X-ray powder diffraction patterns of SBA-15 and bimetallic Ti-SBA-15 in the range of (a) small-angle and (b) wide-angle.

4.4.1.2 DR-UV results

The DR-UV spectra of bimetallic Ti-SBA-15 were shown in Figure 4.37. The spectrum of pure SBA-15 was also included for comparison purpose. From the results, pure SBA-15 had no characteristic absorption peak while the Ti-SBA-15 exhibited an intense band at 210 nm and the shoulder band at 320 nm. The band at 210 nm is a characteristic band of tetrahedrally coordinated titanium and the band at 320 nm related to anatase phase in the framework. On the other hand, the absence of an absorption band at ≈ 270 nm was indicated the no observe of octahedral coordination. That suggested the most of Ti atom occupy in tetrahedral position and small amount of anatase in the framework of Ti-SBA-15 [76]. After impregnation of second metal, the absorption peak at 210 nm was observed in all the samples. This peak is attributed to the regular $Ti^{4+}O_4$ framework tetrahedral of parent material. Furthermore, the spectra of Ce/Ti-SBA-15 sample displayed the absorption peak at about 340 nm. This peak can be ascribed to the small CeO_2 crystallites [57]. Moreover, DR-UV spectra of Cu/Ti-SBA-15 exhibited the absorption band at 210-270 nm. This band can be ascribed to the Cu ions that occupied isolated sites. In addition, the band over 350 nm indicated the formation of Cu clusters to bulk CuO [58]. For the Fe/Ti-SBA-15 catalyst, different Fe^{3+} species in the sample have been characterized by the peak position, such as Fe in octahedral position at 280 nm, small clusters or microaggregates of Fe_2O_3 particles located between 300-400 nm and aggregated Fe_2O_3 cluster at 420-500 nm [59, 60]. In addition, DR-UV spectra of V/Ti-SBA-15 showed the absorption peaks at 280, 380, 420, 460 and 500 nm. The features located at 280 and 380 nm have been attributed to the isolated tetrahedral V^{5+} species and the low oligomeric tetrahedral coordinated V^{5+} species, respectively [61, 62]. The other absorption peaks at 420, 460 and 500 nm can be assigned to the octahedral V^{5+} species, bulk V_2O_5 and polymeric

vanadium oxide materials, respectively [63, 64]. From the result, the UV spectra confirm the presence of metal species in the synthesized samples.

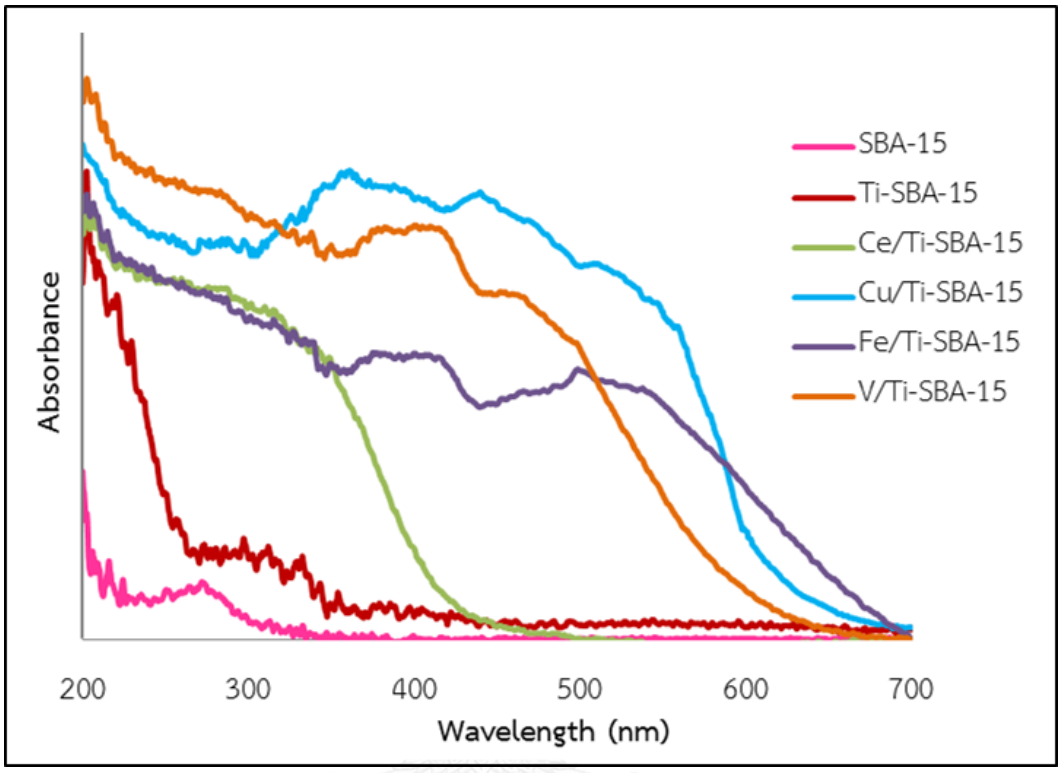

Figure 4.39 DR-UV spectra of bimetallic Ti-SBA-15.

4.4.1.3 Sorption properties

The nitrogen adsorption/desorption isotherms and pore size distributions of SBA-15 and bimetallic Ti-SBA-15 were shown in Figure 4.38. Both products displayed a type IV isotherm with H1-type hysteresis loop according to the IUPAC classification for mesoporous materials [49]. This suggested that the incorporation of titanium species of Ti-SBA-15 retained the typical mesoporous structure of SBA-15. The hysteresis loop of Ti-SBA-15 slightly shifted to lower relative pressure when compared with SBA-15 revealed that the pore size of Ti-SBA-15 was smaller than SBA-15 as mentioned in Table 4.12. After impregnation of second metal, the nitrogen adsorption/desorption isotherms were similar to the original Ti-SBA-15 suggesting that the mesoporous structure of the materials were preserved upon metal impregnation and calcination. However, it is easy to observe that the hysteresis loop of Ce/Ti-SBA-15 becomes broader than those of other M-Ti-SBA-15. From the result, the desorption branch of the M-SBA-15 isotherms shifted to lower pressure, whereas the adsorption was not changed. This behavior indicated that the coexistence of open and partially closed mesopores which suggested by Janssen [77]. Furthermore, the narrow pore size distribution curves were shown in Figure 4.38(b). The results indicated the uniformity of the mesopore size for all samples with average pore size about 10.5 and 7.0 nm for SBA-15 and bimetallic Ti-SBA-15, respectively.

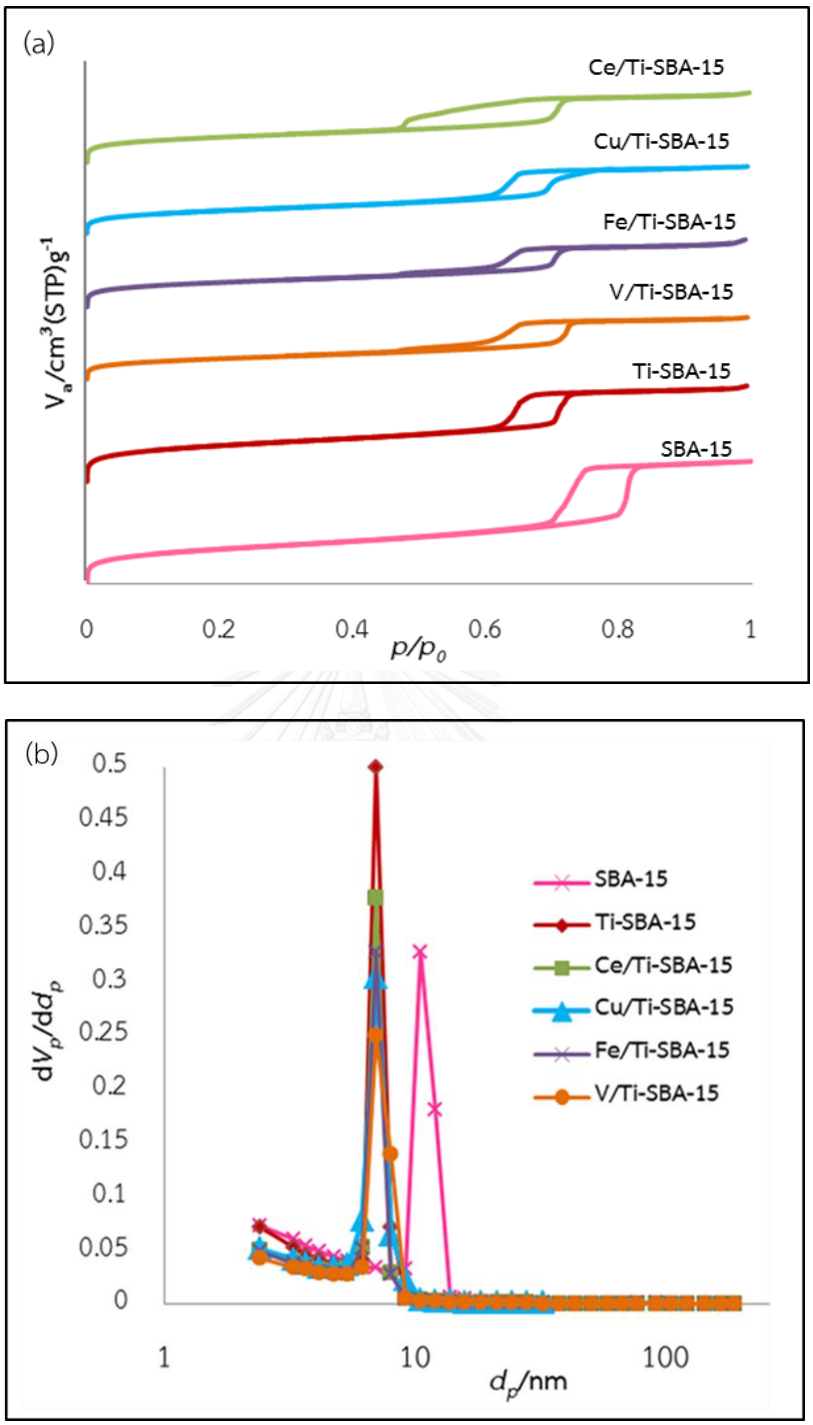

Figure 4.40 (a) N_2 adsorption/desorption isotherms and (b) pore size distributions of M/Ti-SBA-15.

The surface properties of SBA-15, Ti-SBA-15 and bimetallic Ti-SBA-15 were summarized in Table 4.12. The incorporation of titanium species caused a decrease of pore volume and pore diameter when compared with pure SBA-15 due

to the larger diameter of titanium atom than silicon atom [78]. The surface area and pore volume of the Ti-SBA-15 support was 891 $m^2 g^{-1}$ and ca. 0.8703 $cm^3 g^{-1}$, respectively. Following impregnation of second metal, the drastic reduction in surface area and total pore volume indicated that parts of the metal oxide particles were deposited in the pores of the support which leading to a partial blockage due to agglomerate formation. Thus, the loss of surface area and pore volume of bimetallic catalyst in comparison with Ti-SBA-15 confirm the attachment of metals inside the pores.

Table 4.12 Surface properties of metal containing Ti-SBA-15 (M/Ti-SBA-15).

Sample	a_0[c]	N_2 Adsorption/desorption			
		Specific surface area (BET)[a] ($m^2 g^{-1}$)	Pore volume[b] ($cm^3 g^{-1}$)	Pore diameter[b] (nm)	Wall thickness[d] (nm)
SBA-15	10.7	852	1.1862	10.57	0.1066
Ti-SBA-15	10.4	891	0.8703	7.05	3.3585
Ce/Ti-SBA-15[e]	10.4	663	0.6444	7.05	3.3899
Cu/Ti-SBA-15[e]	10.6	617	0.6395	7.05	3.5721
Fe/Ti-SBA-15[e]	10.6	646	0.6201	7.05	3.5995
V/Ti-SBA-15[e]	10.0	548	0.5973	7.05	2.9545

[a]BET was calculated by $S_{BET} = S_{total}/a$; S_{BET} = the total surface area, S_{total} = the specific surface area, a = mass of the adsorbent

$S_{total} = (V_m N s)/V$; V_m = units of volume which are also the units of the molar volume of the adsorbate gas, N = Avogadro's number, s = the adsorption cros section of the adsorbing species, V = the molar volume of the adsorbat gas.

[b]reported by BJH plot

[c]unit cell parameter ($\mathbf{a_0}$) = $\mathbf{2d_{100}/\sqrt{3}}$; d_{100} = d-spacing data from XRD

[d]wall thickness was calculated by $W = \mathbf{a_0} - d_p$; W = wall thickness,

d_p = pore diameter from BJH plot

[e]Metal content 10wt.%.

4.4.1.4 SEM imges

The SEM images of the synthesized SBA-15 and bimetallic Ti-SBA-15 are shown in Figure 4.39. The micrograph of Ti-SBA-15 shows that the cylindrical grain shape particles having the size of about 630 x 970 nm, which are commonly observed in pure SBA-15. Furthermore, the morphologies of Ti-SBA-15 were slightly changed after metal impregnation. The particle shapes of M/Ti-SBA-15 were smaller than pure Ti-SBA-15. The particles size of Ce/Ti-SBA-15, Cu/Ti-SBA-15, Fe/Ti-SBA-15 and V/Ti-SBA-15 were *ca*. 400 × 600 nm, 500 × 600 nm, 600 × 600 nm and 600 × 800 nm, respectively.

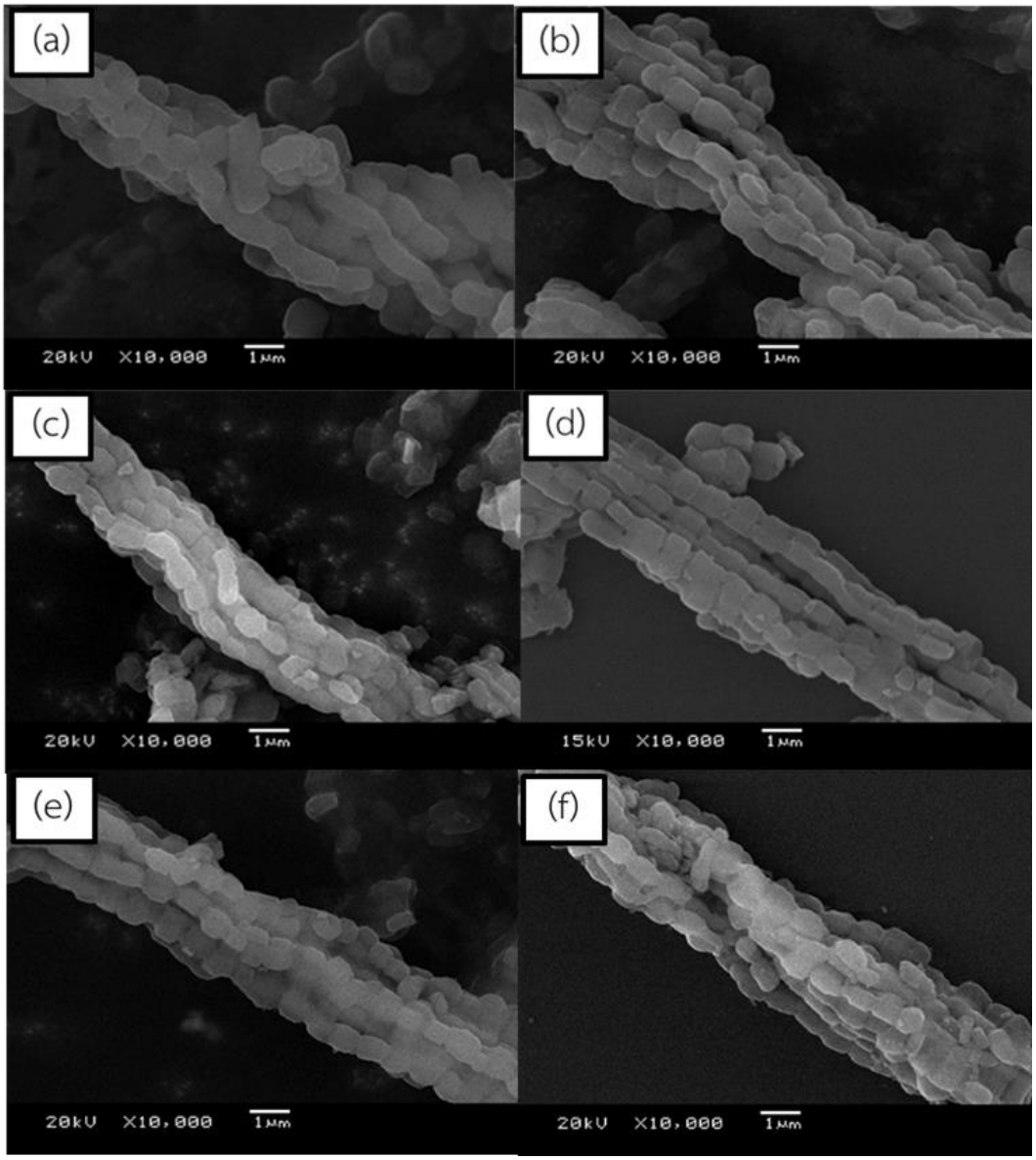

Figure 4.39 The SEM images of (a) SBA-15, (b) Ti-SBA-15, (c) Ce/Ti-SBA-15, (d) Cu/Ti-SBA-15, (e) Fe/Ti-SBA-15 and (f) V/Ti-SBA-15.

4.4.1.5 TEM images

Transmission electron micrographs of the Ti-SBA-15 in Figure 4.40 (a-b) showed the two-dimensional hexagonal texture of SBA-15 and the distance between two adjacent SBA-15 mesopore ~7.1 nm. These results consisted with the estimation by nitrogen adsorption/desorption isotherm, which presented in Table 4.12. Following impregnation with second metal, the M/Ti-SBA-15 catalysts retained its shape, which indicated that the mesoscopic order of the parent materials was maintained. In the case of Ce/Ti-SBA-15, the metal particles were well dispersed on the surface of support material. However, particles size of CeO_2 clusters were found to be in the 75 × 75 nm. For Cu/Ti-SBA-15, the aggregated metal particles of CuO were found with size in the range 50-500 nm. In addition, on the surface of Fe/Ti-SBA-15, the TEM images presented the agglomeration of Fe particles in the mean size about 83 × 83 nm and the large size about 100 × 183 nm. This result indicated that aggregate Fe particles were mainly presented on the outer pore because the metallic particle size larger than pore size of SBA-15. On the other hand, the TEM images of V/Ti-SBA-15 were showed the small metallic particle in size about 7 × 7 nm. These results were in accordance with the XRD and DR-UV spectra, which presented the phase of an aggregation of Ce, Cu and Fe in the form of CeO_2, CuO and Fe_2O_3, respectively.

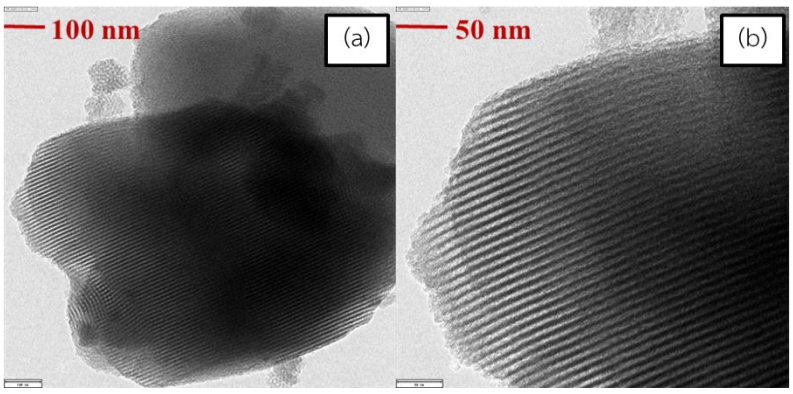

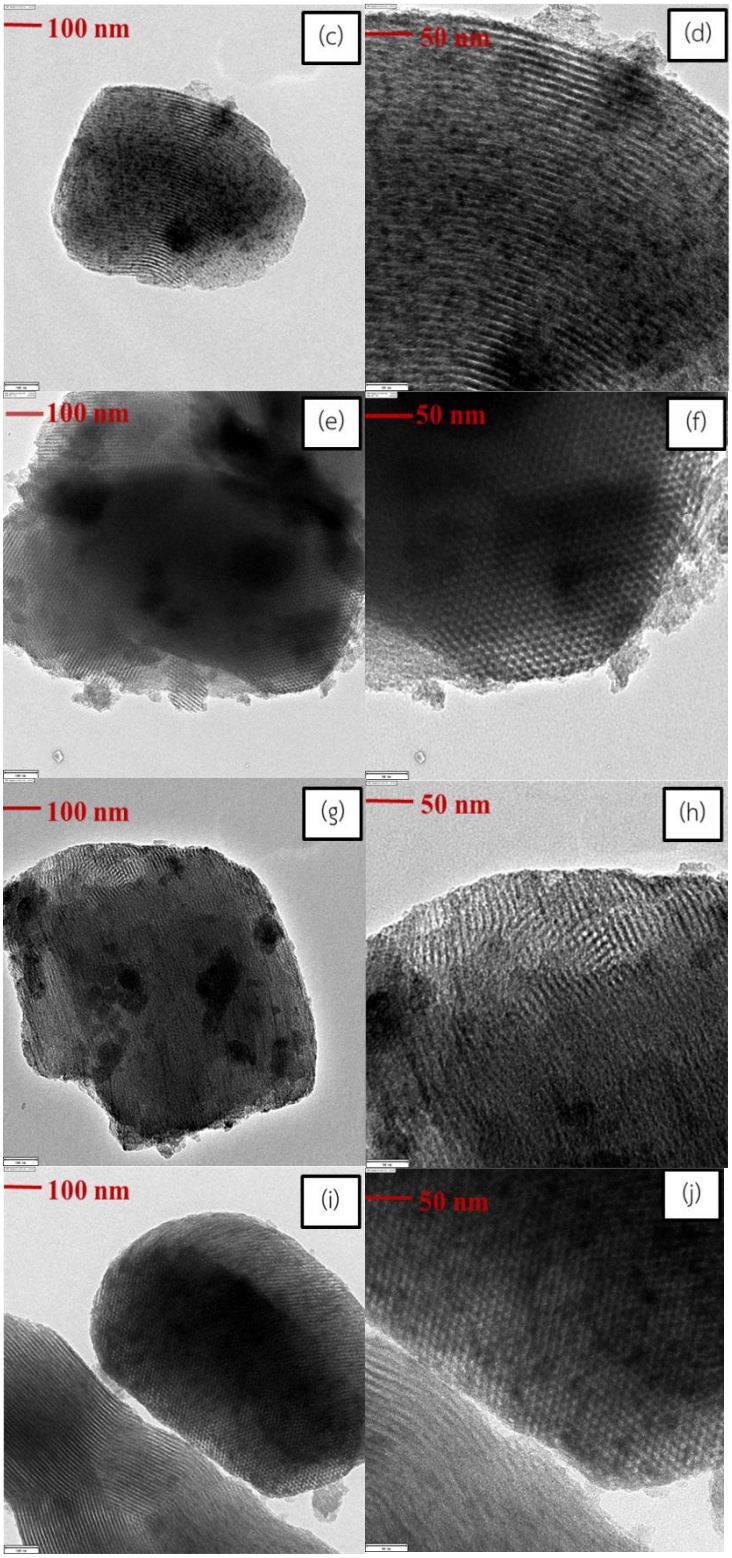

Figure 4.41 TEM images of (a-b) Ti-SBA-15, (c-d) Ce/Ti-SBA-15, (e-f) Cu/Ti-SBA-15, (g-h) Fe/Ti-SBA-15 and (i-j) V/Ti-SBA-15 at 20000 and 50000 magnifications.

4.5 Catalytic testing

The synthesized catalysts were used in benzene hydroxylation with H_2O_2 as the oxidant. The influence of the various reaction parameters including mole ratio of benzene and hydrogen peroxide, type of transition metal, the amount of catalyst, reaction time, reaction temperature, metal contents, Si/Ti mole ratio and type of solvent were investigated. The results were presented in Table 4.13 to 4.40.

4.5.1 Catalytic testing of M/TS-1 on benzene hydroxylation

4.5.1.1 Effect of benzene to hydrogen peroxide mole ratio for TS-1

Table 4.13 illustrated the influence of mole ratio of benzene to hydrogen peroxide over TS-1 support. The yield of phenol was positively depended on the amount of H_2O_2 and reached a maximum value of 0.88% at the benzene to hydrogen peroxide mole ratio as 1:7. With a further increase in the mole ratio of benzene to hydrogen peroxide, the yield of phenol was still constant. Therefore, the suitable mole ratio of benzene to hydrogen peroxide for the yield of phenol was 1:7.

Table 4.13 Effect of benzene: H_2O_2 mole ratio on the catalytic performance of TS-1.

Catalyst	Mole ratio of Benzene:H_2O_2 (in total volume /g)	% yield by mole				H_2O_2 efficiency
		Phenol	Hydro quinone	Benzo quinone	Catechol	
TS-1	1:1(10.24)	0.40	-	-	-	21
	1:3(15.85)	0.64	-	-	-	26
	1:5(21.54)	0.67	-	-	-	28
	1:7(27.18)	0.88	0.03	0.02	-	32
	1:9(32.82)	0.88	-	0.03	-	31
	1:11(38.48)	0.82	0.07	0.03	-	35
	1:13(44.13)	0.81	0.02	0.05	-	31

H_2O_2 efficiency = (mole of H_2O_2 decomposed/starting mole of H_2O_2)x100

Reaction condition: 0.05 g of catalyst, acetonitrile 5.66 g, benzene 0.0224 mole, 60°C for 3 h.

4.5.1.2 Effect of transition metal

The influences of second metal on the yield of phenol were shown in Table 4.14. The value of phenol yield around 5.56% was achieved over the using of V/TS-1 catalyst. On the contrary, Ce/TS-1, Cu/TS-1 and Fe/TS-1 showed lower catalytic activity than V/TS-1 due to small number of active surface area, which caused by the low metal dispersion. These results corresponded to the characterization of TEM, which demonstrate that the aggregation of Ce, Cu and Fe species occurred on the surface of Ce/TS-1, Cu/TS-1 and Fe/TS-1. As a result, V was considered as the suitable second metal for TS-1.

Table 4.14 Effect of transition metal supported on TS-1 for benzene hydroxylation reaction.

Catalyst	% yield by mole				H_2O_2 efficiency
	Phenol	Hydro quinone	Benzo quinone	Catechol	
TS-1	0.88	0.03	0.02	-	32
Ce/TS-1	0.99	-	-	-	35
Cu/TS-1	3.78	-	0.20	-	44
Fe/TS-1	trace	-	-	-	21
V/TS-1	5.56	-	-	-	46

H_2O_2 efficiency = (mole of H_2O_2 decomposed/starting mole of H_2O_2)x100

Reaction condition: 0.05 g of catalyst, acetonitrile 5.66 g, benzene: H_2O_2 mole ratio = 1:7, 60°C for 3 h (total volume 27.18 g).

4.5.1.3 Effect of benzene to hydrogen peroxide mole ratio for V/TS-1

The effect of benzene to hydrogen peroxide mole ratio over V/TS-1 catalyst was studied and the results are listed in Table 4.15. From the results, benzene to hydrogen peroxide mole ratio of 1:11 is suitable ratio to get maximum yield of phenol, whereas the best condition of TS-1 was 1:7 (Table 4.13). This result indicated that, although both TS-1 and V/TS-1 have the same supporter, the optimal condition was differed because of the chemical nature of catalyst. Thus, 1:11 was considered as suitable for benzene to hydrogen peroxide mole ratio for V/TS-1 for determination in the next step.

Table 4.15 Effect of benzene:H_2O_2 mole ratio on the catalytic activity of V/TS-1.

Mole ratio of Benzene:H_2O_2 (in total volume /g)	% yield by mole				H_2O_2 efficiency
	Phenol	Hydro quinone	Benzo quinone	Catechol	
1:1(10.24)	3.34	-	-	-	46
1:3(15.85)	3.98	-	-	-	44
1:5(21.54)	4.51	-	-	-	46
1:7(27.18)	5.56	-	-	-	46
1:9(32.82)	6.43	-	-	-	49
1:11(38.48)	7.94	0.90	0.32	-	51
1:13(44.13)	4.59	-	0.21	-	45

H_2O_2 efficiency = (mole of H_2O_2 decomposed/starting mole of H_2O_2)x100

Reaction condition: 0.05 g of 10 wt.% V/TS-1, acetonitrile 5.66 g, benzene = 0.0224 mole, 60°C, 3 h.

4.5.1.4 Effect of catalytic amount

Table 4.16 demonstrated the influence of V/TS-1 amount on the reaction. The yield of phenol increased with increasing the amount of catalyst and reached a maximum value of phenol yield 9.16% over 0.075g (4.3% base on weight of benzene) of catalyst. Furthermore, the yield of phenol sharply decreased when the amount of catalyst was over 0.075g. This resulted from the self-decomposition of hydrogen peroxide over excessive amount of catalyst [79]. The results are in accordance with the hydrogen peroxide efficiency that exhibited the increase of H_2O_2 consumption. Therefore, the amount of V/TS-1 catalyst was used at 0.075g in the other catalytic testing parameters.

Table 4.16 Effect of V/TS-1 amount on benzene hydroxylation reaction.

Catalyst amount (g,%)	% yield by mole				H_2O_2 efficiency
	Phenol	Hydro quinone	Benzo quinone	Catechol	
0 (0%)	trace	-	-	-	18
0.025 (1.4%)	4.51	-	-	-	42
0.050 (2.9%)	7.94	0.90	0.32	-	51
0.075 (4.3%)	9.16	1.18	0.45	-	59
0.100 (5.7%)	3.51	0.31	0.23	-	60
0.150 (8.6%)	trace	-	-	-	63

H_2O_2 efficiency = (mole of H_2O_2 decomposed/starting mole of H_2O_2)x100

Reaction condition: 10 wt.% V/TS-1 catalyst, acetonitrile 5.66 g, benzene:H_2O_2 mole ratio = 1:11, 60°C for 3 h, % catalyst based on weight of benzene(total volume 38.48 g).

4.5.1.5 Effect of reaction time

The effect of the reaction time on the yield of phenol was shown in Table 4.17. The results observed that the phenol yield continuously increased from 4.59% to 9.16% when the reaction time was extended from 0.5 h to 3 h. In addition, the yield of phenol became decreasing when the reaction time was over than 3 h because of the deep oxidation of the product [80]. Thus, the optimal reaction time for the V/TS-1 should be 3 h.

Table 4.17 Effect of reaction time on benzene hydroxylation reaction.

Reaction time (h)	% yield by mole				H_2O_2 efficiency
	Phenol	Hydro quinone	Benzo quinone	Catechol	
0.5	4.59	-	-	-	39
1	5.93	-	-	-	45
2	6.61	0.35	0.34	-	48
3	9.16	1.18	0.45	-	59
4	7.76	-	1.52	-	57
5	7.70	-	1.79	-	62

H_2O_2 efficiency = (mole of H_2O_2 decomposed/starting mole of H_2O_2)x100

Reaction condition: 10 wt.% V/TS-1 catalyst, acetonitrile 5.66 g, benzene: H_2O_2 mole ratio = 1:11, catalytic amount = 0.075g, 60°C(total volume 38.48 g).

4.5.1.6 Effect of reaction temperature

The influence of reaction temperature on the reactivity of benzene hydroxylation was investigated and the results were illustrated in Table 4.18. From the results, the yield of phenol increased with increasing the reaction temperature and provided the highest yield as 10.02% when the reaction temperature rose up to 55°C. However, further increase in temperature to 60°C caused a decrease in phenol yield because of the further oxidation of phenol. Moreover, the yield of phenol sharply decreased at the reaction temperature 65 and 70°C due to the thermal decomposition of hydrogen peroxide to H_2O and O_2 at higher temperatures. Therefore, 55°C was considered as a suitable reaction temperature for phenol production.

Table 4.18 Effect of Reaction temperature on benzene hydroxylation reaction.

Reaction temperature (°C)	% yield by mole				H_2O_2 efficiency
	Phenol	Hydro quinone	Benzo quinone	Catechol	
50	6.60	-	0.23	-	43
55	10.02	-	0.29	-	55
60	9.16	1.18	0.45	-	59
65	1.75	-	-	-	76
70	trace	-	-	-	100

H_2O_2 efficiency = (mole of H_2O_2 decomposed/starting mole of H_2O_2)x100

Reaction condition: 10 wt.% V/TS-1 catalyst, acetonitrile 5.66 g, benzene: H_2O_2 mole ratio = 1:11, catalytic amount = 0.075 g for 3 h in total volume 38.48 g.

4.5.1.7 Effect of vanadium content

The catalytic efficiency of V/TS-1 with different V-contents was tested in benzene hydroxylation. The amount of V loading was varied from 5 wt.% to 20 wt.%. As can be seen in Table 4.19, the phenol yield continually increased from 6.92% to 10.02% when the content of vanadium was raised from 5 wt.% to 10 wt.%. With increasing the vanadium concentration, the reduction in the yield of phenol was observed. These results were consistent with DR-UV and TEM data. For 10 wt.% V/TS-1, the vanadium oxide species mainly located in the form of VO_4. This form is an active site for benzene hydroxylation. Thus, the good dispersion of VO_4 species could increase the active site for 10 wt.% V/TS-1. At the lower vanadium content (5 wt.%), this catalyst showed the lower catalytic efficiency than 10 wt.% V/TS-1. This result caused by lower amount of active site. However, the turn over number (TON) of 5 wt.% V/TS-1 exhibited higher valve than 10 wt.% V/TS-1. In the case of 15 wt.% and 20 wt.%, the high vanadium loading favored the existence of vanadium in the form of inactive species resulting in the lower catalytic activity. Therefore, the suitable V-content of TS-1 was 10 wt.%.

Table 4.19 Effect of vanadium contents on benzene hydroxylation reaction.

V amount (wt.%)	% yield by mole				H_2O_2 efficiency	TON
	Phenol	Hydro quinone	Benzo quinone	Catechol		
5	6.92	-	0.19	-	44	19
10	10.02	-	0.29	-	55	15
15	6.38	-	0.44	-	45	7
20	6.55	-	-	-	48	5

H_2O_2 efficiency = (mole of H_2O_2 decomposed/starting mole of H_2O_2)x100

Reaction condition: V/TS-1 catalyst, acetonitrile 5.66 g, benzene: H_2O_2 mole ratio = 1:11, catalytic amount = 0.075 g, 55°C for 3 h in total volume 38.48 g.

4.5.1.8 Activity of reused catalyst

The reusability of 10 wt.% V/TS-1 catalyst in benzene hydroxylation reaction was evaluated and the results were summarized in Table 4.20. The yield of phenol was sharply decreased, which can be considered as the V leaching from the impregnated catalyst. On the contrary, regenerated catalyst provided 9.60% yield of phenol that slightly decreased when compared with fresh catalyst.

Table 4.20 The catalytic performance of reused and regenerated V/TS-1 catalyst on benzene hydroxylation reaction.

Catalyst	Cycle	% yield by mole				H_2O_2 efficiency
		Phenol	Hydro quinone	Benzo quinone	Catechol	
V/TS-1	1 (Fresh)	10.02	-	0.29	-	55
	2	0.22	-	-	-	30
Regenerated V/TS-1	1	9.60	-	0.11	-	46

H_2O_2 efficiency = (mole of H_2O_2 decomposed/starting mole of H_2O_2)x100

Reaction condition: 10 wt.% V/TS-1 catalyst, acetonitrile 5.66 g, benzene: H_2O_2 mole ratio = 1:11, catalytic amount = 0.075 g, 55°C for 3 h in total volume 38.48 g.

By experimenting over wide ranges of reaction parameters for the benzene hydroxylation over the series of metal supported on TS-1 catalyst, the optimal conditions were derived at benzene to hydrogen peroxide mole ratio of 1:11, 0.075 g of 10 wt.% V/TS-1 catalyst in the presence of acetonitrile 5.66 g at the reaction temperature is 55°C for 3 h. At the optimum condition, V/TS-1 with 10 wt.% of vanadium content provided a highest 10.02 % yield of phenol. This optimum condition was used as primary reaction condition scanning for other catalysts.

4.5.2 Catalytic testing of M/Ti-MWW on benzene hydroxylation

4.5.2.1 Effect of transition metal

Table 4.21 displayed the effect of transition metal on the yield of phenol. The highest yield of phenol (9.66%) was achieved at high H_2O_2 efficiency by using V/Ti-MWW catalyst. However, Ce/Ti-MWW, Cu/Ti-MWW and Fe/Ti-MWW showed lower catalytic performance than V/Ti-MWW because of lower active surface area. This result caused by the aggregation of metal particles on the surface of Ti-MWW, which confirmed by TEM result.

Table 4.21 Effect of transition metal supported on Ti-MWW for benzene hydroxylation reaction.

Catalyst	% yield by mole				H_2O_2 efficiency
	Phenol	Hydro quinone	Benzo quinone	Catechol	
Ti-MWW	0.15	-	-	-	21
Ce/Ti-MWW	0.10	-	-	-	21
Cu/Ti-MWW	6.29	0.15	0.64	0.55	62
Fe/Ti-MWW	0.17	-	trace	-	33
V/Ti-MWW	9.66	-	0.22	-	77

H_2O_2 efficiency = (mole of H_2O_2 decomposed/starting mole of H_2O_2)x100

Reaction condition: 0.075 g of catalyst, acetonitrile 5.66 g, benzene: H_2O_2 mole ratio = 1:11, 55°Cfor 3 h(total volume 38.48 g).

4.5.2.2 Effect of benzene to hydrogen peroxide mole ratio

The influence of mole ratio of benzene to hydrogen peroxide over V/Ti-MWW was investigated and the results are shown in Table 4.22. When the benzene : H_2O_2 mole ratio increased from 1:1 to 1:3, the yield of phenol rapidly increased from 7.07% to 12.81%. Moreover, a decrease in the yield of phenol was observed with a further increase the amount of H_2O_2. At the benzene : H_2O_2 mole ratio was over 1:3, the efficiency of H_2O_2 utilization decreased. Therefore, benzene to hydrogen peroxide mole ratio of 1:3 was used in the following experimental testing.

Table 4.22 Effect of benzene: H_2O_2 mole ratio on the catalytic performance of V/Ti-MWW

Mole ratio of Benzene:H_2O_2 (in total volume /g)	% yield by mole				H_2O_2 efficiency
	Phenol	Hydro quinone	Benzoquinone	Catechol	
1:1(10.24)	7.07	-	0.21	-	63
1:3(15.85)	12.81	-	0.24	-	96
1:5(21.54)	10.02	-	0.35	-	87
1:7(27.18)	9.67	-	0.33	-	86
1:9(32.82)	8.72	-	0.27	-	85
1:11(38.48)	9.66	-	0.22	-	77
1:13(44.13)	7.87	-	0.21	-	79

H_2O_2 efficiency = (mole of H_2O_2 decomposed/starting mole of H_2O_2)x100

Reaction condition:0.075g of 10wt.% V/Ti-MWW, acetonitrile 5.66 g, benzene 0.0224 mole, 55°C for 3 h.

4.5.2.3 Effect of catalytic amount

Table 4.23 displayed the effect of the V/Ti-MWW amount on benzene hydroxylation reaction. From the result, the reaction showed very poor yield in the reaction that absence of catalyst. With increasing the catalytic amount, the yield of phenol increased steadily and reached the maximum value of 13.69% over 0.1 g of V/Ti-MWW (5.7% base on weight of benzene). A further increase in the amount of catalyst caused a decrease in the yield of phenol because of the further oxidation of phenol and the accelerated self-decomposition of hydrogen peroxide by excess amount of catalytic active sites. The result indicated that 0.1 g of V/Ti-MWW is the suitable amount for the benzene hydroxylation.

Table 4.23 Effect of V/Ti-MWW amount on benzene hydroxylation reaction.

Catalyst amount (g,%)	% yield by mole				H_2O_2 efficiency
	Phenol	Hydro quinone	Benzo quinone	Catechol	
0 (0%)	trace	-	-	-	20
0.025 (1.4%)	11.42	-	-	-	90
0.050 (2.9%)	12.51	-	-	-	92
0.075 (4.3%)	12.81	-	0.24	-	96
0.100 (5.7%)	13.69	0.78	0.22	-	100
0.125 (7.1%)	13.15	0.42	0.55	0.10	100
0.150 (8.6%)	12.20	0.23	0.42	-	100

H_2O_2 efficiency = (mole of H_2O_2 decomposed/starting mole of H_2O_2)x100

Reaction condition: 10 wt.% V/Ti-MWW, acetonitrile 5.66 g, benzene:H_2O_2 = 1:3, 55°C, 3 h, % catalyst based on weight of benzene(total volume 15.85 g).

4.5.2.4 Effect of reaction time

The influence of the reaction time on the yield of phenol was investigated by varying the time from 0.5-5 h. The results were summarized in Table 4.24. It can be observed that the yield of phenol increased smoothly with the reaction time up to 3 h. The highest 13.69% yield of phenol was achieved. With further increasing the reaction time, the yield of phenol decreased due to the deep oxidation of phenol to form by-product. This result indicated that the optimum reaction time was 3 h.

Table 4.24 Effect of reaction time on benzene hydroxylation reaction.

Reaction time (h)	% yield by mole				H_2O_2 efficiency
	Phenol	Hydro quinone	Benzo quinone	Catechol	
0.5	10.72	-	-	-	100
1	11.87	-	-	-	100
2	13.29	-	-	-	100
3	13.69	0.78	0.22	-	100
4	13.05	0.82	0.43	-	100
5	12.45	0.66	0.52	-	100

H_2O_2 efficiency = (mole of H_2O_2 decomposed/starting mole of H_2O_2)x100

Reaction condition: 0.1 g of 10 wt.% V/Ti-MWW, acetonitrile 5.66 g, benzene:H_2O_2 = 1:3, 55°C, (total volume 15.85 g).

4.5.2.5 Effect of reaction temperature

Table 4.25 illustrated the effect of reaction temperature on the yield of phenol. The benzene hydroxylation was tested at the temperature ranging from 50-70°C. It can be seen that the yield of the phenol increased when increasing the reaction temperature and reached the plateau value of 13.69 % at 55°C. However, the phenol yield significantly decreased with increasing the reaction temperature due to the further oxidation of phenol. In addition, at higher temperatures (70°C), self-decomposition of H_2O_2 was occurred that caused a drastically reduced in the yield of phenol. Thus, the optimal reaction temperature for V/Ti-MWW was 55°C.

Table 4.25 Effect of Reaction temperature on benzene hydroxylation reaction.

Temperature (°C)	% yield by mole				H_2O_2 efficiency
	Phenol	Hydro quinone	Benzo quinone	Catechol	
50	12.17	-	-	-	100
55	13.69	0.78	0.22	-	100
60	12.21	0.88	0.47	-	100
65	11.99	0.54	-	-	100
70	trace	-	-	-	100

H_2O_2 efficiency = (mole of H_2O_2 decomposed/starting mole of H_2O_2)x100

Reaction condition: 0.1 g of 10 wt.% V/Ti-MWW, acetonitrile 5.66 g, benzene:H_2O_2 = 1:3, 3 h, (total volume 15.85 g).

4.5.2.6 Effect of vanadium content

The catalytic results of the benzene hydroxylation to phenol using V/Ti-MWW with different vanadium contents were summarized in Table 4.26. The vanadium loading on Ti-MWW was varied from 2.5 wt.% to 20 wt.%. As a result, the yield of phenol increased with increasing the vanadium content from 2.5 wt.% to 5 wt.% and reached a maximum value of 14.72% of phenol yield over 5 wt.% V/Ti-MWW which resulted from the generation of active surface area according to the higher vanadium contents. These results were consistent with those observations from DR-UV spectroscopy. V/Ti-MWW catalyst with 5 wt.% of vanadium exhibited the good dispersion of VO_4 species which was the catalytic active site for benzene hydroxylation [81]. At minimum vanadium loading (2.5 wt.%), despite the presence of highly dispersed tetrahedral V^{5+} species, it does not improve the catalytic properties of the catalyst due to less number of VO_4 species when compared to 5 wt.% V/Ti-MWW. With the increasing of the vanadium contents, an excess vanadium loading of 10, 15 and 20 wt.% caused decreasing the phenol yield because of the aggregation of vanadium species on the Ti-MWW support, as illustrated in the TEM results. The aggregation of isolated tetrahedral VO_4 species occurred to polymerized VO_4 form and bulk V_2O_5 that tend to be less active [81]. Furthermore, the low catalytic activity of 10, 15 and 20 wt.% V/Ti-MWW may be due to partial block of microporous structure by vanadium oxide cluster, which was reflected by the significant reducing of surface area (Table 4.5). In addition, 5 wt.% V/Ti-MWW showed the highest TON at 36, which indicated that a small amount of metal in catalyst exhibited the highest effectiveness of V/Ti-MWW. Among the catalytic data was showed in Table 4.26, V/Ti-MWW with 5 wt.% of vanadium was the best catalyst for the benzene hydroxylation reaction.

Table 4.26 Effect of vanadium contents on benzene hydroxylation reaction.

V amount (wt.%)	% yield by mole				H_2O_2 efficiency	TON
	Phenol	Hydro quinone	Benzo quinone	Catechol		
2.5	9.97	-	-	-	100	31
5	14.72	1.09	0.38	-	100	36
10	13.69	0.78	0.22	-	100	20
15	12.16	-	0.12	-	100	12
20	11.87	-	0.10	-	100	10

H_2O_2 efficiency = (mole of H_2O_2 decomposed/starting mole of H_2O_2)x100

Reaction condition: 0.1g of V/Ti-MWW, acetonitrile 5.66 g, benzene:H_2O_2 = 1:3, 55°C, 3 h, (total volume 15.85 g).

4.5.2.6.1 Mechanism of reaction

The mechanism of benzene hydroxylation with hydrogen peroxide over vanadium supported on Ti-MWW was shown in Figure 4.42. At first, vanadium interacted with hydrogen peroxide to form an unstable vanadium (V) hydroperoxy species (2). Then, vanadium (V) hydroperoxy species rapidly transformed into a vanadium (V) peroxo species (3) on loss of a water molecule. The species (3) interacted with the benzene substrate to give a metallo-peroxy-arene intermediate species (4). After that, transfer of oxygen by C–H bond activation took place in a rate determining step to give vanadium (IV) phenoxy intermediate species (5). Homolytic cleavage in species (5) resulted in rapid dissociation to give phenol and regenerating the species (1) and a small amount of vanadium (IV) hydroxo species (6) in a catalytic cycle[82].

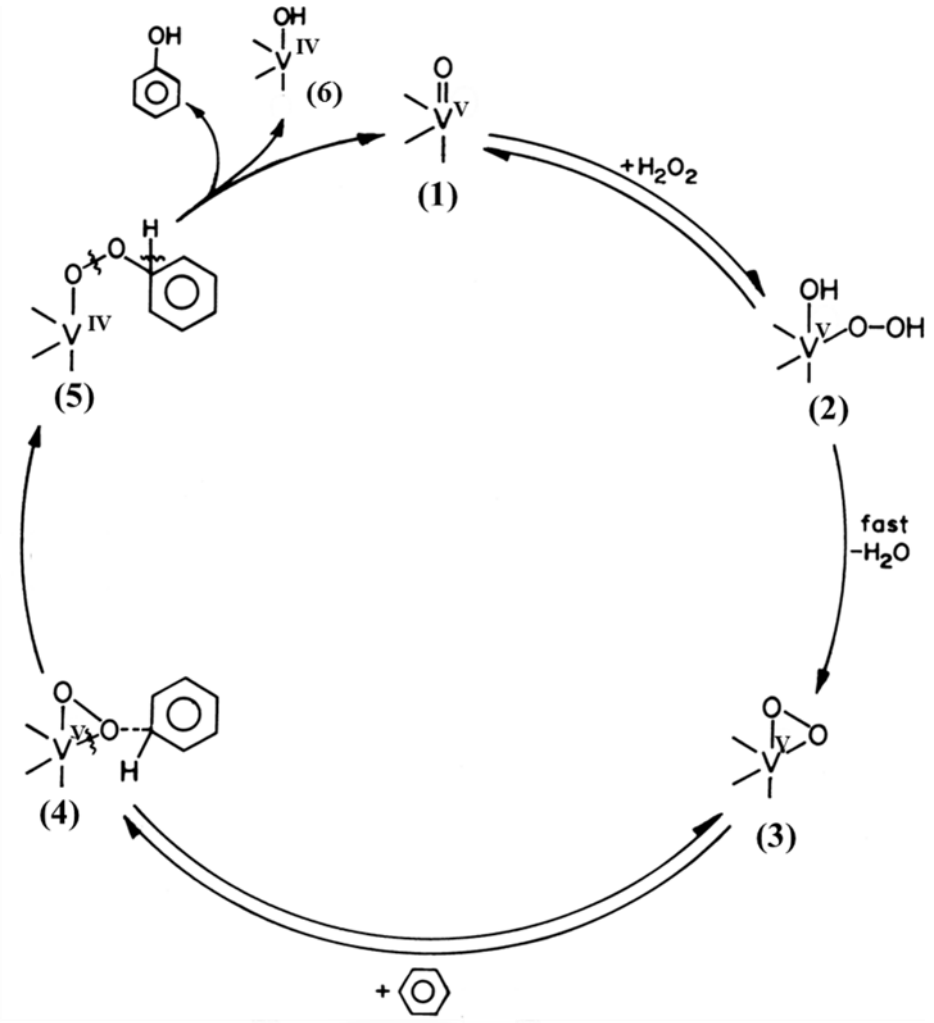

Figure 4.42 Mechanism of benzene hydroxylation with hydrogen peroxide over vanadium supported on Ti-MWW.

4.5.2.7 Effect of Si/Ti mole ratio

Table 4.27 showed the effect of Si/Ti mole ratio on benzene hydroxylation reaction. From the result, the yield of phenol slightly decreased when decrease the amount of titanium. However, 5 wt.% V/Ti-MWW with Si/Ti = 40 provided the highest yield of phenol. Therefore, Si/Ti mole ratio = 40 was considered as a suitable for vanadium impregnated support.

Table 4.27 Effect of Si/Ti mole ratio on benzene hydroxylation reaction.

Si/Ti mole ratio	% yield by mole				H_2O_2 efficiency	TON
	Phenol	Hydro quinone	Benzo quinone	Catechol		
100	13.70	0.88	0.22	-	100	31
70	13.90	0.85	0.28	-	100	33
40	14.72	1.09	0.38	-	100	36

H_2O_2 efficiency = (mole of H_2O_2 decomposed/starting mole of H_2O_2)x100

Reaction condition: 0.1g of 5wt.%V/Ti-MWW, acetonitrile 5.66 g, benzene:H_2O_2 = 1:3, 55°C, 3 h, (total volume 15.85 g).

4.5.2.8 Effect of solvent

Benzene hydroxylation reaction was carried out in different solvents such as acetonitrile, acetone, methanol and water, including solvent free. The results are summarized in Table 4.28. The maximum yield of phenol was obtained in the presence of acetonitrile because the poor scavenging ability of acetonitrile caused an increase the conversion of benzene. Acetonitrile is an aprotic solvent. The enhancing in activity of catalysts in acetonitrile can be explained on the basis of polarity. The activity of catalyst was found to increase with the solvent polarity. In the same polarity index as acetonitrile, acetic acid showed the lower yield of phenol than acetonitrile due to the acceleration of hydrogen peroxide decomposition[82]. For the using of water and solvent free, phase separation between benzene and water was occurred leading to mass transport limitation. Therefore, in terms of both the scavenging ability and its polarity, acetonitrile was the most suitable solvent for the benzene hydroxylation.

Table 4.28 Effect of solvent on benzene hydroxylation reaction.

Solvent	% yield by mole				H_2O_2 efficiency	Polarity index
	Phenol	Hydro quinone	Benzo quinone	Catechol		
Acetonitrile	14.72	1.09	0.38	-	100	6.2
Acetone	3.04	-	-	0.11	77	4.3
Methanol	5.33	0.19	-	-	81	5.1
Acetic acid	7.99	-	trace	-	100	6.2
water	2.15	trace	-	-	56	9.0
Solvent free	trace	-	-	-	31	-

H_2O_2 efficiency = (mole of H_2O_2 decomposed/starting mole of H_2O_2)x100

Reaction condition: 0.1g of 5wt.%V/Ti-MWW, solvent 5.66 g, benzene:H_2O_2 = 1:3, 55°C, 3 h, (total volume 15.85 g).

4.5.2.9 Activity of reuse catalyst

Another important factor in the catalytic performance of materials was their stability during catalytic process. The reusability of V/Ti-MWW was tested at the optimum reaction condition. The results were shown in Table 4.29. A significant loss in activity was observed for V/Ti-MWW. This result caused by the leaching of vanadium species. In order to avoid leaching, surface of Ti-MWW was modified by 3-aminopropyltrimethoxysilane before the immobilization of vanadium. From the results, VO-propyl-NH2-anchoring on Ti-MWW catalyst was recycled with stable catalytic performance than V/Ti-MWW because VO-propyl-NH2-anchoring on Ti-MWW had the strong anchoring of vanadium which preventing the leaching of vanadium from the catalyst. Although the yield of phenol over VO-propyl-NH2-anchoring on Ti-MWW was lower than V/Ti-MWW in the first and second runs, the major advantage of the VO-propyl-NH2-anchoring on Ti-MWW catalyst was the high durability during catalytic process. Thus, VO-propyl-NH2-anchoring on Ti-MWW was the alternative catalyst for improving the catalytic stability.

Table 4.29 The catalytic performance of reused V/Ti-MWW catalyst.

Catalyst	Cycle	% yield by mole				H_2O_2 efficiency
		Phenol	Hydro quinone	Benzo quinone	Catechol	
V/Ti-MWW (Si/Ti=39, V=4.35 wt.%)[a]	1 (Fresh)	14.72	1.09	0.38	-	100
	2	8.66	0.71	0.14	-	76
	3	4.30	-	-	-	51
	4	0.27	-	-	-	36
VO-propyl-NH2-anchoring on Ti-MWW (Si/Ti=44, V=3.97 wt.%)[a]	1 (Fresh)	7.02	0.22	0.10	-	67
	2	6.96	0.15	0.04	-	65
	3	6.30	trace	-	-	61
	4	5.97	trace	-	-	59

[a]Inductively Coupled Plasma Mass Spectrometry (ICP-MS)

H_2O_2 efficiency = (mole of H_2O_2 decomposed/starting mole of H_2O_2)x100

Reaction condition: 0.1g of 5wt.%V/Ti-MWW, acetonitrile 5.66 g, benzene:H_2O_2 = 1:3, 55°C, 3 h, (total volume 15.85 g).

4.5.3 Catalytic testing of M/Ti-MCA on benzene hydroxylation

4.5.3.1 Effect of transition metal

The effect of second metal on the yield of phenol was investigated. The results were given in Table 4.30. The addition of copper and vanadium on the Ti-MCA support enhanced catalytic oxidation capacity when compared with other metals. V incorporated Ti-MCA showed the highest 9.02% yield of phenol with high H_2O_2 efficiency. These catalytic results were consistent with characterization part. TEM data showed that the highly dispersion of V species whereas Ce, Cu and Fe particles were aggregated on the surface of Ti-MCA. The aggregation of Ce, Cu and Fe particles led to the poor active site resulting in lower catalytic activity. Thus, V was considered as the suitable second metal for Ti-MCA.

Table 4.30 Effect of transition metal supported on Ti-MCA for benzene hydroxylation reaction.

Catalyst	% yield by mole				H_2O_2 efficiency
	Phenol	Hydro quinone	Benzo quinone	Catechol	
Ti-MCA	0.32	-	-	-	23
Ce/Ti-MCA	0.12	-	-	-	22
Cu/Ti-MCA	3.57	-	0.64	-	60
Fe/Ti-MCA	0.56	-	-	-	25
V/Ti-MCA	9.02	-	0.10	-	75

H_2O_2 efficiency = (mole of H_2O_2 decomposed/starting mole of H_2O_2)x100

Reaction condition: 0.075 g of catalyst, acetonitrile 5.66 g, benzene: H_2O_2 mole ratio = 1:11, 55°C for 3 h (total volume 38.48 g).

4.5.3.2 Effect of benzene to hydrogen peroxide mole ratio

Benzene hydroxylation reaction was carried out with varying mole ratio of benzene to hydrogen peroxide from 1:1 to 1:13. The results were summarized in Table 4.31. The yield of phenol increased steadily with increasing benzene to hydrogen peroxide mole ratio from 1:1 to 1:3. The maximum yield of phenol 12.22% was obtained with high effective utilization of H_2O_2. With further increasing the amount of H_2O_2, a decrease in the yield of phenol was observed. Therefore, the suitable benzene to hydrogen peroxide mole ratio of V/Ti-MCA was 1:3.

Table 4.31 Effect of benzene: H_2O_2 mole ratio on the catalytic performance of V/Ti-MCA

Mole ratio of Benzene:H_2O_2 (in total volume /g)	% yield by mole				H_2O_2 efficiency
	Phenol	Hydro quinone	Benzo quinone	Catechol	
1:1 (10.24)	4.93	-	-	-	31
1:3 (15.85)	12.22	0.01	0.25	-	95
1:5 (21.54)	8.64	trace	0.27	-	71
1:7 (27.18)	6.56	-	0.23	-	61
1:9 (32.82)	7.44	-	0.17	-	66
1:11 (38.48)	9.02	-	0.10	-	74
1:13 (44.13)	2.16	-	-	-	20

H_2O_2 efficiency = (mole of H_2O_2 decomposed/starting mole of H_2O_2)x100

Reaction condition: 0.075 g of 10 wt.% V/Ti-MCA, acetonitrile 5.66 g, benzene 0.0224 mole, 55°C for 3 h.

4.5.3.3 Effect of catalytic amount

The dependence of benzene hydroxylation on the amount of V/Ti-MCA catalyst was studied. The effect of the V/Ti-MCA amount on the yield of phenol was illustrated in Table 4.32. In the absence of catalyst, phenol product was achieved in trace amount. However, the yield of phenol was increased with increasing of catalytic amount and started to decrease after attaining a maximum phenol yield (13.24%) over 0.125 g of V/Ti-MCA (7.1% base on weight of benzene). The excess amount of V/Ti-MCA caused the accelerated self-decomposition of hydrogen peroxide and over oxidation of phenol to by-products. Thus, 0.125 g (7.1% base on weight of benzene) of V/Ti-MCA was the appropriate catalytic amount for this reaction.

Table 4.32 Effect of V/Ti-MCA amount on benzene hydroxylation reaction.

Catalyst amount (g,%)	% yield by mole				H_2O_2 efficiency
	Phenol	Hydro quinone	Benzo quinone	Catechol	
0 (0%)	trace	-	-	-	20
0.025 (1.4%)	11.55	-	0.09	-	90
0.050 (2.9%)	12.43	-	0.18	-	94
0.075 (4.3%)	12.22	0.01	0.25	-	95
0.100 (5.7%)	12.77	0.08	0.32	-	100
0.125 (7.1%)	13.24	0.11	0.55	-	100
0.150 (8.6%)	12.20	0.21	0.72	-	100

H_2O_2 efficiency = (mole of H_2O_2 decomposed/starting mole of H_2O_2)x100
Reaction condition: 10 wt.% V/Ti-MCA, acetonitrile 5.66 g, benzene:H_2O_2 = 1:3, 55°C, 3 h, % catalyst based on weight of benzene (total volume 15.85 g).

4.5.3.4 Effect of reaction time

The benzene hydroxylation was carried out at reaction times ranging from 0.5 to 5 h. As can be seen in Table 4.33, a gradual increase in phenol yield was observed with increasing the reaction time. The maximum yield of phenol (13.24%) was reached at reaction time of 3 h. However, the phenol yield started to decrease when the reaction time was longer than 3 h because phenol was further oxidized and converted to by-products. Hence, 3 h was taken as optimal time for phenol production over V/Ti-MCA.

Table 4.33 Effect of reaction time on benzene hydroxylation reaction.

Reaction time (h)	% yield by mole				H_2O_2 efficiency
	Phenol	Hydro quinone	Benzo quinone	Catechol	
0.5	10.37	-	-	-	100
1	11.36	-	-	-	100
2	12.24	-	0.10	-	100
3	13.24	0.11	0.55	-	100
4	13.14	0.19	0.61	-	100
5	13.08	0.28	0.72	-	100

H_2O_2 efficiency = (mole of H_2O_2 decomposed/starting mole of H_2O_2)x100

Reaction condition: 0.125 g of 10 wt.% V/Ti-MCA, acetonitrile 5.66 g, benzene:H_2O_2 = 1:3, 55°C, (total volume 15.85 g).

4.5.3.5 Effect of reaction temperature

Temperature variation on benzene hydroxylation was investigated to get the optimum reaction temperature which producing the maximum yield of phenol. The reaction temperature was varied from 50°C to 70°C and the results were shown in Table 4.34. From the results, the phenol yield gradually increased from 12.52% to 13.24% when reaction temperature increased from 50°C to 55°C. With further increasing in reaction temperature to 65°C, the yield of phenol was not improved because of over oxidation. In addition, a drastic decrease in the yield of phenol was observed at reaction temperature of 70°C. This result caused by self-decomposition of H_2O_2. Thus, the reaction temperature at 55°C was well suited for the benzene hydroxylation.

Table 4.34 Effect of reaction temperature on benzene hydroxylation reaction.

Temperature (°C)	% yield by mole				H_2O_2 efficiency
	Phenol	Hydro quinone	Benzo quinone	Catechol	
50	12.52	-	0.19	-	100
55	13.24	0.11	0.55	-	100
60	12.52	0.14	0.62	-	100
65	12.11	0.15	0.65	-	100
70	trace	-	-	-	100

H_2O_2 efficiency = (mole of H_2O_2 decomposed/starting mole of H_2O_2)x100

Reaction condition: 0.125 g of 10 wt.% V/Ti-MCA, acetonitrile 5.66 g, benzene:H_2O_2 = 1:3, 3 h, (total volume 15.85 g).

4.5.3.6 Effect of vanadium content

Table 4.35 showed the influence of vanadium contents on the yield of phenol in benzene hydroxylation reaction. Vanadium was loaded on Ti-MCA support from 5 wt.% to 20 wt.% by impregnation method. At the lowest vanadium content (5 wt.%), 12.69% yield of phenol was obtained with 100% selectivity. Side products such as hydroquinone, benzoquinone and catechol were not detected. Moreover, the increase of vanadium content to 10 wt.% had a positive effect on the phenol yield. This result caused by lower active site in 5 wt.% V/Ti-MCA resulting in lower catalytic activity than 10 wt.% V/Ti-MCA. In the case of 10 wt.% V/Ti-MCA, the highest 13.24% yield of phenol was achieved. These results were consistent with data from characterization part. Vanadium oxide species mainly existed in the form of isolated VO_4 over 10 wt.% V/Ti-MCA, as evidenced by DR-UV studies. This form is an active site for benzene hydroxylation [81]. Furthermore, the inactive bulk V_2O_5 phase was not detected by XRD over 10 wt.% V/Ti-MCA. Thus, 10 wt.% V/Ti-MCA showed high catalytic performance in benzene hydroxylation. However, the turnover number (TON) of 5 wt.% V/Ti-MCA showed higher valve than 10 wt.% V/Ti-MCA. However, further increasing in vanadium content led to the decrease in phenol yield. From TEM data it was confirmed that vanadium oxide species was aggregated at the high vanadium content (15 and 20 wt.%). The low dispersion of vanadium species caused a decrease in active site resulting in lower catalytic activity. Therefore, the excessive vanadium content was not improved the phenol yield. From the above discussion it was clear that 10 wt.% V/Ti-MCA was the best catalyst for the benzene hydroxylation reaction.

Table 4.35 Effect of vanadium contents on benzene hydroxylation reaction.

V amount (wt.%)	% yield by mole				H_2O_2 efficiency	TON
	Phenol	Hydro quinone	Benzo quinone	Catechol		
5	12.69	-	-	-	100	33
10	13.24	0.11	0.55	-	100	21
15	12.98	0.09	0.42	-	100	14
20	12.49	-	0.18	-	100	10

H_2O_2 efficiency = (mole of H_2O_2 decomposed/starting mole of H_2O_2)x100

Reaction condition: 0.125 g of V/Ti-MCA, acetonitrile 5.66 g, benzene:H_2O_2 = 1:3, 55°C, 3 h, (total volume 15.85 g).

4.5.3.7 Activity of reuse catalyst

To examine the reusability of catalyst, V/Ti-MCA was tested in benzene hydroxylation at the optimum condition for four times. The results were shown in Table 4.36. The yield of phenol decreased significantly from 13.24% to 0.30% after the fourth reaction cycle. This result can be described as the leaching of vanadium species from the impregnated V/Ti-MCA catalyst.

Table 4.36 The catalytic performance of reused V/Ti-MCA catalyst on benzene hydroxylation reaction.

Catalyst	cycle	% yield by mole				H_2O_2 efficiency
		Phenol	Hydro quinone	Benzo quinone	Catechol	
V/Ti-MCA	1(Fresh)	13.24	0.11	0.55	-	100
	2	7.98	-	0.10	-	75
	3	3.30	-	trace	-	49
	4	0.30	-	-	-	36

H_2O_2 efficiency = (mole of H_2O_2 decomposed/starting mole of H_2O_2)x100

Reaction condition: 0.125 g of catalyst (10 wt.% of V), acetonitrile 5.66 g, benzene:H_2O_2 = 1:3, 55°C, 3 h, (total volume 15.85 g).

4.5.4 Catalytic testing of M/Ti-SBA-15 on benzene hydroxylation

4.5.4.1 Effect of transition metal

In order to study the bi-component catalysts for benzene hydroxylation, the second metal in this study were Ce, Cu, Fe and V. Table 4.37 showed the catalytic performances in the hydroxylation of benzene over bi-metal supported on Ti-SBA-15 catalysts. Comparison with Ti-SBA-15, the Ce/Ti-SBA-15 and Fe/Ti-SBA-15 catalysts showed the slightly difference in the yield of phenol due to the aggregation of Ce and Fe species on the surface of Ce/Ti-SBA-15 and Fe/Ti-SBA-15, which were agreement with the TEM results. However, the Cu/Ti-SBA-15 and V/Ti-SBA-15 catalysts improved the phenol yield considerably. Moreover, V/Ti-SBA-15 provided the highest 6.46% yield of phenol. Therefore, the results found that V was the suitable second metal for Ti-SBA-15.

Table 4.37 Effect of transition metal supported on Ti-SBA-15 for benzene hydroxylation reaction.

Catalyst	% yield by mole				H_2O_2 efficiency
	Phenol	Hydro quinone	Benzo quinone	Catechol	
Ti-SBA-15	0.18	-	-	-	22
Ce/Ti-SBA-15	1.02	-	-	-	27
Cu/Ti-SBA-15	5.40	trace	-	-	48
Fe/Ti-SBA-15	0.26	-	-	-	24
V/Ti-SBA-15	6.46	0.24	0.12	-	60

H_2O_2 efficiency = (mole of H_2O_2 decomposed/starting mole of H_2O_2)x100

Reaction condition: 0.075 g of catalyst, acetonitrile 5.66 g, benzene: H_2O_2 mole ratio = 1:11, 55°C for 3 h (total volume 38.48 g).

4.5.4.2 Effect of benzene to hydrogen peroxide mole ratio

The effect of benzene to hydrogen peroxide mole ratio on the yield of phenol over V/Ti-SBA-15 catalyst was shown in Table 4.38. The yield of phenol increased with increasing the mole ratio of benzene to hydrogen peroxide. The highest 6.78% yield of phenol was obtained by using benzene to hydrogen peroxide mole ratio as 1:13. Therefore, 1:13 is considered as the suitable mole ratio of benzene to hydrogen peroxide for this V/Ti-SBA-15.

Table 4.38 Effect of benzene: H_2O_2 mole ratio on the catalytic performance of V/Ti-SBA-15.

Mole ratio of Benzene:H_2O_2 (in total volume /g)	% yield by mole				H_2O_2 efficiency
	Phenol	Hydro quinone	Benzo quinone	Catechol	
1:1 (10.24)	3.42	-	-	-	45
1:3 (15.85)	4.50	-	-	-	49
1:5 (21.54)	4.88	-	-	-	51
1:7 (27.18)	5.56	trace	-	-	55
1:9 (32.82)	5.91	0.10	trace	-	56
1:11 (38.48)	6.46	0.24	0.12	-	60
1:13 (44.13)	6.78	0.33	0.25	-	61
1:15 (49.68)	6.34	0.19	trace	-	53

H_2O_2 efficiency = (mole of H_2O_2 decomposed/starting mole of H_2O_2)x100

Reaction condition: 0.075 g of 10 wt.% V/Ti-SBA-15, acetonitrile 5.66 g, benzene 0.0224 mole, 55°C for 3 h.

4.5.4.3 Effect of catalytic amount

Table 4.39 displayed the effect of the amount of V/Ti-SBA-15 catalyst on benzene hydroxylation reaction. From the results, poor yield of phenol was observed in the reaction that absence of catalyst. However, the phenol yield increased from 3.24% to 6.83% when the amount of V/Ti-SBA-15 catalyst increased from 0.025 g (1.4% base on weight of benzene) to 0.050 g (2.9% base on weight of benzene) owing to the increase in active sites. At the amount of catalyst was over 0.050 g, the phenol yield gradually decreased due to the excess catalytic active sites which not only provided the further oxidation of reaction products but also in favor of the self-decomposition of hydrogen peroxide. Thus, the suitable amount of V/Ti-SBA-15 catalyst for the benzene hydroxylation was 0.050 g.

Table 4.39 Effect of V/Ti-SBA-15 amount on benzene hydroxylation reaction.

Catalyst amount (g,%)	% yield by mole				H_2O_2 efficiency
	Phenol	Hydro quinone	Benzo quinone	Catechol	
0 (0%)	trace	-	-	-	19
0.025 (1.4%)	3.24	0.05	-	-	47
0.050 (2.9%)	6.83	0.14	0.08	-	59
0.075 (4.3%)	6.78	0.33	0.25	-	61
0.100 (5.7%)	5.69	0.42	0.28	-	67
0.125 (7.1%)	4.34	0.18	0.02	-	73
0.150 (8.6%)	1.36	-	-	-	81

H_2O_2 efficiency = (mole of H_2O_2 decomposed/starting mole of H_2O_2)x100

Reaction condition: 10 wt.% V/Ti-SBA-15, acetonitrile 5.66 g, benzene:H_2O_2 = 1:13, 55°C, 3 h, % catalyst based on weight of benzene (total volume 44.13 g).

From above results, V/Ti-SBA-15 catalyst was eliminated from the candidate catalyst because it exhibited poorest catalytic activity when compared with other catalysts. Therefore, V/Ti-SBA-15 catalyst was not explored in the other catalytic testing parameters.

4.5.5 Catalytic activity of vanadium supported on titanosilicate catalyst on benzene hydroxylation

Table 4.40 showed the results of benzene hydroxylation over vanadium supported on titanosilicate catalyst such as V/TS-1, V/Ti-MWW and V/Ti-MCA. The results were reported at the optimum reaction condition of each catalyst. The vanadium supported on titanosilicates exhibited the catalytic performance on benzene hydroxylation in the order of V/Ti-MWW > V/Ti-MCA > V/TS-1. From previous research, the dispersion and nature of metal oxide in the catalysts had tremendous influence on the catalytic activity [83]. For the prepared catalysts at this optimum condition, vanadium oxide mainly located in the form of VO_4 which was the catalytic active site for benzene hydroxylation [81]. Therefore, another important factor affecting the catalytic performance was their structure of catalyst support. Although TS-1 was well known as effective redox catalyst, vanadium supported on TS-1 showed a lowest yield of phenol. This result caused by small pore size that led to mass transport limitation resulting in a lower catalytic activity than other catalysts [84]. In the case of catalyst with larger pore size, V/Ti-MCA was more active than V/TS-1 by showing the phenol yield of 13.24%. The large pore of V/Ti-MCA catalyst with its three-dimensional channel system provided favorable mass transfer resulting in efficient diffusion and transport of reactants and products in the reactions [34]. Furthermore, superior to other catalysts, vanadium supported on Ti-MWW showed a highest catalytic activity which produced 14.72% yield of phenol. The effective catalytic behavior of V/Ti-MWW not only caused by three-dimensional structure but

also resulted from the possessing of unique pore system. V/Ti-MWW has 12-membered ring supercages as well as external half cups that open reaction space for reactants [85]. Thus, V/Ti-MWW showed the highest catalytic performance in benzene hydroxylation.

Table 4.40 Catalytic activity of vanadium supported titanosilicate catalyst on benzene hydroxylation

Catalyst	% yield by mole				H_2O_2[a] efficiency	TON
	Phenol	Hydro quinone	Benzo quinone	Catechol		
V/TS-1[b]	10.02	-	0.29	-	55	15
V/Ti-MWW[c]	14.72	1.09	0.38	-	100	36
V/Ti-MCA[d]	13.24	0.11	0.55	-	100	21

[a] H_2O_2 efficiency = (mole of H_2O_2 decomposed/starting mole of H_2O_2)x100

[b] Optimum condition: 0.075g of 10wt.% V/TS-1, acetonitrile 5.66g, benzene:H_2O_2 mole ratio=1:11, 55°C, 3h

[c] Optimum condition: 0.1g of 5wt.%V/Ti-MWW, acetonitrile 5.66g, benzene:H_2O_2 mole ratio=1:3, 55°C, 3h

[d] Optimum condition: 0.125g of 10wt.% V/Ti-MCA, acetonitrile 5.66g, benzene:H_2O_2 mole ratio=1:3, 55°C, 3h.

CHAPTER V
CONCLUSIONS

The microporous and mesoporous titanosilicates with the transition metal (Ce, Cu, Fe, or V) were successfully synthesized by hydrothermal followed by impregnation method. All synthesized products were characterized by using X-ray powder diffraction, N_2 adsorption-desorption, DR-UV spectrophotometry, SEM, TEM and ICP-MS. The XRD patterns of all catalysts indicated the characteristic peak of each parent material. N_2 adsorption-desorption isotherms exhibited a type I according to the IUPAC classification for microporous material for TS-1 and Ti-MWW and type IV, which referred to typical shape of mesoporous structures for Ti-MCA and Ti-SBA-15. For DR-UV spectra, bimetallic catalysts as Ce, Cu and Fe supported on titanosilicates exhibited the aggregation of metal oxide species which confirmed by TEM images. As the same metal content, vanadium bimetallic catalyst exhibited better dispersion than other catalysts. SEM results indicated that the morphology of all bimetallic catalysts was similar to parent material. Amount of vanadium in catalysts were determined by using ICP-MS. The 10 wt.% vanadium supported on titanosilicates showed the amount of vanadium as 9.16, 9.20 and 9.18 wt.% for V/TS-1, V/Ti-MWW and V/Ti-MCA, respectively. For the series of vanadium supported on micro- and mesoporous titanosilicates with different vanadium contents, the structure of titanosilicate parent material of all catalysts were well retained at high vanadium loading. The dispersion and nature of vanadium species strongly depended on vanadium content. Isolated tetrahedral VO_4 is the main existence species at low vanadium loading. With the increasing of vanadium content, isolated tetrahedral VO_4 was aggregated. At high vanadium concentration, vanadium favored the existence in the form of bulk V_2O_5. V/TS-1, V/Ti-MWW and V/Ti-MCA showed V_2O_5 phase at vanadium content 10, 5 and 15 wt.%, respectively.

In the benzene hydroxylation, the reaction was carried out by varying catalyst types including M/TS-1, M/Ti-MWW, M/Ti-MCA and M/Ti-SBA-15 by using hydrogen peroxide as an oxidant. V as second metal presented the best catalytic activity in all titanosilicate supporters. Nature and dispersion of vanadium species as well as structure of support had tremendous effect on the yield of phenol. It was found that V/Ti-MWW with 5 wt% V-content showed highest catalytic performance with 14.72% yield of phenol. The optimum condition was carried at benzene: H_2O_2 mole ratio of 1:3, 0.1 g of catalyst, acetonitrile 5.66 g, 55°C for 3 h.

The suggestions for future work

- Modify V/Ti-MWW to give its higher stability and more cycle in reuse process.
- Find the other catalyst supports such as LUS-1 that can be used as catalyst in benzene hydroxylation.

REFERENCES

[1] Global phenol consumption 2015 [Online]. Available from: http://www.icis.com/resources/news/2016/06/09/10006764/market-outlook-phenol-acetone-markets-are-under-ressure-icis-consulting/ [14 November]

[2] Global bisphenol A polymer market [Online]. Available from: http://www.transparencymarketresearch.com/bisphenol-a-market.html [14 November]

[3] Global phenolic resins market [Online]. Available from: http://www.marketresearchstore.com/report/phenolic-resins-market-for-z37563 [14 November]

[4] Cumene process [Online]. Available from: https://en.wikipedia.org/wiki/Cumene_process [15 November]

[5] Pirutko, L.V., Uriarte, A.K., Chernyavsky, V.S., Kharitonov, A.S., and Panov, G.I. Preparation and catalytic study of metal modified TS-1 in the oxidation of benzene to phenol by N2O. Microporous and Mesoporous Materials 48(1–3) (2001): 345-353.

[6] Bahidsky, M. and Hronec, M. Direct hydroxylation of aromatics over copper–calcium–phosphates in the gas phase. Catalysis Today 99(1–2) (2005): 187-192.

[7] Yuranov, I., Bulushev, D.A., Renken, A., and Kiwi-Minsker, L. Benzene to phenol hydroxylation with N2O over Fe-Beta and Fe-ZSM-5: Comparison of activity per Fe-site. Applied Catalysis A: General 319 (2007): 128-136.

[8] Battistel, E., Tassinari, R., Fornaroli, M., and Bonoldi, L. Oxidation of benzene by molecular oxygen catalysed by vanadium. Journal of Molecular Catalysis A: Chemical 202(1–2) (2003): 107-115.

[9] Liu, Y., Murata, K., and Inaba, M. Direct oxidation of benzene to phenol by molecular oxygen over catalytic systems containing Pd(OAc)2 and heteropolyacid immobilized on HMS or PIM. Journal of Molecular Catalysis A: Chemical 256(1–2) (2006): 247-255.

[10] Gu, Y.-Y., Zhao, X.-H., Zhang, G.-R., Ding, H.-M., and Shan, Y.-K. Selective hydroxylation of benzene using dioxygen activated by vanadium–copper

oxide catalysts supported on SBA-15. Applied Catalysis A: General 328(2) (2007): 150-155.

[11] Parida, K.M. and Dash, S.S. Surface characterization and catalytic evaluation of manganese nodule leached residue toward oxidation of benzene to phenol. Journal of Colloid and Interface Science 316(2) (2007): 541-546.

[12] Kong, Y., Xu, X., Wu, Y., Zhang, R., and Wang, J. Effect of Promoters on the Catalytic Activity of MCM-41 with High Copper Content in Benzene Hydroxylation. Chinese Journal of Catalysis 29(4) (2008): 385-390.

[13] Zhu, Y., Dong, Y., Zhao, L., and Yuan, F. Preparation and characterization of Mesopoous VOx/SBA-16 and their application for the direct catalytic hydroxylation of benzene to phenol. Journal of Molecular Catalysis A: Chemical 315(2) (2010): 205-212.

[14] Song, S., Jiang, S., Rao, R., Yang, H., and Zhang, A. Bicomponent VO2-defects/MWCNT catalyst for hydroxylation of benzene to phenol: Promoter effect of defects on catalytic performance. Applied Catalysis A: General 401(1–2) (2011): 215-219.

[15] Wang, C., et al. Direct hydroxylation of benzene to phenol over metal oxide supported graphene oxide catalysts. Catalysis Communications 68 (2015): 1-5.

[16] Tanarungsun, G., Kiatkittipong, W., Praserthdam, P., Yamada, H., Tagawa, T., and Assabumrungrat, S. Hydroxylation of benzene to phenol on Fe/TiO2 catalysts loaded with different types of second metal. Catalysis Communications 9(9) (2008): 1886-1890.

[17] Adam, F. and Thankappan, R. Oxidation of benzene over bimetallic Cu–Ce incorporated rice husk silica catalysts. Chemical Engineering Journal 160(1) (2010): 249-258.

[18] Xu, D., Jia, L., and Guo, X. Cu-doped mesoporous VOx-TiO2 in catalytic hydroxylation of benzene to phenol. Chinese Journal of Catalysis 34(2) (2013): 341-350.

[19] Hu, L., Yue, B., Chen, X., and He, H. Direct hydroxylation of benzene to phenol on Cu–V bimetal modified HMS catalysts. Catalysis Communications 43 (2014): 179-183.

[20] Ye, X., Cui, Y., Qiu, X., and Wang, X. Selective oxidation of benzene to phenol by Fe-CN/TS-1 catalysts under visible light irradiation. Applied Catalysis B: Environmental 152–153 (2014): 383-389.

[21] The effect of a catalyst on the activation energy of a reaction [Online]. Available from: http://archive.cnx.org/contents/ea93e564-1498-4e31-9c4e-3aba71467a82@2/reaction-rates [15 November]

[22] Type of catalyst [Online]. Available from: http://byjus.com/chemistry/types-of-catalyst/ [15 November]

[23] Microporous material [Online]. Available from: https://en.wikipedia.org/wiki/Microporous_material [15 November]

[24] Primary building unit of zeolite structure [Online]. Available from: http://innovareacademics.in/journals/index.php/jcr/article/view/11219/6321 [15 November]

[25] Secondary Building Units (SBU's) in zeolites [Online]. Available from: http://www.ch.ic.ac.uk/vchemlib/course/zeolite/structure.html [15 November]

[26] Three types of shape selectivity [Online]. Available from: http://what-when-how.com/wp-content/uploads/2011/03/tmpCC79_thumb_thumb.jpg [15 November]

[27] MFI structure [Online]. Available from: http://asia.iza-structure.org/IZA-SC/ftc_fw.php?STC=MFI [15 November]

[28] Khouw, C.B., Dartt, C.B., Labinger, J.A., and Davis, M.E. Studies on the Catalytic-Oxidation of Alkanes and Alkenes by Titanium Silicates. Journal of Catalysis 149(1) (1994): 195-205.

[29] Bianchi, D., D'Aloisio, R., Bortolo, R., and Ricci, M. Oxidation of mono- and bicyclic aromatic compounds with hydrogen peroxide catalyzed by titanium silicalites TS-1 and TS-1B. Applied Catalysis A: General 327(2) (2007): 295-299.

[30] Framework Type MWW [Online]. Available from: Framework Type MWW [15 November]

[31] Katiyar, A., Yadav, S., Smirniotis, P.G., and Pinto, N.G. Synthesis of ordered large pore SBA-15 spherical particles for adsorption of biomolecules. Journal of Chromatography A 1122(1–2) (2006): 13-20.

[32] Chen, L.-F., et al. Preparation of Cu/SBA-15 catalysts by different methods for the hydrogenolysis of dimethyl maleate to 1,4-butanediol. Applied Catalysis A: General 356(2) (2009): 129-136.

[33] Anbia, M. and Amirmahmoodi, S. Adsorption of phenolic compounds from aqueous solutions using functionalized SBA-15 as a nano-sorbent. Scientia Iranica 18(3) (2011): 446-452.

[34] Kubota, Y., Jin, C., and Tatsumi, T. Performance of organic–inorganic hybrid catalysts based on Ia-3d mesoporous silica. Catalysis Today 132(1–4) (2008): 75-80.

[35] Wang, S., Wu, D., Sun, Y., and Zhong, B. The Synthesis of MCM-48 with high yields. Materials Research Bulletin 36(9) (2001): 1717-1720.

[36] Barbera, D., et al. The control of selectivity in benzene hydroxylation catalyzed by TS-1: The solvent effect and the role of crystallite size. Journal of Catalysis 275(1) (2010): 158-169.

[37] He, C., Li, P., Cheng, J., Li, J., and Hao, Z. Preparation and investigation of PD/TI-SBA-15 catalysts for catalytic oxidation of benzene. Environmental Progress & Sustainable Energy 29(4) (2010): 435-442.

[38] Li, B., Wu, N., Wu, K., Liu, J., Han, C., and Li, X. Bimetallic V and Ti incorporated MCM-41 molecular sieves and their catalytic properties. RSC Adv. 5(21) (2015): 16598-16603.

[39] Diffraction of X-ray [Online]. Available from: http://www.chemistryviews.org/details/ezine/2064331/100th_Anniversary_of_the_Discovery_of_X-ray_Diffraction.html [15 November]

[40] Adsorption Isotherm [Online]. Available from: http://www.microtrac-bel.com/en/tech/bel/seminar02.html [15 November]

[41] The IUPAC classification of isotherm [Online]. Available from: http://www.jinaipu.com/eng/newsInfo.aspx?parentid=940&catid=944&newsid=12354 [15 November]

[42] BET theory [Online]. Available from: https://en.wikipedia.org/wiki/BET_theory [15 November]

[43] The schematic outline of a TEM [Online]. Available from: http://www.hk-phy.org/atomic_world/tem/tem02_e.html [15 November]

[44] Instrument Description and Theory [Online]. Available from: http://www.sees.manchester.ac.uk/our-research/facilities/geochemistry/equipmentandfacilities/icp-ms/instrumentdescriptionandtheory/ [15 November]

[45] Yeong, Y.F., Abdullah, A.Z., Ahmad, A.L., and Bhatia, S. Synthesis, structure and acid characteristics of partially crystalline silicalite-1 based materials. Microporous and Mesoporous Materials 123(1–3) (2009): 129-139.

[46] Wongkulab, S. Synthesis of titanosilicalite-1 using mixed templates and acid treated Ti-MWW catalysts for phenol hydroxylation. Master, Chulalongkorn University, 2006.

[47] Peng, W., Takashi, T., Takayuki, K., and Tatsuaki, Y. A Novel Titanosilicate with MWW Structure. I. Hydrothermal Synthesis, Elimination of Extraframework Titanium, and Characterizations. J. Phys. Chem. 105 (2001): 2897-2905.

[48] Dongyuan, Z., et al. Triblock Copolymer Syntheses of Mesoporous Silica with Periodic 50 to 300 Angstrom Pores. SCIENCE 279 (1988): 548-552.

[49] Han, Y., Kim, H., Park, J., Lee, S.-h., and Kim, J.-y. Influence of Ti doping level on hydrogen adsorption of mesoporous Ti-SBA-15 materials prepared by direct synthesis. International Journal of Hydrogen Energy 37(19) (2012): 14240-14247.

[50] Chia-Hung, L., Tien-Sung, L., and Chung-Yuan, M. $(VO)^{2+}$ Ions Immobilized on Functionalized Surface of Mesoporous Silica and Their Activity toward the Hydroxylation of Benzene. J. Phys. Chem. 107 (2003): 2543-2551.

[51] Bandas, C., et al. Microwave-Assisted Hydrothermal Method for Synthesis of Nanocrystalline Anatase TiO_2. Chem. Bull. 56 (2011): 81-84.

[52] Mu, Z., Li, J.J., Tian, H., Hao, Z.P., and Qiao, S.Z. Synthesis of mesoporous Co/Ce-SBA-15 materials and their catalytic performance in the catalytic oxidation of benzene. Materials Research Bulletin 43(10) (2008): 2599-2606.

[53] Volanti, D.P., et al. Synthesis and characterization of CuO flower-nanostructure processing by a domestic hydrothermal microwave. Journal of Alloys and Compounds 459(1-2) (2008): 537-542.

[54] Li, X., Liu, X., Xu, L., Wen, Y., Ma, J., and Wu, Z. Highly dispersed Pd/PdO/Fe2O3 nanoparticles in SBA-15 for Fenton-like processes: confinement and synergistic effects. Applied Catalysis B: Environmental 165 (2015): 79-86.

[55] Kaid, M.A. Characterization of Electrochromic Vanadium Pentoxide Thin Films Prepared By Spray Pyrolysis. Egypt. J. Solids 29 (2006): 273-291.

[56] Lv, Q., Li, G., and Sun, H. Synthesis of hierarchical TS-1 with convenient separation and the application for the oxidative desulfurization of bulky and small reactants. Fuel 130 (2014): 70-75.

[57] Ranga, R. and Ranjan, S. XRD and UV-Vis diffuse reflectance analysis of CeO_2–ZrO_2 solid solutions synthesized by combustion method. Proc. Indian Acad. Sci. 113 (2001): 651-658.

[58] Renuka, N.K., Shijina, A.V., Praveen, A.K., and Aniz, C.U. Redox properties and catalytic activity of CuO/gamma-Al(2)O(3) meso phase. J Colloid Interface Sci 434 (2014): 195-200.

[59] Li, Y., et al. Direct synthesis of highly ordered Fe-SBA-15 mesoporous materials under weak acidic conditions. Microporous and Mesoporous Materials 84(1-3) (2005): 41-49.

[60] Reyes-Carmona, Á., et al. Iron-containing SBA-15 as catalyst for partial oxidation of hydrogen sulfide. Catalysis Today 210 (2013): 117-123.

[61] Hassan Zahedi-Niaki, M., Javaid Zaidi, S.M., and Kaliaguine, S. Comparative study of vanadium aluminophosphate molecular sieves VAPO-5, -11, -17 and -31. Applied Catalysis A: General 196(1) (2000): 9-24.

[62] Shaojun, M., et al. On the Role of Vanadia Species for VO_x/SiO_2 in the Selective Oxidation of Methane. Journal of Natural Gas Chemistry 14 (2005): 77-87.

[63] Datta, A., Agarwal, M., and S, D. A novel procedure for the synthesis of NH3 incorporated VPO phase. J. Mater. Chem. 12 (2002): 1892-1897.

[64] Liu, Y.-M., et al. Vanadium oxide supported on mesoporous SBA-15 as highly selective catalysts in the oxidative dehydrogenation of propane. Journal of Catalysis 224(2) (2004): 417-428.

[65] Fornés, V., López, C., López, H.H., and Martínez, A. Catalytic performance of mesoporous VOx/SBA-15 catalysts for the partial oxidation of methane to formaldehyde. Applied Catalysis A: General 249(2) (2003): 345-354.

[66] Tsoncheva, T., Linden, M., Areva, S., and Minchev, C. Copper oxide modified large pore ordered mesoporous silicas for ethyl acetate combustion. Catalysis Communications 7(6) (2006): 357-361.

[67] Lallemand, M., Rusu, O.A., Dumitriu, E., Finiels, A., Fajula, F., and Hulea, V. NiMCM-36 and NiMCM-22 catalysts for the ethylene oligomerization: Effect of zeolite texture and nickel cations/acid sites ratio. Applied Catalysis A: General 338(1–2) (2008): 37-43.

[68] Scopel, W.L. and Fantini, M.C.A. Local Order Structure of a-SiO_xN_y:H Grown by PECVD. Brazilian Journal of Physics 32 (2002): 366-368.

[69] Ellis R. Lippincott, Alvin V. Valkenburg, Charles E. Weir, and Bunting, E.N. Infrared Studies on Polymorphs of Silicon Dioxide and Germanium Dioxide. Journal of Research of the National Bureau of Standards 61 (1958): 61-70.

[70] Enhanced Photophysical Properties of Nanopatterned Titania Nanodots/Nanowires upon Hybridization with Silica via Block Copolymer Templated Sol-Gel Process [Online]. Available from: http://www.mdpi.com/2073-4360/2/4/490/htm [9 December 2016]

[71] (!!! INVALID CITATION !!!).

[72] [$VO(acac)_2$] hybrid catalyst: from complex immobilization onto silica nanoparticles to catalytic application in the epoxidation of geraniol [Online]. Available from: http://pubs.rsc.org/en/content/articlehtml/2011/cy/c1cy00090j [10 December 2016]

[73] Liu, X., et al. Room-Temperature Synthesis in Acidic Media of Large-Pore Three-Dimensional Bicontinuous Mesoporous Silica with Ia3d Symmetry Chem. Int. Ed. 41 (2002): 3876-3878.

[74] Macías, G., Ramírez, J., Gutiérrez-Alejandre, A., and Cuevas, R. Preparation of highly active NiMo/Al-SBA15 (x) HDS catalysts: Preservation of the support hexagonal porous arrangement. Catalysis Today 133-135 (2008): 261-266.

[75] Sherif A, E.S., Takaaki, H., and Fujio, M. Large-Scale Design of Cubic Ia3d Mesoporous Silica Monoliths with High Order, Controlled Pores, and Hydrothermal Stability. Advanced Materials 17 (2005): 47-53.

[76] Zhang, H., Tang, C., Lv, Y., Gao, F., and Dong, L. Direct synthesis of Ti-SBA-15 in the self-generated acidic environment and its photodegradation of Rhodamine B. Journal of Porous Materials 21(1) (2013): 63-70.

[77] Janssen, A.H., Yang, C.M., Wang, Y., Schu1th, F., Koster, A.J., and de Jong, K.P. Localization of Small Metal (Oxide) Particles in SBA-15 Using Bright-Field Electron Tomography. J. Phys. Chem. B 107 (2003): 10552-10556.

[78] Jung, W.Y., et al. Synthesis of Ti-containing SBA-15 materials and studies on their photocatalytic decomposition of orange II. Catalysis Today 131(1–4) (2008): 437-443.

[79] Gao, X. and Xu, J. A new application of clay-supported vanadium oxide catalyst to selective hydroxylation of benzene to phenol. Applied Clay Science 33(1) (2006): 1-6.

[80] Makgwane, P.R. and Ray, S.S. Development of a high-performance nanostructured V2O5/SnO2 catalyst for efficient benzene hydroxylation. Applied Catalysis A: General 492 (2015): 10-22.

[81] Feng, S., Pei, S., Yue, B., Ye, L., Qian, L., and He, H. Synthesis and Characterization of V-HMS Employed for Catalytic Hydroxylation of Benzene. Catalysis Letters 131 (2009): 458-462.

[82] Dapurkar, S.E., Sakthivel, A., and Selvam, P. Mesoporous VMCM-41: highly efficient and remarkable catalyst for selective oxidation of cyclohexane to cyclohexanol. Journal of Molecular Catalysis A: Chemical 223(1-2) (2004): 241-250.

[83] Ferreira, R.S.G., de Oliveira, P.G.P., and Noronha, F.B. The effect of the nature of vanadium species on benzene total oxidation. Applied Catalysis B: Environmental 29(4) (2001): 275-283.

[84] Hongchuan, X., et al. Enhanced Catalytic Oxidation by Hierarchically Structured TS-1 Zeolite. J. Phys. Chem. 114 (2010): 6553–6559.

[85] Wu, P., Tatsumi, T., Komatsu, T., and Yashima, T. A Novel Titanosilicate with MWW Structure: II. Catalytic Properties in the Selective Oxidation of Alkenes. Journal of Catalysis 202(2) (2001): 245-255.

APPENDICES

Iodometric titration

Part 1 Standardization of Sodium Thiosulfate

$$\text{Normality of sodium thiosulfate solution} = \frac{(\text{g } KIO_3)(\text{mL } KIO_3)}{(\text{mL } Na_2S_2O_3)(35.67 \text{ g.L/eq})}$$

Part 2 Determination of Hydrogen Peroxide

$$\text{Hydrogen peroxide (\%w/w)} = \frac{(A\text{-}B)(N)(1.7007)}{\text{Sample weight}}$$

Where: A = Titration volume for sample

B = Titration volume for blank.

N = Normality of $Na_2S_2O_3$

Hydrogen peroxide efficiency

H_2O_2 efficiency = (mole of H_2O_2 decomposed/starting mole of H_2O_2) x 100

VITA

Miss Pornpimol Wongsuwan was born on March 4, 1990 in Suratthani, Thailand. She graduated with Bachelor of Chemistry from Faculty of Science, Srinakharinwirot University, in 2012. She continued her study in Petrochemistry and Polymer Science Program, Faculty of Science, Chulalongkorn University in 2012 and completed in 2016.

In 9-11 February 2016, she joints the Pure and Applied Chemistry International Conference (PACCON 2016) at Bitec, Bangkok, Thailand. The approval of proceeding and poster presentation was in the title of “Preparation and characterization of metal modified Ti-MWW for benzene hydroxylation.